DEVELOPMENT OF A PORTABLE AEROSOL COLLECTOR AND SPECTROMETER (PACS)

by

Changjie Cai

A thesis submitted in partial fulfillment
of the requirements for the Doctor of Philosophy
degree in Occupational and Environmental Health in the
Graduate College of
The University of Iowa

May 2018

Thesis Supervisor: Professor Thomas M. Peters

Graduate College
The University of Iowa
Iowa City, Iowa

CERTIFICATE OF APPROVAL

_____

PH.D. THESIS

_____

This is to certify that the Ph.D. thesis of

Changjie Cai

has been approved by the Examining Committee for
the thesis requirement for the Doctor of Philosophy degree
in Occupational and Environmental Health at the May 2018 graduation.

Thesis Committee: _____
Thomas M. Peters, Thesis Supervisor

_____
Geb W. Thomas

_____
Tianbao Yang

_____
T. Renée Anthony

_____
Charles O. Stanier

To Dan Li

ACKNOWLEDGEMENTS

Enormous thanks are due to my wife, Dan Li, my beloved eternal companion, who has been giving me never-ending support and help. She has been encouraging and believing in me, especially when I felt discouraged. I would not be where I am today without her. I also appreciate my father, Wenguang Cai, and mother, Xiuchun Hua, who have been teaching me to become a person who is willing to help others and to contribute to society.

I would like to express my sincere gratitude to my advisor, Dr. Tom Peters, who modeled a mentor who I would like to be in the future. My original definition of *research* was limited to an individual adventure. However, Tom enriched my personal dictionary by instilling an additional dimension to research: research is a collaborative enterprise; good research involves a group of people who share the same vision, with each of them contributing their expertise and skills. Tom always emphasized that good research transcends the human-and-computer interaction; it is a result of collaborative endeavors. He challenged me to jump outside my comfort zone. Tom also spent numerous time helping me improve my skills of writing and presentation.

The value of working as a team has proven to be true as I communicated with and learned from all other committee members, Dr. Geb Thomas, Dr. Tianbao Yang, Dr. Renée Anthony, and Dr. Charles Stanier. The collaborative, scholarly interactions and exchanges led to a much higher productivity than a simple addition of each person's contribution. This dissertation would not have been completed without the support from all committee members. I really appreciate each committee member's tremendous contribution. This collaborative lens will be instilled to my future work as a researcher, educator, and service provider.

I would also like to thank Dr. Jae Hong Park, Dr. David Peate, Dr. Larissa Stebounova, Dr. Sinan Sousan, Kate Leonard, Andrew Halterman, Levi Mines, Ryan Grant, Sam Jones, Laura Hallett, Theresa McCollom, Alyson Gray, Kevin Gettz, and Chun Hoe Ong who worked with me in the laboratory. In addition, I feel grateful that Dr. Matthew Nonnenmann provided many teaching opportunities for me. I also appreciate Dr. Patrick O'Shaughnessy for taking our industrial hygiene students to several occupational places to have the real workplace field experience.

This work was supported by the small-business innovative research (SBIR) project (AF131-024) from the U.S. Air Force and the pilot project (No. T42OH008491) from the Heartland Center for Occupational Health & Safety at the University of Iowa.

ABSTRACT

The overall goal of this doctoral dissertation is to develop a prototype instrument, a Portable Aerosol Collector and Spectrometer (PACS), that can continuously measure aerosol size distributions by number, surface area and mass concentrations over a wide size range (from 10 nm to 10 μm) while also collecting particles with impactor and diffusion stages for post-sampling chemical analyses.

To achieve the goal, in the first study, we designed, built and tested the PACS hardware. The PACS consists of a six-stage particle size selector, a valve system, a water condensation particle counter to measure number concentrations and a photometer to measure mass concentrations. The valve system diverts airflow to pass sequentially through upstream stages of the selector to the detectors. The stages of the selector include three impactor and two diffusion stages, which resolve particles by size and collect particles for chemical analysis. Particle penetration by size was measured through each stage to determine actual performance and account for particle losses. The measured d_{50} of each stage (aerodynamic diameter for impactor stages and geometric diameter for diffusion stages) was similar to the design. The pressure drop of each stage was sufficiently low to permit its operation with portable air pumps.

In the second study, we developed a multi-modal log-normal (MMLN) fitting algorithm to leverage the multi-metric, low-resolution data from one sequence of PACS measurements to estimate aerosol size distributions of number, surface area, and mass concentration in near-real-time. The algorithm uses a grid-search process and a constrained linear least-square (CLLS) solver to find a tri-mode (ultrafine, fine, and coarse), log-normal distribution that best fits the input data. We refined the algorithm to obtain accurate and

precise size distributions for four aerosols typical of diverse environments: clean background, urban and freeway, coal power plant, and marine surface. Sensitivity studies were conducted to explore the influence of unknown particle density and shape factor on algorithm output. An adaptive process that refined the ranges and step sizes of the grid-search reduced the computation time to fit a single size distribution in near-real-time. Assuming standard density spheres, the aerosol size distributions fit well with the normalized mean bias (*NMB*) of -4.9% to 3.5%, normalized mean error (*NME*) of 3.3% to 27.6%, and R^2 values of 0.90 to 1.00. The fitted number and mass concentration biases were within ± 10% regardless of uncertainties in density and shape. With this algorithm, the PACS is able to estimate aerosol size distributions by number, surface area, and mass concentrations from 10 nm to 10 μm in near-real-time.

In the third study, we developed a new algorithm–the mass distribution by composition and size (MDCS) algorithm–to estimate the mass size distribution of various particle compositions. Then we compared the PACS for measuring multi-mode aerosols to three reference instruments, including a scanning mobility particle sizer (SMPS), an aerodynamic particle sizer (APS) and a nano micro-orifice uniform deposit impactor (nanoMOUDI). We used inductively coupled plasma mass spectrometry to measure the mass of collected particles on PACS and nanoMOUDI stages by element. For the three-mode aerosol, the aerosol size distributions in three metrics measured with the PACS agreed well with those measured with the SMPS/APS: number concentration, *bias* = 9.4% and R^2 = 0.96; surface area, bias = 17.8%, R^2 = 0.77; mass, bias = -2.2%, R^2 = 0.94. Agreement was considerably poorer for the two-mode aerosol, especially for surface area and mass concentrations. Comparing to the nanoMOUDI, for the three-mode aerosol, the

PACS estimated the mass median diameters (MMDs) of the coarse mode well, but overestimated the MMDs for ultrafine and fine modes. The PACS overestimated the mass concentrations of ultrafine and fine mode, but underestimated the coarse mode. This work provides insight into a novel way to simultaneously assess airborne aerosol size, composition, and concentration by number, surface area and mass using cost-effective handheld technologies.

PUBLIC ABSTRACT

Adverse health impacts from inhalation of aerosols are a complicated function of particle size, composition and concentration. An aerosol is defined as a collection of solid or liquid particles suspended in the air. Particles can be inhaled and deposit on different regions of human respiratory system depending on particle size. Deposited particles can exert adverse health effects depending on their composition and the quantity deposited, or dose. The relationship between adverse health effects and exposure or dose is also dependent upon the metric (number, surface area, or mass) used to express quantity. A combination of commercial research instruments are needed to assess exposures to aerosols by size, composition, and concentration. However, the expensive cost (~$200,000), bulky size, and heavy weight of a combination of these instruments limit their use to research studies.

This study centers on developing a portable and cost-effective device for collecting and measuring aerosols. This study includes three main parts: (1) development of the hardware, (2) development of the fitting algorithm, and (3) laboratory test of the device prototype. This work provides insight into a novel way to simultaneously assess airborne aerosol size, composition, and concentration using cost-effective handheld technologies.

TABLE OF CONTENTS

LIST OF TABLES

LIST OF FIGURES

CHAPTER I

INTRODUCTION

Introduction to Aerosol Characteristics

An aerosol is a collection of solid or liquid particles suspended in a gas (Seinfeld and Pandis, 2016). Particles are defined by their size, concentration, composition, and shape (Kulkarni et al., 2011) with the entire aerosol described by a compilation of these parameters called an aerosol size distribution. Aerosol size is one of the most important properties to determine the aerosol behavior in a gas (Rubenstein and Koehl, 1977). Concentration defines the quantity of particles per unit volume of gas (Heitbrink et al., 2008; Kulkarni et al., 2011). Aerosol composition varies dramatically by size due to the different sources and formation/removal mechanisms by size (Whitby, 1978; Bardouki et al., 2003). Furthermore, non-spherical aerosols (e.g., fibers and agglomerates) usually behave differently compared to spherical aerosols (Jianzhong et al., 2003; Zelenyuk et al., 2006).

The size of a particle largely determines how it behaves in a gas. Whitby (1978) divided ambient aerosols into three modes with aerodynamic diameter, a diameter of the spherical particle with a density of 1000 kg/m^3. The three modes include a nuclei mode (or ultrafine mode) (0.005 ~ 0.1 μm), an accumulation mode (or fine mode) (0.1 ~ 2 μm), and a coarse mode (greater than 2 μm) (Figure 1-1). For small particles (nuclei mode), they achieve significant diffusive motion caused by the random movement of gas molecules. By increasing the particle size, the impacts of inertia on the particle motion increase. Various motion mechanisms result in different deposition mechanisms of a particle. For instance, for a particle deposition onto a fiber of a filter, there are five basic deposition mechanisms:

diffusion, interception, inertial impaction, gravitational settling, and electrostatic attraction corresponding to various particle sizes (Rubenstein and Koehl, 1977). Figure 1-2 shows the total filter collection efficiency and the efficiency due to each of the single-fiber mechanisms given by Hinds (1999). Diffusion is the most important mechanism for particles smaller than 100 nm. The collection efficiency caused by interception and impaction mechanisms are negligible for particles smaller than 100 nm, but then increase rapidly with increasing the particle size. The gravitational settling mechanism is negligible for particles smaller than 1 μm. The electrostatic attraction mechanism is not shown in Figure 1-2, because this mechanism is not only related to the particle size, but also related to the charge on the particle.

Aerosol concentration can be expressed using multiple 'metrics', including number, surface area and mass concentration. Most modern exposure limits for aerosols are based on mass concentration (Chow et al., 1993; ACGIH, 2008). However, particle mass is dependent on diameter cubed, thus, the largest particles present in an atmosphere often obscure the mass of ultrafine (< 100 nm) particles. Here we use copper fume as an example. The mass concentration of 15 nm Cu particles with a number concentration of 10^6 particles/cm^3 (a high concentration for environmental or workplace settings) is only 0.0074 mg/m^3, or thirteen times lower than the Permissible Exposure Limit (PEL) of copper fume (0.1 mg/m^3) proposed by Occupational Safety and Health Administration (OSHA). Consequently, mass concentration is often not sufficient to fully describe an aerosol exposure. Other metrics (e.g., number and surface area) may be better indicators of exposure to ultrafine and fine mode particles (Brouwer et al., 2004; Heitbrink et al., 2008).

Aerosol composition typically varies by size. Figure 1-1 shows the schematic of an atmospheric aerosol size distribution, principle modes, sources, and formation and removal mechanisms (Whitby, 1978). For various size particles, the sources, and formation/removal mechanisms are quite different, which typically results in different chemical compositions by size. As an example, Bardouki et al. (2003) identified that aerosol consisted of different ions were different for urban aerosols. The main anion and cation was SO_4^{2-} and NH_4^+, respectively for the fine mode, whereas it was NO_3^- and Ca^{2+}, respectively for the coarse mode.

Particle shape changes the particle behavior in a gas. The Stokes' law for drag force on a moving particle is based on the assumption of spherical shape (Hinds, 1999). To account for departure of a non-spherical particle from sphericity, a drag correction factor, called dynamic shape factor, is introduced. The dynamic shape factor is defined as the ratio of the drag force on a non-spherical particle to the drag force on a spherical particle with a volume equivalent diameter and velocity (Hinds, 1999). Therefore, for non-spherical particles (e.g., fibers and agglomerates), particle shape is usually considered as a modification of the behavior of an ideal particle (a spherical particle with a density of 1000 kg/m^3) by using the dynamic shape factor (Jianzhong et al., 2003; Zelenyuk et al., 2006).

Health Effects of Aerosols

Adverse health effects from the inhalation of particles are a complicated function of particle size, shape, composition, and exposure/dose metric (e.g., number, surface area and mass concentration) (Harrison and Yin, 2000). Particles deposit in different regions of the respiratory system according to their size, density and shape (Hinds, 1999), whereas the adverse health effects potentially resulting from these deposited particle composition

and shape (Valavanidis et al., 2008; Palomäki et al., 2011). Researchers perform epidemiological and toxicological studies to identify aerosol exposures that elicit adverse health effects. They define these exposures in terms of aerosol concentration metric, size, composition, and sometimes shape (Wittmaack, 2007).

Particle size is critical in determining the particle deposition location in human respiratory system. Figure 1-3 shows the predicted total and regional deposition based on International Commission on Radiological Protection (ICRP) deposition model as a function of aerodynamic particle size from average data of males and females (Hinds, 1999). If aspirated into the respiratory tract, particles larger than 5 μm of aerodynamic diameter mainly deposit in the head airways by gravitational settling and impaction mechanisms. For particles between 0.1 and 1 μm, the deposition through the respiratory track is minimal due to the relatively insignificance of all deposition mechanisms. For particles between 10 and 100 nm, the fraction deposited within alveolar, tracheobronchial and head airways regions increase with decreasing the particle size due to the increasing significance of the diffusion mechanism. Particles smaller than 10 nm mostly deposit on the head airways region by diffusion.

Particle shape is another important physical factor in an aerosol that can cause adverse health effects. Some materials, such as asbestos fibers and carbon nanotubes (CNTs), have unique chemical and physical characteristics which have attracted the interest of industrial manufacturers. However, they also have raised concerns about their unique health risks due to their needle-like shape (Maynard et al., 2006). For example, exposure to the needle-like shape of asbestos fibers can cause a series of adverse health effects such as chronic pulmonary inflammation, fibrosis, and mesothelioma (Craighead et al., 1982;

Mossman and Churg, 1998). The needle-like shape of carbon nanotubes resemble asbestos and also shows asbestos-like pathogenicity (Poland et al., 2008; Takagi et al., 2008; Palomäki et al., 2011).

Various particle compositions result in different adverse health effects. Inhaling manganese (Mn) oxide nanoparticles could increase the Mn concentrations in many human organs such as olfactory bulb, lung, striatum, frontal cortex, and cerebellum (Elder et al., 2006). Human studies have shown that elevated levels of Mn are associated with increased rates of Parkinsonism and Parkinson's disease (Olanow, 2004; Kwakye et al., 2015). Karlsson et al. (2008) indicated that copper (Cu) oxide nanoparticles are much more toxic than CNTs. Cu oxide nanoparticles are also potent regarding cytotoxicity and deoxyribonucleic acid (DNA) damage. For silver (Ag) nanoparticles, many studies indicated that they could be toxic to the mammalian cells derived from human organs including skin, liver, lung, brain, vascular system, and reproductive organs (Ahamed et al., 2010). The Ag nanoparticles were also found to induce cell death and oxidative stress in human fibrosarcoma and skin carcinoma cells, and they could enter cells to cause DNA damage and apoptosis in fibroblasts and liver cells (Arora et al., 2008; Arora et al., 2009).

The most relevant exposure/dose metric needs to be identified to study the health effects of aerosols by size. Traditionally, the mass concentration has been used in epidemiological studies. For example, the mass concentrations of particles smaller than 2.5 μm ($PM_{2.5}$) are associated with lung cancer and cardiopulmonary mortality (Pope et al., 2002), and those of particles between 2.5 μm and 10 μm ($PM_{10-2.5}$) are associated with chronic obstructive pulmonary disease, asthma and respiratory admissions (Brunekreef and Forsberg, 2005). Consequently, governmental agencies express most limits in terms of

aerosol mass concentration integrated over wide size ranges, such as the $PM_{2.5}$ and PM_{10} National Ambient Air Quality Standards (NAAQS) from Environmental Protection Agency (EPA) for ambient air, and Occupational Exposure Limits (OELs) from Mine Safety and Health Administration (MSHA), the National Institute for Occupational Safety and Health (NIOSH), and Occupational Safety and Health Administration (OSHA) for personal exposures in the workplace. Other metrics (such as number and surface area concentration) are increasingly considered important and potentially better predictors of adverse health effects than mass concentration, especially for ultrafine and fine mode particles (Brouwer et al., 2004; Ramachandran, 2005; Ellenbecker and Tsai, 2015).

Aerosol Measurement Devices

The measurement of aerosols is important in many fields, including public health, manufacturing, pharmaceuticals, toxicology, and atmospheric science (Kulkarni et al., 2011). Environmental engineers/scientists and industrial hygienists conduct aerosol measurements to ensure that the public and workers are not exposed to hazardous concentrations (Ostro et al., 1996; Turpin and Lim, 2001; Maynard et al., 2004). In pharmaceutical sciences, aerosols are measured to determine the delivered dose to target organs in the human body (Alexander et al., 2008). Toxicologists study how aerosol concentration, size, and composition affect adverse toxic health effects on biological systems (Natusch and Wallace, 1974; Pöschl, 2005). Atmospheric scientists measure aerosols to study their effects on the earth system, including the weather and climate. (Carslaw et al., 2010).

We summarize four categories of devices for measuring and sampling airborne aerosols in Table 1-1: (1) Time-Resolved & Size-Integrated, (2) Time-Resolved & Size-

Resolved, (3) Time-Integrated & Size-Integrated, and (4) Time-Integrated & Size-Resolved. Direct-reading instruments have been developed for wide use over the three decades. They includes the first two main categories: (1) Time-Resolved & Size-Integrated, and (2) Time-Resolved & Size-Resolved (Table 1-1). The portable Time-Resolved & Size-Integrated devices (e.g., condensation particle counter (CPC), photometer, and diffusion charging) are able to provide real-time measurement. However, they provide limited size information and only output concentration in one metric per device. The Time-Resolved & Size-Resolved devices can provide detailed real-time or near-real-time aerosol size distributions. The scanning mobility particle sizer (SMPS) measures number concentration of sub-micrometer particles highly resolved by equivalent mobility particle size (Wang and Flagan, 1990), and the aerodynamic particle sizer (APS) measures number concentrations of aerosols from 0.5 μm to 20 μm highly resolved by aerodynamic particle size (Baron, 1986).

Researchers have combined size-selective technologies to overcome the limited measurement size range. For example, Harrison et al. (2000) combined the SMPS and APS, using highly size-resolved information to estimate aerosol size distributions of number, surface area and mass concentration from 10 nm to ~20 μm. The wide range aerosols system (WRAS) combines the portable aerosol optical spectrometer, differential mobility analyzer (DMA) and CPC to measure aerosol size distributions by different metrics over a wide size range from ~5 nm to ~30 μm (Keck et al., 2011). However, the SMPS/APS and WRAS system are not portable. The wide-range particle spectrometer (WPSTM) introduced by Liu et al. (2010) can measure aerosol size distributions from ~10 nm to ~10 μm by combining a scanning mobility spectrometer (SMS) and a laser particle spectrometer

(LPS). The WPSTM is small enough to fit into a small portable cabinet. Nevertheless, this system does not collect particles by size for later chemical and physical analysis. Other portable Time-Resolved & Size-Resolved devices, such as the optical particle sizer (OPS) and the electrical low pressure impactor (ELPI), can measure number size distributions as well (Keskinen et al., 1992; Gouesbet and Grehan, 2013).

Time-Integrated devices enable the collection of particles for chemical and physical analysis. They include two main categories: (1) Time-Integrated & Size-Integrated, and (2) Time-Integrated & Size-Resolved (Table 1-1). Most of the Time-Integrated & Size-Integrated samplers, such as 37-mm filter cassette and inhalable IOM sampler, are used to measure time-averaged personal exposures, but they are time and labor consuming samplers with limited size information (Demange et al., 2002). The Time-Integrated & Size-Resolved devices, such as nano micro-orifice uniform deposit impactor (nanoMOUDI) and low pressure cascade impactor, can collect particles by aerodynamic particle size (Marple et al., 1986, 1991; Maenhaut et al., 1996). Collected particles can be analyzed gravimetrically to determine mass or with chemical techniques, such as inductively coupled plasma mass spectroscopy (ICP-MS), to determine mass by composition (Herner et al., 2006; Onat et al., 2012). In addition, the nanoMOUDI is not portable because a large and heavy pump is needed to provide a flowrate of 10 L/min and to overcome high pressure drops caused by the small impactor nozzles in the last few impactor stages.

Researchers have combined Time-Resolved & Size-Integrated and Time-Integrated & Size-Resolved devices to both measure and collect particles by size for chemical analysis. For example, Vosburgh et al. (2013) combined a personal diffusion battery for

size separation with a CPC to provide the aerosol size distributions of sub-micrometer particles. Similarly, the number concentration and size were collected using a combination of CPC and an ELPI (Brachert et al., 2014).

Aerosol Parameterization and Data Inversion Algorithms

While aerosol size distributions can be simply tabulated or plotted, it is convenient to fit the data to a function allowing the distribution to be characterized by only a few parameters. A variety of functions have been used for this purpose. For instance, the Rosin-Rammler distribution, which is related to the Weibull distribution, is applicable to coarsely dispersed dusts and sprays (RosIN, 1933). The Nukiyama-Tanasawa distribution is used for sprays having extremely broad size ranges (Nukiyama, 1939). An inverse power law distribution (Junge distribution) can be applied to the size distribution of atmospheric aerosols (Twomey, 1975). The Khrgian-Mazin distribution, a modified gamma distribution, is applicable to the size distributions of cloud droplets (Pruppacher and Klett, 2012). The exponential distribution is used to the aerosol number size distributions (Maher and Laird, 1985). The log-normal distribution is the most widely used distribution for aerosols according to reasonably good fits to a variety of empirical data (Hinds, 1999; Kulkarni et al., 2011).

Aerosol size distributions can be mathematically described using a multi-modal log-normal (MMLN) distribution. Whitby and Sverdrup (1980) showed that a tri-modal, log-normal distribution could describe aerosols from eight typical atmospheric size distributions, including marine surface, clean continental background, average background, background and aged urban plume, background and local sources, urban average, urban and freeway, and coal power plant. Other researchers have also found the tri-modal log-

normal distribution to fit measured aerosol size distributions well (Wilson and Suh, 1997; Hussein et al., 2005; Liu et al., 2008).

Mathematical algorithms have been developed to fit size-resolved aerosol data. Twomey (1965) introduced a constrained linear inversion algorithm to infer aerosol size distributions from filter measurements taken at different flowrates. Later, Twomey (1975) introduced an iterative nonlinear inversion algorithm, and compared two algorithms that estimated the parameters of a bimodal number distribution from aerosol measurements using filters. The results showed that his iterative, nonlinear algorithm out-performed his constrained, linear inversion algorithm when the measurements extended over a wide dynamic range. A nonlinear algorithm is initialized with an initial guess for the distribution, and then to correct repeatedly until the functions converge within some specified degree. However, his nonlinear iterative algorithm tended to oscillate rather than consistently moving toward a solution. Crump and Seinfeld (1982) suggested a generalized cross validation algorithm, which performed better in numerical examples than Twomey's nonlinear algorithm. Markowski (1987) refined Twomey's algorithm with a mathematical smoothing technique designed to minimize the oscillation.

Other data inversion algorithms for aerosol measurement data have been developed in last few decades. Maher and Laird (1985) developed an expectation-maximization (EM) algorithm to fit an aerosol size distribution for the ultrafine mode from diffusion battery data. This EM algorithm is an iterative computation of maximum likelihood estimates for data whose distributional properties can be described as the integral of an appropriate exponential function. This algorithm provides a unique solution vector, which guarantees a nonnegative concentration. Wolfenbarger and Seinfeld (1990) developed an inversion

algorithm based on regularization to find smooth size distributions that represent data measured by multiple instruments (such as a diffusion batteries, OPCs, DMAs and low pressure impactors). The size range of fitted aerosol size distributions covered from 1 nm to 10 µm. Hussein et al. (2005) developed an algorithm to fit the aerosol number size distributions automatically without knowing the number of modes. Taylor et al. (2014) applied a Gaussian mixture model to fit aerosol data obtained from the Aerosol Robotic Network, which measures atmospheric aerosol properties using sun photometers.

Shortcomings of the Literature

Commercial instruments provide a way to continuously assess aerosol concentrations by size and metric. Photometers continuously measure aerosol mass concentrations in environmental and occupational settings (Görner et al., 1995). CPCs measure number concentrations (Hering et al., 2005; 2014). Both type of instruments are portable and continuous, but provide limited size information on a single metric (e.g., number or mass concentration) and no information on composition. The SMPS and APS provide a continuous measurement of aerosol size distributions, but are very expensive (~$50,000 to $100,000), large, and heavy. Moreover, none of these instruments provide information on particle composition.

Aerosol samplers collect particles for subsequent chemical analyses that can determine particle composition. Size- and time-integrated samplers, such as the 37-mm filter cassette and inhalable IOM sampler, are widely used to measure personal exposures in the workplace (Demange et al., 2002), but yield little information on the size of the collected particles. Size-resolved and time-integrated devices, such as the nanoMOUDI cascade, collect particles by aerodynamic particle size. Although these instruments provide

a way to measure mass concentration by size and composition, they do not provide continuous real-time aerosol size distribution information. The ELPI can output continuous aerosol size distribution information, while simultaneously collecting particles for chemical analysis after sampling (Järvinen et al., 2017). However, the cost of the ELPI (>$100,000) precludes its widespread use in exposure assessment. There is no single portable instrument that measure aerosol size distributions in various metrics (e.g., number, surface area and mass concentrations) relevant to health effects investigations *and* also collect particles by size for subsequent chemical analysis.

Aerosol size distributions of one metric can be converted to those of other metrics. For the SMPS and APS size distribution data, users converted raw count data to number, surface area and volume concentrations (Abt et al., 2000). However, uncertainties in sizing and concentration made with the original measurements are exacerbated in the conversion. For example, the smallest *mass* concentration mode in the atmospheric aerosol is the nuclei mode, which may contain the highest *number* of aerosols. Consequently, number concentrations of nuclei mode particles are subject to large uncertainty when transforming from instruments that provide the mass concentration of an aerosol by size (e.g., the cascade impactor) (Whitby, 1978). The data from multiple instruments providing aerosol size distributions in multiple metrics may potentially reduce the uncertainties in estimating accurate size distributions over a wide size range.

Specific Aims

The overall goal of this doctoral dissertation is to develop a prototype instrument, a Portable Aerosol Collector and Spectrometer (PACS) that can continuously measure aerosol size distributions by number, surface area and mass concentrations over a wide size

range (from 10 nm to 10 μm), and can collect particles with impactor and diffusion stages for post-sampling chemical analyses. To achieve this goal, in Aim 1, we designed and developed the PACS hardware. In Aim 2, we developed a MMLN fitting algorithm to enable continuous output of aerosol size distributions in the three metrics. In Aim 3, we conducted laboratory experiments to evaluate the PACS prototype for measuring multi-modal aerosols by size in multiple concentration metrics, and by composition.

Aim 1. Development of a Portable Aerosol Collector and Spectrometer (PACS) Part I: Design and Hardware Development. In this study, we described the design and testing of the PACS hardware. The target journal for this work is the *Environmental Science and Technology*.

Aim 2. Development of a Portable Aerosol Collector and Spectrometer (PACS) Part II: Algorithm to Estimate Size Distributions. In this study, we presented a MMLN fitting algorithm to leverage the multi-metric, low-resolution data from one sequence of PACS measurements to estimate the number, surface area and mass concentration highly resolved by aerodynamic particle size ranging from 10 nm to 10 μm in near-real-time. The target journal for this work is the *Environmental Science and Technology*.

Aim 3. Evaluation of a Portable Aerosol Collector and Spectrometer (PACS) to Measure Particle Concentrations by Size and Composition. In this laboratory study, we evaluated the ability of the PACS to measure aerosol size distributions in near-real-time for three metrics (number, surface area and mass concentration) and estimate mass size distributions of various particle compositions. We compared the aerosol size distributions measured with the PACS to those measured with reference instruments,

including a SMPS, an APS and a nanoMOUDI for multi-modal aerosols. The target journal for this work is the *Environmental Science and Technology*.

Table 1-1: Selected devices for measuring and sampling airborne particles (Modified from Kuhlbusch et al., 2011)

Category	Selected devices	Size range	Time resolution	Metric	Advantages	Limitations
Time Resolved & Size Integrated	Condensation particle counter (CPC)	> ~10 nm	1 sec	Number concentration	(1) Real-time measurement; (2) Portable;	(1) Limited size information; (2) No collection of particles for chemical and morphological analysis;
	Photometer	> 100 nm	1 sec	Mass concentration		
	Diffusion Charging	> ~10 nm	1 sec	Surface area concentration		
Time Resolved & Size Resolved	Scanning Mobility Particle Sizer (SMPS)	~1 nm – ~800 nm	>30 sec	Number size distribution	(1) Most output detailed size information; (2) Real-time measurement;	(1) Most not easily portable; (2) Expensive; (3) Most of them cannot collect particles for chemical and morphological analysis;
	Aerodynamic Particle Sizer (APS)	~700 nm – ~20 µm	~1 sec	Number size distribution		
	Wide range aerosol system (WRAS)	~5 nm – ~20/30 µm	>30 sec	Number size distribution		
	Wide-range particle spectrometer (WPS)	~10 nm – 0.5 µm for CPC; 0.4 µm – 10 µm for LPS	~1 sec	Number and mass size distributions		
	Optical particle sizer (OPS)	~300 nm – ~20 µm	~1 sec	Number size distribution		
	Electrical low pressure impactor (ELPI)	~30 nm – 1.0 µm	1 min or 1 sec	Number and mass size distributions		

Table 1-1: Continued

Time Integrated & Size Integrated	Filtration	n.a.	n.a.	Mass concentration	(1) Personal; (2) Collection of particles for chemical and morphological analysis;	(1) Limited size information; (2) Time and labor consuming;
	personal sampler	n.a.	n.a.	Mass concentration		
Time Integrated & Size Resolved	Nano micro-orifice uniform deposit impactor (nanoMOUDI) cascade	~10 nm – 10 µm	n.a.	Mass size distribution	(1) Collection of particles for chemical and morphological analysis;	(1) Time and labor consuming;
	Low pressure cascade impactor	> 20 nm	n.a.	Mass size distribution		

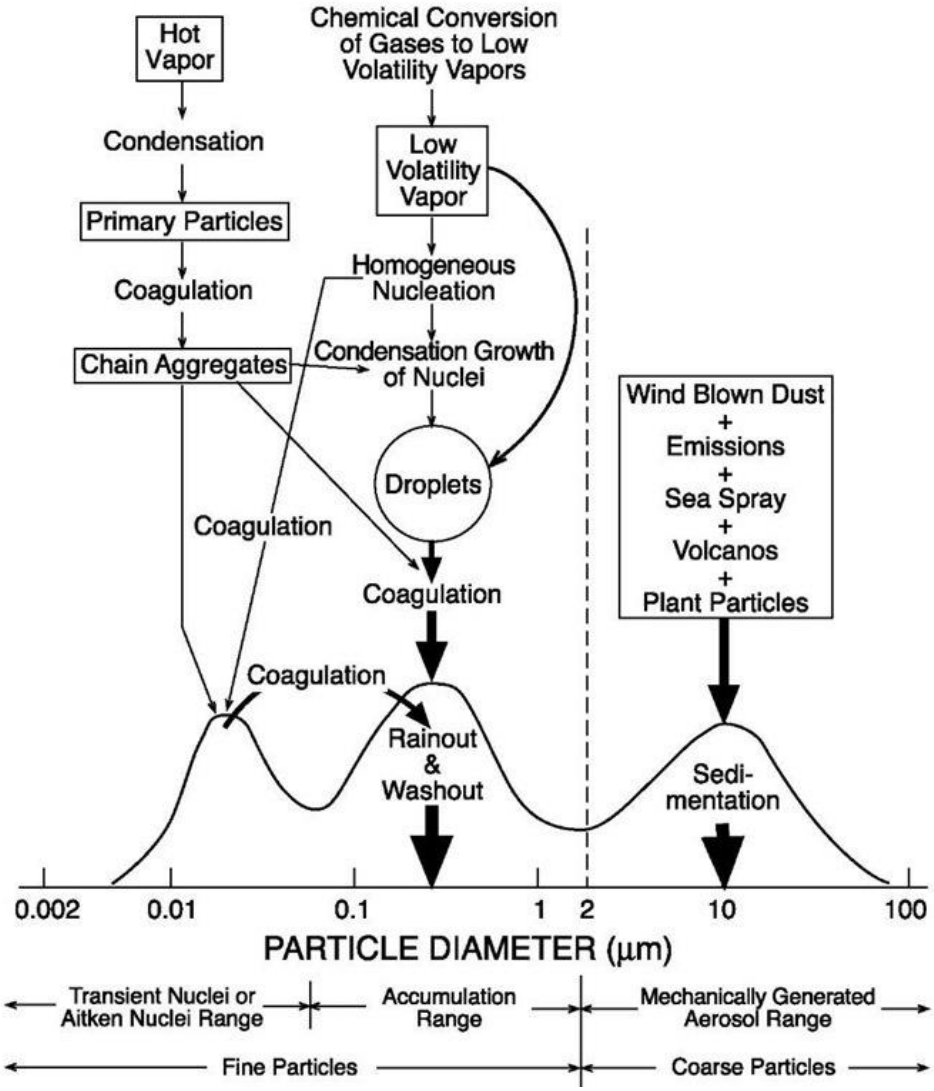

Figure 1-1: Schematic of an atmospheric aerosol size distribution, principle modes, sources, and particle formation and removal mechanisms. Figure is from Whitby (1978).

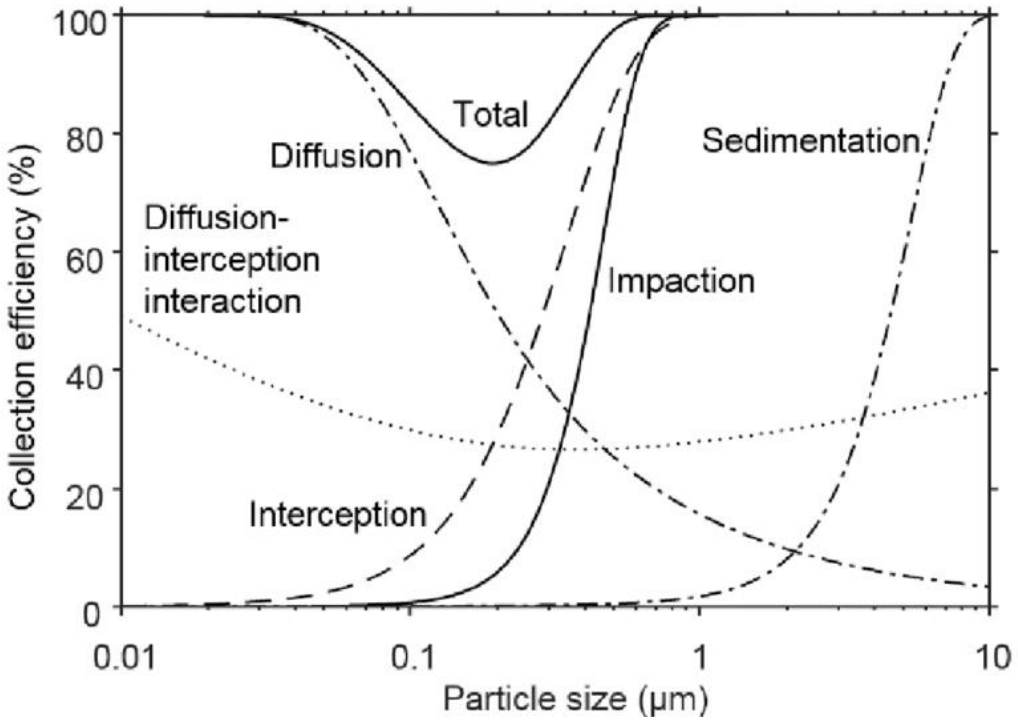

Figure 1-2: Filter efficiency for individual single-fiber mechanisms and total efficiency. Figure is from Hinds (1999).

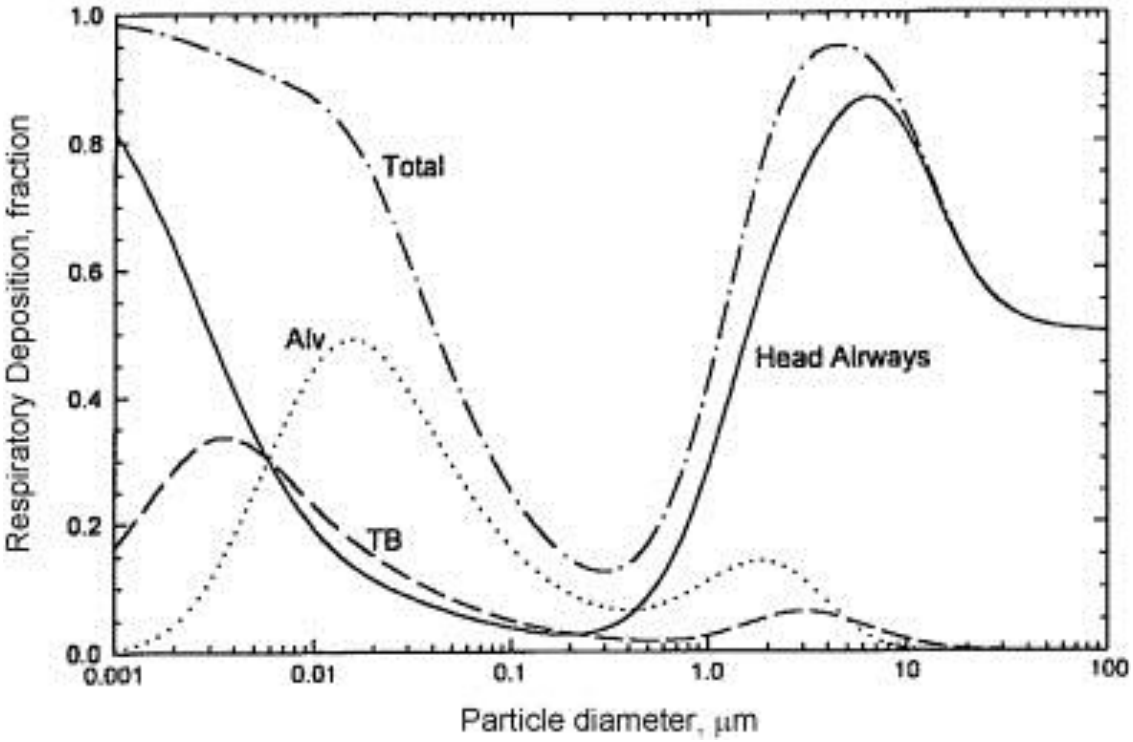

Figure 1-3: Predicted total and regional deposition based on International Commission on Radiological Protection (ICRP) deposition model for light exercise (nose breathing). Figure is from Hinds (1999).

CHAPTER II

DEVELOPMENT OF A

PORTABLE AEROSOL COLLECTOR AND SPECTROMETER (PACS)

PART I: DESIGN AND HARDWARE DEVELOPMENT

Abstract

Adverse health impacts from inhalation of particles depend on particle size, composition, and concentration, but the instruments that measure these health-relevant parameters are often limited. This study characterizes the hardware components of a Portable Aerosol Collector and Spectrometer (PACS), a prototype device designed to continuously measure aerosol size distributions of number, surface area and mass concentration from 10 nm to 10 μm and collect particles with impactor and diffusion stages for subsequent chemical analysis. The PACS consists of a six-stage particle size selector, a valve system, a water condensation particle counter to detect number concentrations, and a photometer to detect mass concentrations. The valve system diverts airflow to pass sequentially through upstream stages of the selector to the detectors. The stages of the selector include three impactor and two diffusion stages, which resolve aerosols by aerodynamic and geometric particle size, respectively, and collect particles for later chemical analysis. Particle penetration by size was measured through each stage to determine actual collection performance and account for particle losses. The measured d_{50} of each stage was similar to the design. The pressure drop of each stage was sufficiently low to permit its operation with portable air pumps. The PACS represents a novel way to simultaneously assess airborne aerosol size, composition, and concentration by number, surface area and mass.

Introduction

Adverse health effects from the inhalation of particles are a complicated function of particle size, shape, composition, and exposure metric (e.g., number, surface area and mass concentration) (Harrison and Yin, 2000). Aerosols are typically classified into three size modes: (1) ultrafine mode (i.e., <100 nm, nanoparticles), (2) fine (or accumulation) mode (i.e., 100 nm ~ 1 μm, fine particles) and (3) coarse mode (i.e., 1 μm ~ 10 μm, coarse particles) (Wallace and Howard-Reed, 2002). Particles deposit in different regions of the respiratory system according to their size (Hinds, 1999), whereas the adverse health effects potentially resulting from these deposited particles depend on particle composition (Valavanidis et al., 2008). The mass concentrations of ambient particulate matter smaller than 2.5 μm ($PM_{2.5}$, ultrafine and fine mode particles) are associated with lung cancer and cardiopulmonary mortality (Pope et al., 2002), and those of coarse mode particles ($PM_{10-2.5}$) are associated with chronic obstructive pulmonary disease, asthma and respiratory admissions (Brunekreef and Forsberg, 2005). Consequently, governmental agencies express most limits in terms of aerosol mass concentration integrated over wide size ranges, such as the $PM_{2.5}$ and PM_{10} National Ambient Air Quality Standards from Environmental Protection Agency for ambient air and occupational exposure limits from Mine Safety and Health Administration, the National Institute for Occupational Safety and Health, and Occupational Safety and Health Administration for personal exposures in the workplace. However, other metrics (i.e., number and surface area concentration) are increasingly considered better predictors of adverse health effects than mass concentration, especially for ultrafine and fine mode particles (Brouwer et al., 2004; Ramachandran, 2005; Ellenbecker and Tsai, 2015).

Commercial instruments provide a way to continuously assess aerosol concentrations of a given metric by size. Photometers continuously measure aerosol mass concentrations in environmental and occupational settings (Görner et al., 1995). Condensation particle counters (CPCs) assess aerosol number concentrations (Hering et al., 2005; 2014). Both type of instruments are portable and continuous, but provide limited size information on a single metric (e.g., number or mass concentration). Scanning mobility particle sizer (SMPS) and the aerodynamic particle sizer (APS) provide a continuous measurement of aerosol size distributions (Baron, 1986; Wang and Flagan, 1990), but are very expensive (~$50,000 to $100,000), large, and heavy. Moreover, none of these instruments provide information on particle composition.

Samplers that collect particles for subsequent chemical analyses can allow particle composition assessments. Size- and time-integrated samplers, such as the 37-mm filter cassette and inhalable IOM sampler, are widely used to measure personal exposures in the workplace (Demange et al., 2002), but yield only gross information on the size of the collected particles. Size-resolved and time-integrated devices, such as the nano micro-orifice uniform deposit impactor (nanoMOUDI) cascade, collect particles by aerodynamic particle size (Marple et al., 1986, 1991; Maenhaut et al., 1996). Although these instruments provide a way to measure mass concentration and particle composition, they do not provide continuous aerosol size distribution information. The electrical low pressure impactor (ELPI) can output continuous aerosol size distribution information, while simultaneously collecting particles for chemical analysis after sampling (Järvinen et al., 2017). However, the cost of the ELPI (>$100,000) precludes its widespread use in exposure assessment. There is no single portable instrument that continuously measure real-time aerosol size

distributions in various metrics (e.g., number, surface area and mass concentrations) and also collect particles by size for chemical analysis.

Our goal was to develop an instrument, the Portable Aerosol Collector and Spectrometer (PACS), to continuously measure aerosol size distributions by number, surface area and mass concentrations over a wide size range (from 10 nm to 10 μm) and to collect particles with impactor and diffusion stages for post-sampling chemical analyses. In Part I of this study, we describe the design and testing of the PACS hardware. In companion manuscripts, we describe a multi-modal fitting algorithm to enable continuous output of aerosol size distributions and associated laboratory tests comparing information on size and composition obtained with the PACS to reference instruments (SMPS, APS and Nano-MOUDI).

Methods

Portable Aerosol Collector and Spectrometer (PACS)

The PACS consists of four main parts (Figure 2-1): a particle size selector, a valve system, particle detectors (a photometer and water CPC [WCPC]), and controlling software running on a computer. Photographs of the prototype PACS and individual components are shown in Figure 2-2. Air transports aerosol through an electrically conductive tube to the inlet of the size selector at a flowrate of 0.7 L/min. Six independent valves of the valve system are controlled so that only one is open at a time. The open valve allows aerosol to pass from the inlet through a portion of the machined stages and then to a common manifold. The designed theoretical collection efficiencies by size are shown in Figure 2-3. We designed the selector to cover aerosols from 10 nm to 10 μm, enabling separation of ultrafine, fine and coarse mode particles. The aerosol then passes simultaneously to the

aerosol detectors, a photometer to measure mass concentrations and a WCPC to measure number concentrations. A full data collection sequence, sampling each size selector stage in turn, yields 12 measurements: six number concentrations and six mass concentrations.

Size Selector

The aluminum size selector consists of six stages in a series: a bypass stage, three impactor stages, and two diffusion stages (Figure 2-2). The first stage allows aerosol entering the inlet to freely pass through to the valve manifold. As shown in Figure 2-3, the next three stages were designed to collect particles by single-hole impactors with 50% stage cut-off aerodynamic diameters, d_{50}, of 10-µm, 1-µm, and 0.3-µm. These impactors were designed following well-established guidelines in Marple and Willeke (1976). Table 2-1 lists the dimensions of each impactor stage, including the nozzle width (W), the nozzle length (L), and the distance from impaction plate to nozzle (S). The nozzle width was selected to ensure a jet Reynolds number between 500 and 3000. For ease of sample recovery, the impaction plates consist of pre-oiled, porous plastic discs (9.5 mm diameter, Part # 225-388, SKC Inc., Eighty Four, PA, USA) pressed into a recess in the impactor plate assembly. A user can rapidly remove these discs with forceps for later chemical analysis of collected particles. The 1-µm impactor (Stage 2) removes coarse mode particles, allowing fine and ultrafine mode particles to pass; the 0.3-µm impactor (Stage 3) removes particles larger than 0.3 micrometers, simplifying the interpretation of the diffusion-stage results. (Figure 2-3; solid lines).

The two diffusion stages consist of circular, nylon meshes (41–µm net filters, Part # NY4104700, Carrigtwohill, Co. Cork, Ireland) held in place with a 47-mm filter holder. The meshes collect the smallest particles from the air stream by Brownian motion.

Following the theory of Cheng and Yeh (1980), we selected the one mesh to provide a d_{50} of 16 nm of geometric diameter for the first diffusion stage, and six meshes to provide a d_{50} of 110 nm of geometric diameter for the second diffusion stage (Figure 2-3; dashed lines). Together, the collection efficiency of the two diffusion stages was designed to match the nanoparticulate matter (NPM) sampling criterion. The NPM criterion was proposed by Cena et al. (2011) to collect nanoparticles by aerodynamic particle size with an efficiency that mimics their deposition in the human respiratory tract. Since the SMPS measures the particle equivalent mobility diameter, we converted the aerodynamic diameter of NPM to equivalent mobility diameter according to assumed particle density and shape factor from literature (Appendix C).

In theoretical calculations, we assumed standard temperature (20°C) and pressure (101.3 kPa), standard particle density (1000 kg/m^3), and a hydrodynamic factor of 0.0942. The theoretical penetration curves for impactor stages were calculated with the designed d_{50} and a sharpness of 1.15, following Hinds (1999). The particles that collect on the impactor and diffusion stages can be analyzed chemically (e.g., digestion followed by elemental analysis) to obtain a time-integrated measure of mass size distributions of various particle compositions, which is the subject of a companion manuscript.

Valve System

The valve system consists of six independent, custom pinch valves and a controller (Figure 2-2). The valve system, size selector and manifold are connected by six flexible plastic tubes (length = 46 mm, inner diameter = 4.76 mm, outer diameter = 6.35 mm; Tygon R-3603, VWR Scientific Inc., Rochester, NY, USA). The airflow path through the instrument was designed with few bends to minimize particle losses. Since the Bypass

Stage contains particles of all sizes, the airflow path flows without bend from the size selector to the photometer, minimizing particle loss from impaction (Figure 2-1). For other stages, the airflow has two 90-degree bends as it passes through the valve system and the manifold to the photometer. The airflow passes through an additional four bends on the way to the WCPC.

Each pinch valve includes a motor (Pololu 50:1 micro metal geared motor HP, Pololu Corporation, Las Vegas, NV, USA) connected to the pinch assembly. The direction of the current flow to the motor determines whether the assembly pinches the flexible tube open or closed. The amount of current delivered to the motor controls the magnitude of force applied to pinch the tubing. A custom circuit board designed using Multisim Version 13 (National Instruments Corporation, Austin, TX, USA) uses a microcontroller (Nano, Arduino, Ivrea, Italy) to process serial communications and appropriately signal the six motors through a motor driver (Pololu Dual H-Bridge Motor Driver, DRV8833, Texas Instruments, Dallas, Texas, USA). The board also supports the power regulation for all of these components.

Detectors

Two detectors were selected for the PACS: a photometer (SidePak AM510, TSI Inc., Shoreview, MN, USA) and WCPC (Box Magic, Aerosol Dynamics Inc., Berkeley, CA, USA) (Figure 2-2). Of the 0.7 L/min total flow, 0.4 L/min is directed to the photometer and the remaining 0.3 L/min to the WCPC. The photometer provides a continuous reading (time resolution of 1 sec) of mass concentration for aerosols from 0.1 to 10 μm. It uses a 670-nm laser diode to illuminate a portion of the aerosol flow. Set perpendicular to the illumination axis, the photometer's lens collects light scattered by the particles, focusing

the light on a photodetector, which generates a voltage proportional to the mass concentration. The SidePak photometer is portable and widely used to measure aerosol mass concentrations in outdoor and indoor environments (Klepeis et al., 2007; Jiang et al., 2011).

The laminar-flow WCPC, developed by Hering et al. (2014), provides a continuous measurement (time resolution of 1 sec) of number concentration for particles from 5 nm to 2 μm. Traditional WCPCs consist of a cool and wet wall (conditioner) followed by a warm and wet wall (growth region) that promotes condensation of water onto airborne particles (Hering et al., 2005). The WCPC used in this study replaces the "warm and wet wall (growth region)" of the traditional WCPC with two sections – a short warm and wet "initiator" (indicated in red in Figure 2-1) and a cool and wet "moderator" (indicated in green in Figure 2-1). The "initiator" provides the water vapor that creates the supersaturation, while the "moderator" provides the time for particle growth. As demonstrated by Hering et al. (2014) through modeling and laboratory tests, the new design reduces the added heat and water vapor while achieving the same peak supersaturation and similar droplet growth as the previous design. Therefore, the working time can be extended with the same amount of added water by consuming less power. Moreover, the WCPC is portable and operates independent of orientation. Two personal sampling pumps (GilAir PLUS, Gilian Instrument Corporation, Wayne, NJ, USA) provide airflow through the detectors. These external pumps were needed because the original pumps used in the SidePak AM510 and WCPC were not powerful enough to overcome the pressure drop caused by the small impactor nozzle in the size selector (Impactor Stage 3).

Controlling Software

A custom software program was developed using Visual Basic in Microsoft Visual Studio (VB.Net Version, Microsoft Corporation, Redmond, WA, USA) to control the timing of valves and to acquire data from the photometer and WCPC. The user defines the delay after a valve is opened and the duration over which concentrations are averaged (15 s in the current work). The program sequentially opens one valve at a time, collecting and storing six mean number concentrations and six mean mass concentrations for a single scan through all stages (3 min in the current work). It then calls a fitting algorithm, the subject of a companion manuscript, to translate these 12 measurements into aerosol size distributions of number, surface area and mass concentration. The program then displays these data graphically and numerically by particle size mode to the user.

Stage Penetration by Size

Following Sousan et al. (2016), we measured the penetration by size and pressure drop of each stage of the separator with the experimental setup shown in Figure 2-4. Room air was filtered with two high efficiency particulate air filters and passed into a chamber consisting of a mixing zone (0.64 m × 0.64 m × 0.66 m) and a sampling zone (0.53 m × 0.64 m × 0.66 m) divided by a perforated plate (600 evenly spaced 0.6-cm holes). Aerosol was injected into the mixing zone, where a small fan ensured that the aerosol was well mixed, and then passed through the perforated plate to provide a uniformly-distributed aerosol in the sampling zone.

We generated three aerosol types to span the range of interest. Fresh metal fume was produced with a spark discharge system (Park et al., 2014), providing an ultrafine

mode aerosol. A salt aerosol was generated using a Collision-type nebulizer (Aeroneb Solo Model, Aerogen, Martinez, CA, USA) with 0.9% salt solution, providing a fine mode aerosol. Arizona road dust (Fine Grade, Part # 1543094, Powder Technology Inc., Arden Hills, MN, USA) was aerosolized using a fluidized bed aerosol generator (3400A, TSI Inc., Shoreview, MN, USA), providing a coarse mode aerosol. We maintained steady aerosol concentrations ($8.2 \times 10^4 \pm 2.5 \times 10^3$ particles/cm^3 for fresh metal fume, $4.6 \times 10^4 \pm 8.7 \times 10^2$ particles/cm^3 for salt and $4.8 \times 10^2 \pm 8.7$ particles/cm^3 for Arizona road dust) throughout all tests.

We measured particle penetrations by size through each stage for each aerosol type six times (n = 6 stages × 3 aerosol types × 6 replications = 108 tests). Particle number concentrations by size were measured alternately entering the PACS and exiting the manifold after passing through the stage being measured. The number concentrations by equivalent mobility particle size were measured with an SMPS (SMPS 3936, TSI Inc., Shoreview, MN, USA) operated with a Nano DMA (DMA 3085, TSI Inc., Shoreview, MN, USA) for 5 nm to 20 nm and a long DMA (DMA 3081, TSI Inc., Shoreview, MN, USA) for 28 nm to 496 nm. The number concentrations by aerodynamic particle size were also measured with an APS (APS 3321, TSI Inc., Shoreview, MN, USA) for particles larger than 0.7 μm. The flowrate of the SMPS and APS were adjusted to achieve a total flowrate through the PACS of 0.7 L/min. The flowrate of the SMPS was set to 0.3 L/min. Filtered air was supplied at 4.6 L/min to the APS so that it sampled with a flowrate of 0.4 L/min.

The penetration for each size bin of the SMPS and APS was calculated as the number concentration exiting the outlet divided by that entering the inlet. We calculated

the R-squared (R^2) to evaluate how well the collection efficiency of particles to the meshes of the diffusion stages approximate the NPM curve as follows:

$$R^2 = 1 - \frac{\sum(NPM_j - measured_j)^2}{\sum(NPM_j - \frac{1}{j}\sum NPM_j)^2} \quad (2\text{-}1)$$

where j is the size bin, NPM_j and $measured_j$ are the theoretical and measured NPM data points, respectively.

Pressure Drop

We measured the pressure drop of each stage three times (n = 6 stages x 3 replicates = 18) with a pressure gauge (Model 407910, 0-200 kPa, Extech Instruments, Nashua, NH, USA) at a flowrate of 0.7 L/min. The pressure gauge was connected between the inlet and outlet of the valve manifold (dashed lines in Figure 2-4). Cumulative pressure drop was measured across the target stage.

Detector Response Time after Valve Switch

We measured the response time to achieve a stable number concentration after a valve switch (n = 6 stages x 3 replications = 18 tests). The response time is needed to set an appropriate delay before detector concentrations are used in calculations. We measured the response time for each stage using a mixed aerosol of fresh fume, aged metal fume, and Arizona road dust. As described above, fresh fume was produced with a spark discharge system to represent an ultrafine mode. Aged metal fume produced with a second spark discharge system was passed through two coagulation chamber in series (2 coagulation chamber × 200 L = 400 L) to allow the fume to age into a fine mode. Arizona road dust was aerosolized using a fluidized bed aerosol generator to represent the coarse mode. This

mixed aerosol was injected into the mixing/dilution chamber (Figure 2-4). The valves of the size selector were opened sequentially for 30 sec one at a time. For each stage, the response time was measured as the time to reach 95% of the steady-state number concentration by the WCPC after the valve for that stage was opened.

Results and Discussion

Stage Penetration by Size

Impactor Stages

Particle penetrations by aerodynamic particle size for bypass and impactor stages, and geometric particle size for diffusion stages are shown in Figure 2-5 and summarized in Table 2-1. SMPS measures the equivalent mobility diameter. I converted it to aerodynamic diameter using the equation and assumed particle densities and shape factors in Appendix C. Penetration is shown for particles smaller than 7 μm because number concentrations were unstable for larger particles. For each stage, we obtained penetration data. These measured penetrations are needed to improve estimates of aerosol size distributions. In all stages, diffusion losses were observed for small particles (< ~20 nm), and gravitational settling/impaction/interception losses were observed for large particles (> ~0.5 μm). For example, for the Bypass Stage (Figure 2-5a), the maximum penetration (~100% ± 3%) was observed for aerosols with diameters from ~20 nm to ~0.5 μm. For particles progressively smaller than ~20 nm, the penetration gradually decreased to ~58% (± 4%) for ~6 nm particles due to diffusion losses. For particles larger than ~0.5 μm, the penetration gradually decreased to ~72% (± 15%) for ~7 μm particles due to gravitational settling and impaction.

For particles progressively smaller than ~20 nm, the penetration of the 10-µm impactor (Stage 1, Figure 2-5b), gradually decreased from ~100% (± 10%) to ~88% (± 7%) for ~6 nm particles due to diffusion losses. The characteristic d_{50} of the Impactor Stage 1 was estimated to be ~10 µm of aerodynamic diameter with a sharpness (σ) of 2.6 (Table 2-1). More particle losses from diffusion were observed in the 1-µm impactor (Impactor Stage 2) than in the 10-µm impactor. For particles progressively smaller than ~20 nm, the penetration gradually decreased from ~90% (± 18%) to ~55% (± 5%) for ~6 nm particles (Figure 2-5c). The d_{50} of Impactor Stage 2 was ~1.0 µm of aerodynamic diameter with the σ of 1.6 (Table 2-1). In Impactor Stage 3 (Figure 2-5d), the penetration gradually decreased from ~100% (± 11%) to ~76% (± 9%) for particles from ~116 nm to ~9 nm. The d_{50} of this impactor was ~0.4 µm of aerodynamic diameter with the σ of 1.5 (Table 2-1). The Bypass Stage provided a collection efficiency curve similar to that of the 10-µm impactor and could potentially be eliminated in future versions of the PACS.

As expected, the measured characteristic d_{50} of each impactor stage was similar to the design (Table 2-1). In the impactor stages (Stage 1, 2 and 3), the number and mass concentrations can be detected for the particles smaller than 10 µm, 1.0 µm and 0.4 µm, respectively. The sharpness of the Stage 3 is similar to that of a previously reported nanosampler (NS, σ = 1.6; Tsai et al., 2012), a personal nanoparticle respiratory deposition sampler (NRD, sharpness = 1.53; Cena et al., 2011) and an Anderson cascade impactor using inertial filter technology (ANIF, sharpness = 1.6; Hata et al., 2012). The penetration curve of Impactor Stage 3 was sharper than that of the commercial NS of KANOMAX (sharpness = 1.9; KANOMAX, 2012) and less than that of either a personal nanoparticle sampler (PENS, sharpness = 1.3; Tsai et al., 2012) or a microorifice uniform deposit

impactor (MOUDI, sharpness = 1.2; Chen et al., 2016). Although high flowrates and low pressures are able to achieve sharper curves and reduce diffusion loss than in this study, they require large pumps which make the device less portable (Marple et al., 2001). The penetration curve of the last impactor stage of the PACS with sharpness of 1.5 is sufficiently sharp to remove particles larger than the ~300 nm from the airstream, and resolve uncertainties in data interpretation with the diffusion stages. More information about the design and test of the third impactor stage is shown in Appendix A.

The losses we observed for the impactor stages are similar to those observed for other devices. According to theory, particle losses occur due to gravitational settling, impaction, interception and diffusion (Hinds, 1999). Marple et al. (1991) studied the inter stage losses within the MOUDI, reporting that the losses were the greatest for the larger particles (~15 μm), where the gravitational settling and impaction were most severe. However, the losses rapidly decreased with progressive smaller particles to negligible particles less than 5 μm. The losses increased again as the particle size reached ~100 nm due to the diffusional effects of these small aerosols.

A knowledge of actual aerosol penetration by size in each stage is important to reduce uncertainties in estimating aerosol size distributions from PACS data. As described in Part III of this study, we incorporate the smoothed penetration curves, which include particle losses, for each stage into a multi-modal log-normal (MMLN) fitting algorithm. Shi et al. (1999) showed that particle loss caused by diffusion of ultrafine mode particles should be considered to obtain accurate aerosol size distributions with the SMPS. Reineking and Porstendörfer (1986) generally stressed that particle losses should be

incorporated in analysis routines to correct the raw measurements for any aerosol measurement instrument. The operation of the PACS will require this same correction.

Diffusion Stages

Penetration by geometric particle size for the diffusion stages are shown in Figure 2-5e and 2-5f. Since most of particles (97 ± 3%) larger than 500 nm were removed by the 0.3-µm impactor (Figure 2-5d), only particles smaller than 500 nm are shown in Figure 2-5e and 2-5f. For the first diffusion stage with one mesh (Stage 4, Figure 2-5e), penetration was highest (99% ± 7%) for particles from ~300 nm to 400 nm and gradually decreased with decreasing particle size (< 40% for particles smaller than 10 nm). The measured d_{50} of the first diffusion stage was ~16 nm of geometric diameter (Table 2-1). For the second diffusion stage with 6 meshes (Stage 5, Figure 2-5f), penetration gradually decreased from ~100% for particles of ~400 nm to ~8% for particles of ~15 nm. The measured d_{50} of the second diffusion stage was ~56 nm of geometric diameter (Table 2-1). As expected, the measured characteristic d_{50} of each diffusion stage was similar to the design. The penetrations in diffusion stages can be used to provide size information for particles less than 300 nm. In the last stage, since less than 10% of particles smaller than 10 nm can penetrate the 6 meshes, the lower size limit of the PACS measurement was set at 10 nm.

The effective collection efficiency by equivalent mobility particle size of particles to the two diffusion stages combined (Stages 4 and 5) is shown in Figure 2-6 (black dots). The collection efficiency was lowest (15% ± 10%) for ~300 nm particles, where the last impactor collects the particles larger than this size, and gradually increased with decreasing particle size. This combined collection efficiency is similar to the NPM sampling criterion (solid line) with R^2 of 0.97. This criterion represents the deposition of nanoparticles in the

human respiratory tract (Cena et al., 2011). Thus, the mass of aerosols chemically analyzed on the two diffusion stages can be added to estimate the nanoparticles that deposit in human respiratory system. Few examples of samplers with efficiencies matching respiratory deposition can be found in literature. The size-selective inlet (Kuo et al., 2005), multistage sampler (Koehler et al., 2009) and NRD sampler (Cena et al., 2011) were designed to mimic a modified ICRP lung deposition fraction. However, the size-selective inlet only simulates the fraction reaching the ciliated regions of the lungs, the multistage sampler mimics the total particle deposition in the human respiratory tract (not specifically for nanoparticles), and the NRD sampler provides only nanoparticle mass concentration, is unable to provide the information for fine and coarse mode.

Pressure Drop

The measured cumulative pressure drop for each PACS stage is listed in Table 2-1. The highest pressure drop (2.23 kPa) was caused by the third impactor, followed by the second impactor (0.65 kPa). The pressure drop caused by other stages were negligible (~0 kPa). Overcoming the system pressure drop is critical to maintaining a stable flowrate. The pumps originally used in the photometer and WCPC were unable to maintain the design flowrate of 0.7 L/min due to the pressure drop imparted by the 300-nm impactor. The external air pumps (the portable GilAir PLUS air pumps) used in the final PACS design are able to overcome this pressure drop without faulting due to low system flowrate requirement (Appendix B). These external pumps can be replaced with a single pump internal to the PACS in future versions.

Detector Response Time after Valve Switch

The number and mass concentrations of the combined test aerosol measured by the detectors after passing through each stage are shown in Figure 2-7. The time to achieve 95%-105% of steady-state number concentrations for each stage is shown in Table 2-1. As expected, the number concentration was more stable than the mass concentration because the metal fume generated by the spark system is more stable than the Arizona dust generated by the fluidized bed aerosol generator. For the Bypass Stage, the number concentration went above steady-state because of the transition from the high pressure drop downstream of the 300-nm impactor to the low pressure drop of the Bypass Stage. This larger pressure change caused the air flowrate to become higher than 0.7 L/min, thereby causing the WCPC to erroneously read higher concentrations. As a result, the Bypass Stage had the longest response time (15 ± 4 sec). The response time of Stage 1 (7 ± 1 sec) was ~50% faster than that of the Bypass Stage, because there was little pressure drop in this stage. Due to the pressure drop added by Stage 2 and 3, the WCPC response time increased by a few seconds (totaling 10 ± 1 sec for Stage 2 and 8 ± 2 sec for Stage 3). For the two diffusion stages (Stage 4 and 5), the WCPC response times were 8 ± 1 sec and 6 ± 0 sec, respectively.

There are three factors for determining the response time: 1) opening and closing valves; 2) response of the pumps to recover from pressure drop released by the stage; and 3) the clearing of the volume of air between the exit of the stage and the detector. Valve opening and closing is fairly rapid (~3 sec), so unlikely to be the largest contributor to overall response time. The time for the pumps to regain airflow is dependent on the pressure drop added/released by stage. Based on the airflow and the air volume between the exit of

the stage and the WCPC, the estimated time for clearing the volume of air between the exit of the stage and the detector is ~3 sec for the Bypass Stage, ~3.1 sec for the Stage 1, ~3.3 sec for the Stage 2, ~3.4 sec for the Stage 3, ~3.4 sec for the Stage 4, and ~3.5 sec for the Stage 5.

These time delays and the associated averaging time define the minimum time required to obtain a full set of measurements with the PACS. If the averaging time is 15 sec, then the minimum time required to obtain a set of measurements over all stages was 144 sec.

PACS in Context of Commercial Instruments

In a single portable instrument, the PACS provides a way to continuously measure aerosol size distributions of number, surface area, and mass concentration over a wide size range while simultaneously collecting particles with impactor and diffusion stages for chemical analysis. The ELPI, an instrument that retails for ~$120,000, is the only other single instrument with similar capabilities. However, the low pressure impactor stages used to achieve separation of sub-300-nm particles of the ELPI are expensive to manufacture and require a large, heavy vacuum pump, which dramatically reduces the portability of the system. The reliance on diffusion stages to separate these sized particles in the PACS dramatically reduces the cost of size separation and eliminates the need for high vacuum pumps, thereby promoting portability. Further we envision that the PACS size selector can be made by injection molding of conductive plastic instead of aluminum, enabling extremely less expensive size separation, reducing size and weight. Whereas the ELPI relies on highly sensitive electrometers to measure the concentration of particles, the detectors employed in the PACS (a photometer and a WCPC with a commercial cost of

~$15,000) are substantially less inexpensive and have been shown robust in field use. Moreover, we envision that these detectors could be combined in a commercial PACS version, further reducing costs associated with redundant user interfaces and pumps.

Similar information can also be obtained with multiple research-grade instruments, such as the combination of an SMPS, APS and nanoMOUDI (~$150,000 in total). Researchers combine the SMPS and APS to measure aerosol size distributions over a wide range (Harrison et al., 2000). The wide range aerosol spectrometer (WRAS, Grimm Technologies Inc., Douglasville, GA, USA) combines the portable aerosol spectrometer, differential mobility analyzer, and CPC to measure aerosol size distributions from ~5nm to ~32 μm. The wide-range particle spectrometer (WPS^{TM}) introduced by Liu et al. (2010) can measure aerosol size distributions from ~10 nm to ~10 μm by combining a scanning mobility spectrometer (SMS) and a laser particle spectrometer (LPS). These systems lack the ability to collect particles for chemical analysis, thereby requiring another instrument like the nanoMOUDI. In addition, the particles deposit on the PACS diffusion stages can be analyzed to determine the nanoparticles that deposit in human respiratory system.

Nevertheless, the PACS also has some limitations that constrain its intended use to measure continuous aerosol size distributions. As shown in Figure 2-7, 180 sec is required for one measurement using the current prototype. If the aerosol concentrations are rapidly changing at the measurement site, the aerosol size distribution measurements might not be accurate. The flowrate is only 0.7 L/min, which might require a long time sampling to collect sufficient particles on the substrates to be detectable. An alternative scheme of reducing the sampling time is to measure the number and mass concentrations in all stages simultaneously by including additional detectors to the outlet of each stage.

In this work, we describe the design and testing of a Portable Aerosol Collector and Spectrometer, the PACS. The PACS continuously measures aerosol size distributions by number, surface area and mass concentrations over a wide size range (from 10 nm to 10 μm), and collect particles with impactor and diffusion stages for post-sampling chemical analyses. The penetration by size in all six stages were measured experimentally to have characteristic d_{50} (aerodynamic diameter for impactor stages and geometric diameter for diffusion stages) similar to the design. The deposition to the two diffusion stages was in agreement with the NPM sampling criterion. The pressure drop of each stage was sufficiently low to permit its operation with portable air pumps. In the current configuration, the number and mass concentrations from all six stages can be measured in approximately 180 sec. With the data analysis methods introduced in Part II paper of this study, the PACS can provide novel exposure assessments, including aerosol size distributions of number, surface area and mass concentrations in a wide size range (from 10 nm to 10 μm).

Table 2-1: Physical characteristics, flow parameters and experimental results for the PACS stages.

Stage	Physical Characteristics			Flow Parameters		Design	Experimental Results				
	W (mm)	*L* (mm)	*S/W*	*Re*	*V* (cm/sec)	d_{50} (µm)	d_{50} (µm)	Stk_{50}	σ	ΔP (kPa)	*Response* (s)
Bypass stage 0	n.a.	n.a.	n.a.	n.a.	n.a.	n.a.	n.a.	n.a.	n.a.	0	15 ± 4
Impactor stage 1	3.15	4.47	2.78	313	150	10[a]	~10[a]	0.22	2.6	0	7 ± 1
Impactor stage 2	0.67	2.70	6.81	1470	3309	1.0[a]	1.0[a]	0.22	1.6	0.65	10 ± 1
Impactor stage 3	0.48	0.48	5.67	2051	6447	0.3[a]	0.4[a]	0.22	1.5	2.88	8 ± 2
Diffusion stage 4	n.a.	n.a.	n.a.	25	n.a.	0.016[b]	0.016[b]	n.a.	n.a.	2.88	8 ± 1
Diffusion stage 5	n.a.	n.a.	n.a.	25	n.a.	0.110[b]	0.056[b]	n.a.	n.a.	2.88	6 ± 0

Notes: *W* – the nozzle width; *L* – the nozzle length; *S* – the distance from impaction plate to nozzle; *Re* – Reynolds number; d_{50} – 50% stage cut-off diameter; Stk_{50} – Stokes number at 50% collection efficiency; σ – curve sharpness; ΔP – cumulative pressure drop; *V* – nozzle velocity; a – aerodynamic diameter; b – geometric diameter; n.a. – not applicable.

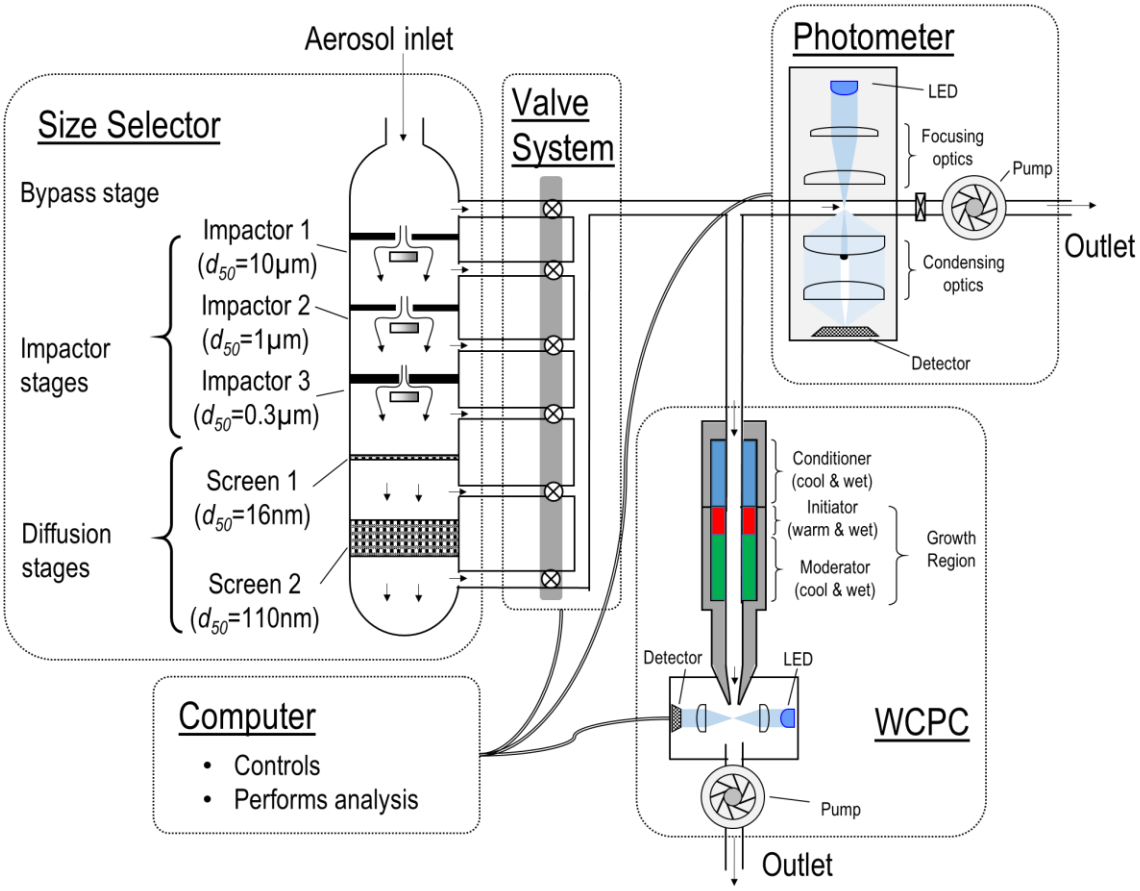

Figure 2-1: Schematic diagram of the PACS with major components identified.

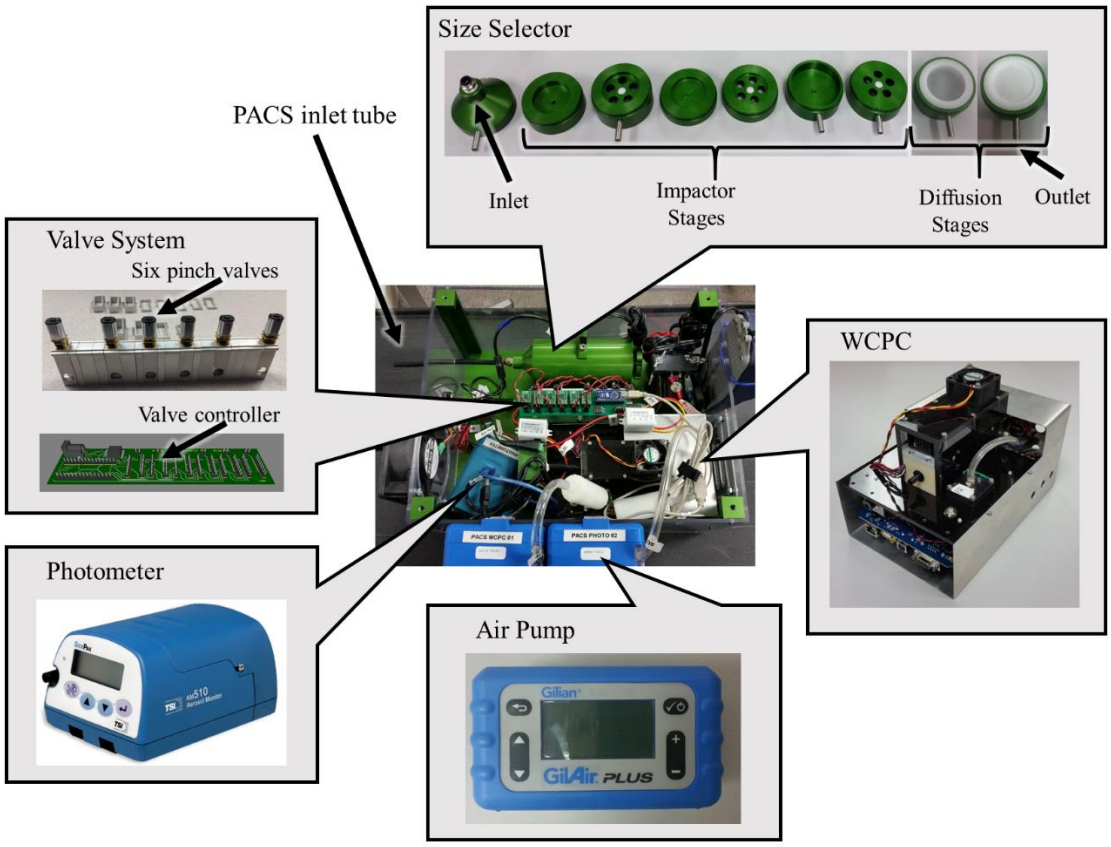

Figure 2-2: Photographs of the PACS, showing the assembled instrument (center) and each component around the perimeter.

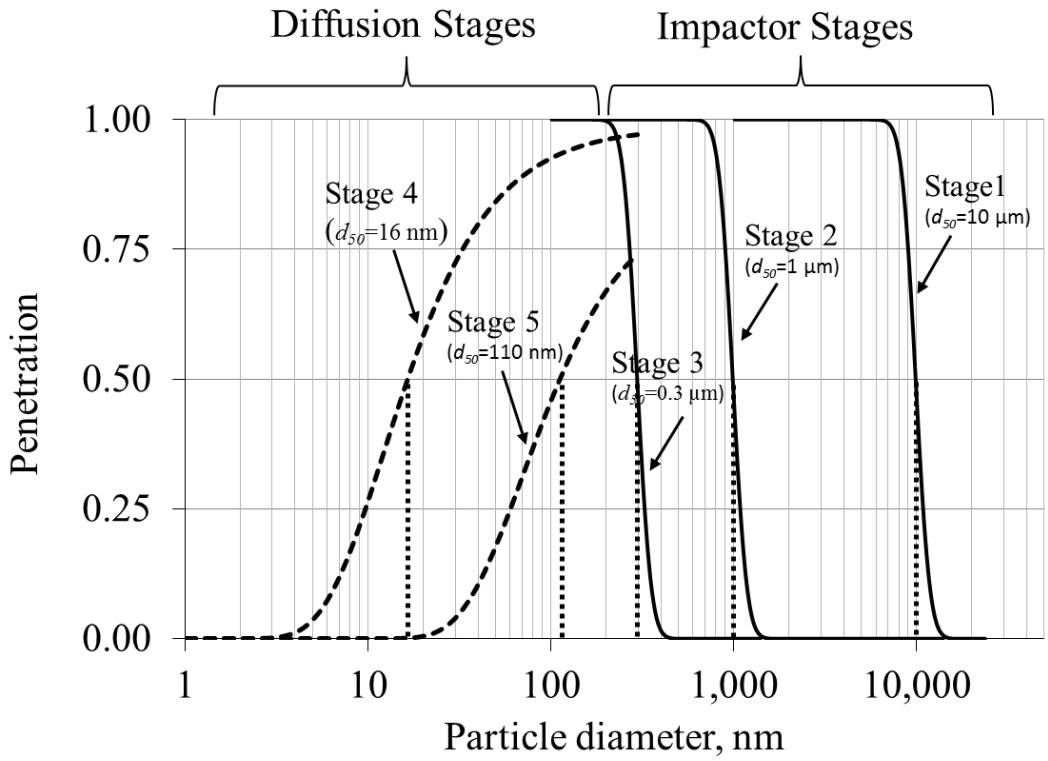

Figure 2-3: Theoretical penetration by particle diameter for each of the PACS impactor stages (aerodynamic diameter, solid lines) and diffusion stages (geometric diameter, dashed lines). Stage 0, the bypass stage, is not shown.

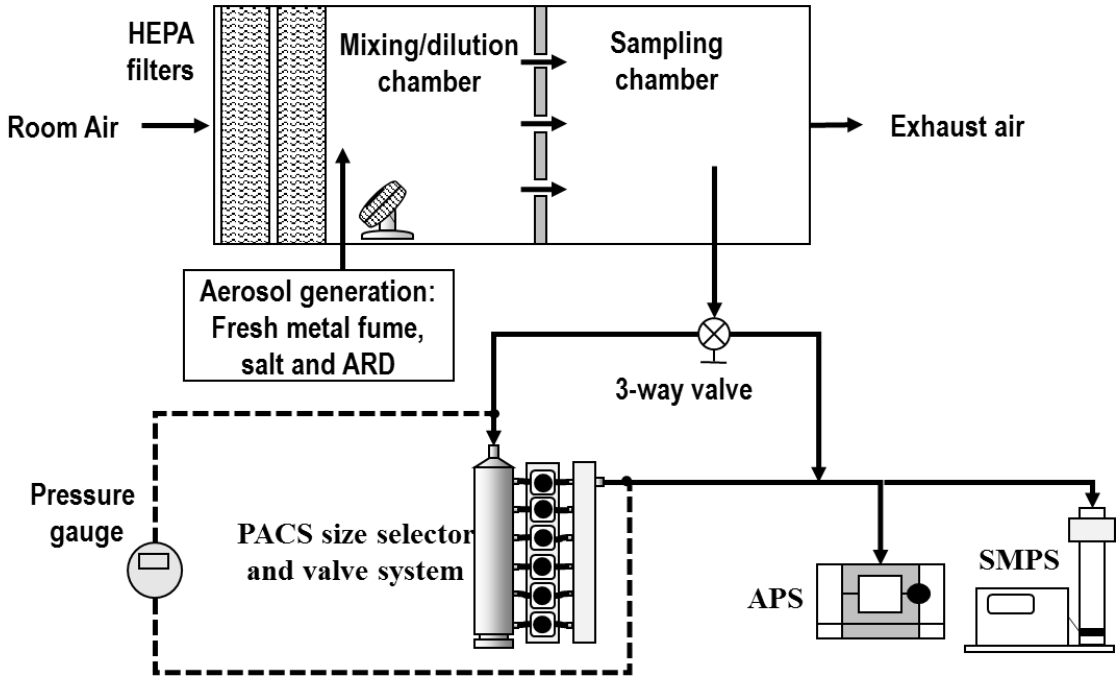

Figure 2-4: Experimental setup used to measure particle penetration by size and pressure drop.

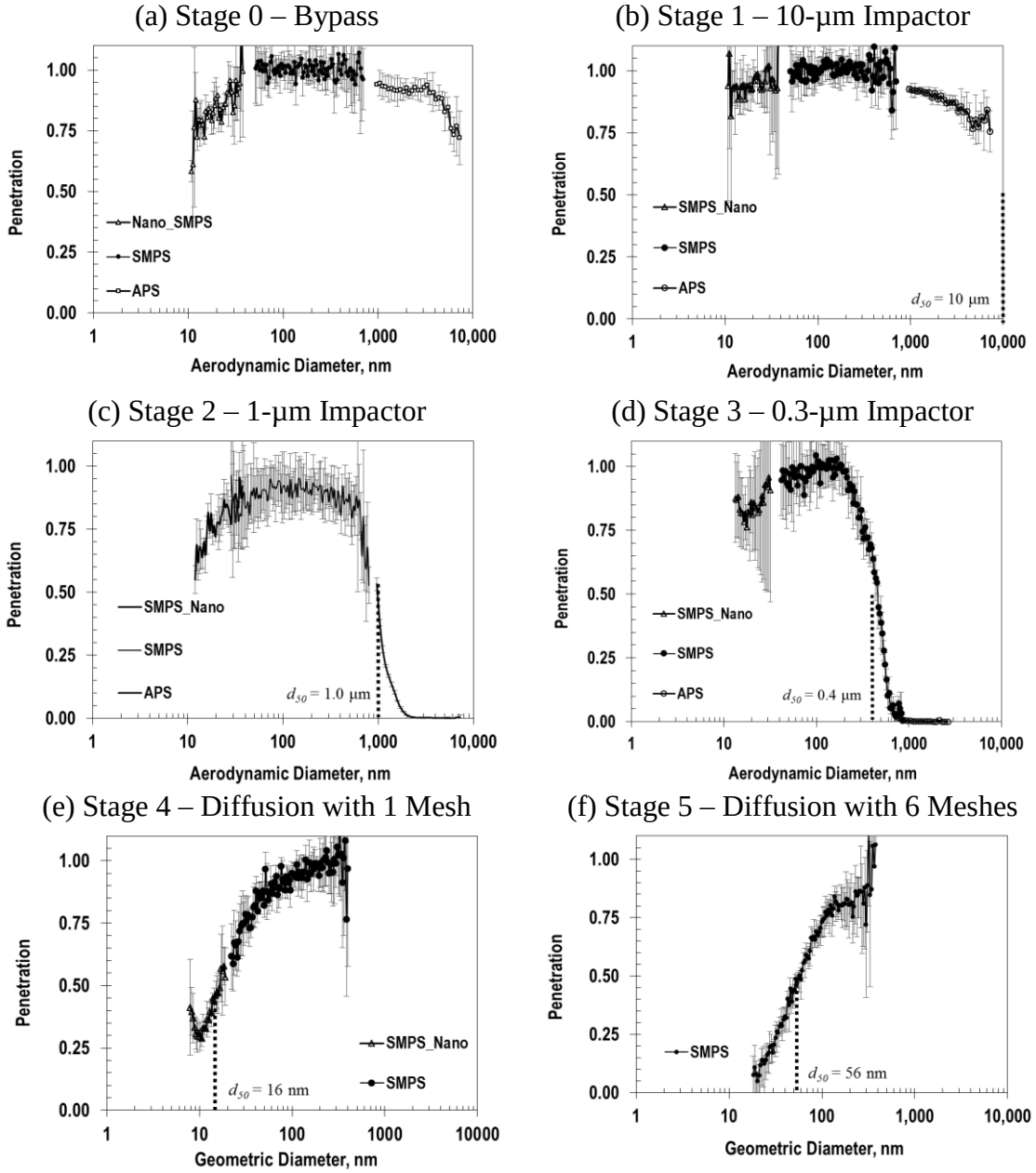

Figure 2-5: Fractional penetration measured for the six PACS stages (error bars represent the standard deviation of six measurements; dashed line indicates the measured d_{50}).

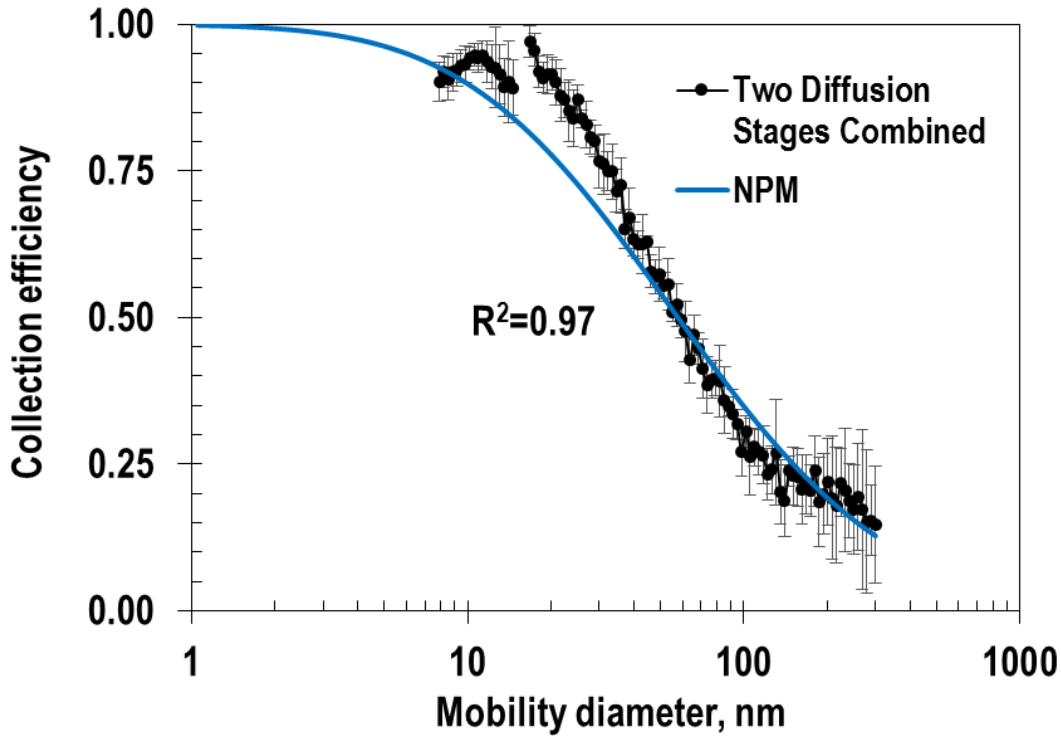

Figure 2-6: Effective collection efficiency of the two diffusion stages of the PACS (error bars represent the standard deviation of six measurements) shown with the nanoparticulate matter (NPM) sampling criterion.

(a)

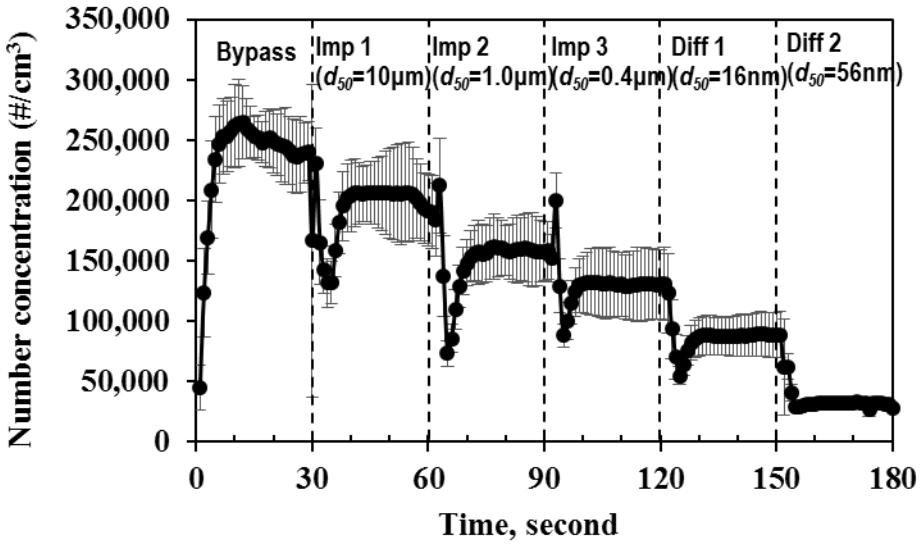

(b)

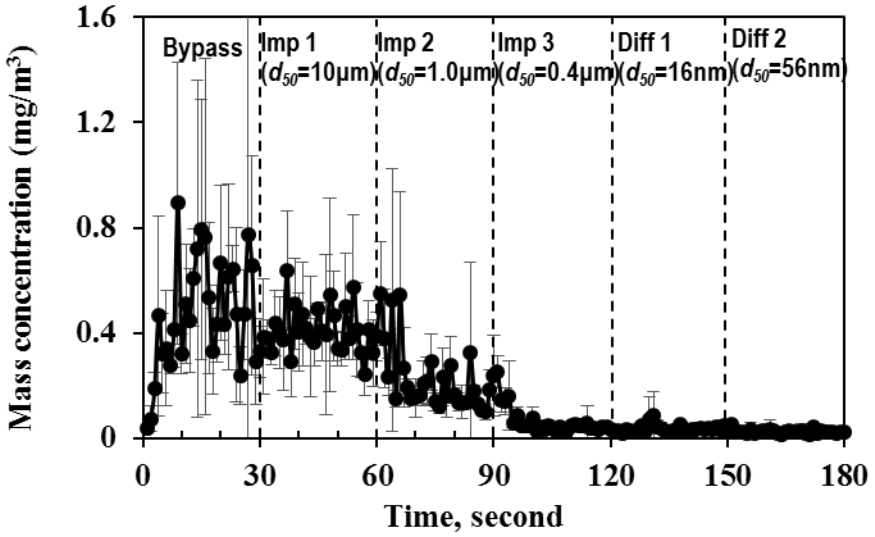

Figure 2-7: Number concentrations from the WCPC (a) and mass concentrations from the photometer (b) for the combined aerosols of fresh metal fume, aged metal fume and Arizona road dust (error bars represent the standard deviation of three measurements).

CHAPTER III

DEVELOPMENT OF A

PORTABLE AEROSOL COLLECTOR AND SPECTROMETER (PACS)

PART II: ALGORITHM TO ESTIMATE SIZE DISTRIBUTIONS

Abstract

Previously in Part I of this study, we described a Portable Aerosol Collector and Spectrometer (PACS) that consists of a six-stage particle size selector, a valve system, a water condensation particle counter to detect number concentrations and a photometer to detect mass concentrations. Here in Part II, we present an algorithm to leverage the multi-metric, low-resolution data from one sequence of PACS measurements (six number and six mass concentrations) to estimate the number, surface area, and mass concentration highly resolved by aerodynamic particle size ranging from 10 nm to 10 μm in near real-time. The algorithm uses a grid-search process and a constrained linear least-square (CLLS) solver to find a tri-mode (ultrafine, fine, and coarse), log-normal distribution that best fits the input data. We refined the algorithm to obtain accurate and precise size distributions for four aerosols typical of diverse environments: clean background, urban and freeway, coal power plant, and marine surface. Sensitivity studies were conducted to explore the influence of unknown particle density (range from 500 to 3000 kg/m^3) and shape factor (range from 1.0 to 3.0) on algorithm output. An adaptive process that refined the ranges and step sizes of the grid-search reduced the computation time to fit a single size distribution from 43.3 ± 29.0 min to 24.3 ± 11.4 sec. Assuming standard density spheres, the aerosol size distributions fit well with the *normalized mean bias* of -4.9% to 3.5%, *normalized mean error* of 3.3% to 27.6%, and R^2 values of 0.90 to 1.00. The fitted number

and mass concentration biases were within ±10% regardless of uncertainties in density and shape. However, fitted surface area concentrations were more likely to be underestimated for particle density less than 1000 kg/m^3 and shape factor larger than 1, and overestimated for particle density larger than 1000 kg/m^3. With this algorithm, the PACS is able to estimate aerosol size distributions by number, surface area, and mass concentrations from 10 nm to 10 μm in near real-time.

Introduction

Adverse health effects from the inhalation of particles are determined by particle size, shape, composition, and either number, surface area or mass concentration (Harrison and Yin, 2000). Commercial instruments designed to assess such aerosol exposures have important practical limitations. Handheld survey instruments, which typically cost less than $10,000, measure either number or mass concentrations but do not discriminate among particles of different size. Condensation particle counters (CPCs) measure number concentration summed from ~10 nm to ~1,000 nm (Hering et al., 2005; 2014), while photometers measure mass concentration aggregated across sizes ranging from ~300 nm to ~10,000 nm (Görner et al., 1995). Particle sizers are a different class of instrument that also measure particle number concentrations, but discriminate size with high resolution (>16 size bins per decade). Particle sizers require different technologies to assess different particle scales. Scanning mobility particle sizers (SMPS) measure sub-micrometer aerosols by equivalent mobility diameter (Wang and Flagan, 1990). Optical particle counters measure particles larger than 300 nm (Jaenicke, 1972), and time-of-flight instruments, such as aerodynamic particle sizer (APS), measure particles larger than ~700 nm of aerodynamic diameter (Baron, 1986). However, the multiple research instruments required to measure

concentrations over a wide size range (10 nm to 10,000 nm) are expensive (>$60,000), bulky, and heavy. Moreover, estimates of surface area and mass concentrations measured by these instruments are subject to the uncertainties of unknown density and shape factor. Portable electrical low pressure impactors provide aerosol concentrations highly resolved by size over a wide range, while simultaneously collecting particles that can be analyzed to determine shape factor and composition (Keskinen et al., 1992; Marjamäki et al., 2000). These impactors, however, are expensive (>$100,000), and real-time estimates of size distributions by different metrics are still subject to uncertainties introduced by unknown density and shape factor.

In Part I of this study, we described the hardware of a new portable device—the Portable Aerosol Collector and Spectrometer (PACS)—that measures aerosol size distributions of number, surface area, and mass concentrations in near real-time, and collects particles with impactor and diffusion stages for chemical analysis (Chapter II). The PACS consists of a six-stage particle size selector, a valve system, a water condensation particle counter to detect number concentrations, and a photometer to detect mass concentrations. The valve system diverts airflow sequentially through each stage of the selector to the detectors. The first stage allows particles entering the inlet to freely pass through to the detectors. Each subsequent stage removes a fraction of particles according to their size. Three impactor stages collect particles by single-hole impactors with 50% stage cut-off diameters, $d_{50,s}$, of 10-µm, 1-µm, and 0.3-µm of aerodynamic diameter. The last two stages collect particles by diffusion with $d_{50,s}$ of 16 nm and 110 nm of geometric diameter, respectively. A software program samples the particles at each stage by sequentially opening one valve at a time for 30 sec. A complete, 180 sec cycle yields 12

measurements: six number and six mass concentrations. We anticipate that a commercialized version of the PACS would cost between $10,000 and $20,000 given that the detectors are similar to those used in handheld survey technology.

Aerosols can be mathematically described by multi-modal log-normal (MMLN) distributions. Whitby (1978) used a tri-modal distribution consisting of a nuclei mode (0.005 ~ 0.1 μm), an accumulation mode (0.1 ~ 2 μm), and a coarse mode (greater than 2 μm) to describe measured size distributions of ambient aerosols. Each mode has a log-normal function with three parameters: geometric mean diameter (*GMD*), geometric standard deviation (*GSD*), and volume of particles per volume of air. Whitby and Sverdrup (1980) showed that this tri-modal, log-normal distribution could describe aerosols from diverse settings, including rural environments, freeways, and even emissions from coal fired power plants. Other researchers have also found tri-modal log-normal distribution to fit measured aerosol size distributions well (Wilson and Suh, 1997; Hussein et al., 2005; Liu et al., 2008).

Mathematical algorithms have been developed to fit size-resolved aerosol data. Twomey (1975) compared two algorithms that estimated the parameters of a bimodal aerosol number distribution from aerosol measurements using diffusion batteries. His iterative, nonlinear algorithm out-performed his constrained, linear inversion algorithm when the measurements extended over a wide dynamic range. However, solutions from his iterative algorithm tended to oscillate rather than consistently moving toward a unique solution. Markowski (1987) refined Twomey's algorithm with a mathematical smoothing technique designed to minimize the oscillation. Maher and Laird (1985) developed an expectation-maximization algorithm to fit an aerosol size distribution for the ultrafine

mode from diffusion battery data. This algorithm provides a unique solution vector, which guarantees a nonnegative concentration. Wolfenbarger and Seinfeld (1990) developed an inversion algorithm based on regularization to find smooth size distributions that represent data measured by multiple instruments (such as a diffusion batteries, OPCs, DMAs and low pressure impactors). The size range of fitted aerosol size distributions covered from 1 nm to 10 μm. Hussein et al. (2005) developed an algorithm to fit the aerosol number size distributions automatically without knowing the number of modes. Taylor et al. (2014) applied a Gaussian mixture model to fit aerosol data obtained from the Aerosol Robotic Network, which measure atmospheric aerosol properties using sun photometers.

Size distributions of one metric can be converted to those of other metrics. For the SMPS and APS size distribution data, users converted raw count data to number, surface area and volume concentrations (Abt et al., 2000). However, uncertainties in sizing and concentration made with the original measurements are exacerbated in the conversion. For example, the smallest mode in the atmospheric aerosol, in term of mass concentration, is the nuclei mode, which may contain the highest number of particles. Consequently, number concentrations of nuclei mode particles are subject to large uncertainty when transforming from instruments that provide the mass concentration of an aerosol by size (e.g., the cascade impactor) (Whitby, 1978). The combination of data from instruments providing aerosol size distributions in multiple metrics may potentially reduce the uncertainties in estimating accurate size distributions over a wide size range.

In Part II of this study, we describe a MMLN fitting algorithm that leverages the multi-metric, low-resolution data from one sequence of PACS measurements to estimate aerosol size distributions of number, surface area, and mass concentration from 10 nm to

10 μm in near real-time. The aerosols are then classified into three size modes: (1) ultrafine mode (i.e., 0.01 ~ 0.1 μm, nanoparticles); (2) fine mode (i.e., 0.1 ~ 1 μm, fine particles); and (3) coarse mode (i.e., 1 ~ 10 μm, coarse particles). We refined the algorithm to obtain accurate and precise size distributions for four aerosols (clean background, urban and freeway, coal power plant, and marine surface). We also conducted a sensitivity study to assess the influence of unknown particle density and shape factor on the algorithm output.

Methods

Description of the Algorithm

The fitting algorithm developed to determine the continuous aerosol size distributions of number (*N*), surface area (*SA*), and mass (*M*) concentrations from PACS measurements consists of two main steps (Figure 3-1). The core parts of the fitting algorithm code are shown in Appendix D. The inputs are the six observed number concentrations ($N_{obs,k}$) and six observed mass concentrations ($M_{obs,k}$) in each stage k (k = 0 to 5) of the size selector obtained from one cycle of the PACS measurement. We used a tri-modal, log-normal distribution to mathematically express an aerosol (Whitby, 1978):

$$f(d_p, N_i, CMD_i, GSD_i) = \sum_{i=1}^{3} \frac{N_i}{\sqrt{2\pi}\ln(GSD_i)} \exp\left[-\frac{[ln(d_p)-ln(CMD_i)]^2}{2ln^2(GSD_i)}\right] \quad (3\text{-}1)$$

where i is the aerosol mode ($i=1$ represents the ultrafine mode, $i=2$ represents the fine mode and $i=3$ represents the coarse mode), N is the number concentration; *CMD* is the count median diameter; *GSD* is the geometric standard deviation, and d_p is the aerodynamic particle diameter.

In Step 1, we estimate N_i, GSD_i and CMD_i by a grid-search process. For *GSD*, we set the step size to 0.1 independent of mode and the range as follows: ultrafine mode between 1.5 and 1.8; fine mode between 1.8 and 2.2; and coarse mode between 2.1 and 2.7. For *CMD*, we set the step size and range as follows: ultrafine mode between 5 nm and 40 nm with a step size of 5 nm; fine mode between 40 nm and 200 nm with a step size of 50 nm; and coarse mode between 0.4 μm and 2 μm with a step size of 0.5 μm. These ranges were selected to encompass diverse aerosols reported on by Whitby and Sverdrup (1980).

For simplicity, we re-write Eq. 3-1 as two equations:

$$f\left(d_p, N_i, CMD_i, GSD_i\right) = \sum_{i=1}^{3} N_i A_i\left(d_p, CMD_i, GSD_i\right) \tag{3-2}$$

$$A_i\left(d_p, CMD_i, GSD_i\right) = \frac{1}{\sqrt{2\pi}\ln(GSD_i)} \exp\left[-\frac{\left[ln(d_p) - ln(CMD_i)\right]^2}{2ln^2(GSD_i)}\right] \tag{3-3}$$

where $A_i\left(d_p, CMD_i, GSD_i\right)$ is a frequency distribution of an aerosol mode *i*. Using an optimization method described by Hussein et al. (2005), we estimate the number concentration in each mode (N_i) using number and mass concentration measurements. We calculate the squared error between observed ($N_{obs,k}$) and fitting number concentration ($N_{fit,k}$), and then set the partial derivative of the square effort with respect to N_i to zero (Eq. 3-4):

$$\frac{\partial}{\partial N_i} \sum_{k=0}^{5} (N_{obs,k} - N_{fit,k})^2 = 0 \tag{3-4}$$

where $N_{fit,k}$ is the number concentration fit by the algorithm in each PACS stage *k* (*k* = 0 to 5). For the first stage, $N_{fit,k}$ is calculated as:

$$N_{fit,k} = \int_0^{\infty} [\sum_{i=1}^{3} N_i A_i\left(d_p, CMD_i, GSD_i\right)] d\left(ln\left(d_p\right)\right), (k = 0) \tag{3-5}$$

For subsequent stages, $N_{fit,k}$ is computed as the penetration through the previous stage, P_{k-1}, multiplied by the number concentration entering the previous stage:

$$N_{fit,k} = P_{k-1}N_{fit,k-1}, (k = 1\ to\ 5) \tag{3-6}$$

We also set the partial derivative of the squared difference between observed ($M_{obs,k}$) and fitting mass concentration ($M_{fit,k}$) with respect to N_i to zero (Eq. 3-7):

$$\frac{\partial}{\partial N_i}\sum_{k=1}^{6}(M_{obs,k} - M_{fit,k})^2 = 0 \tag{3-7}$$

where $M_{fit,k}$ is the mass concentration fit by the algorithm in each PACS stage *k*. For the first stage, $M_{fit,k}$ is calculated as:

$$M_{fit,k} = \int_0^{\infty}\left[\sum_{i=1}^{3} N_i m_i A_i\left(d_p, CMD_i, GSD_i\right)\right] d\left(ln\left(d_p\right)\right), (k = 0) \tag{3-8}$$

where m_i is the mass of one particle with the size of averaged mass diameter (AMD_i) in mode *i*. To calculate m_i, the Hatch-Choate equation is applied to convert CMD_i to the particle diameter associated with the average mass of all particles in a mode (AMD_i) as (Hinds 1999):

$$AMD_i = CMD_i exp(1.5ln^2 GSD_i) \tag{3-9}$$

$$m_i = \rho\frac{\pi}{6}AMD_i^3 \tag{3-10}$$

where ρ is the particle density.

For subsequent stages, $M_{fit,k}$ is computed as the penetration through the previous stage, P_{k-1}, multiplied by the mass concentration entering the previous stage:

$$M_{fit,k} = P_{k-1}M_{fit,k-1}, (k = 1\ to\ 5) \tag{3-11}$$

We applied the CLLS solver, *lsqlin*, in MATLAB (MATLAB, 2014) to solve for N_i, using the 12 linear equations (Eq. 3-5, 3-6, 3-8 and 3-11) as equality constraints. A constraint of $N_i > 0$ is added to prevent obtaining negative values of N_i.

We then calculate bias of number and mass concentration in each PACS stage *k* as $(N_{fit,k} - N_{obs,k})/N_{fit,k}$ and $(M_{fit,k} - M_{obs,k})/M_{fit,k}$, respectively. The log-normal parameters (N_i, CMD_i and GSD_i) are saved when the bias in each stage are smaller than a certain tolerance (i.e., within ± 10% for the first stage, ± 50% for the second stage, and ± 100% for other stages). The Environmental Protection Agency (EPA) and National Institute for Occupational Safety and Health (NIOSH) specified that the acceptance criteria of percent bias should be within ± 10% (EPA 2006; NIOSH 2012). Therefore, the ±10% tolerance for the first stage ensures that the number and mass concentrations measured by the PACS meet these acceptance criteria. After completing the grid-search ranges of GSD_i and CMD_i, the averaged GSD_i and CMD_i are calculated from saved values.

In Step 2, we refine the estimates of N_i, GSD_i and CMD_i by narrowing the grid-search ranges of GSD_i and CMD_i, and decreasing the step size of CMD_i. Then Step 1 is repeated until the step size of CMD_i equals 0.1×10^i nm (i.e., 1 nm for ultrafine mode, 10 nm for fine mode, and 100 nm for coarse mode). We estimate the log-normal parameters (N_i, CMD_i and GSD_i) by minimizing the sum of the squared relative errors (*SSREs*) between the measurements and fitting results (2 measurements [*N* and *M*] × 6 stages = 12 *SSREs*).

$$SSRE = \sum_{k=1}^{6}\left(\frac{N_{obs,k}-N_{fit,k}}{N_{obs,k}}\right)^2 + \sum_{k=1}^{6}\left(\frac{M_{obs,k}-M_{fit,k}}{M_{obs,k}}\right)^2 \quad (3\text{-}12)$$

Then, we applied the Hatch-Choate equation to convert CMD_i and GSD_i to the surface area median diameter (SMD_i) and mass median diameter (MMD_i) as (Hinds 1999):

$$SMD_i = CMD_i exp(2ln^2 GSD_i) \quad (3\text{-}13)$$

$$MMD_i = CMD_i exp(3ln^2 GSD_i) \quad (3\text{-}14)$$

Lastly, for each metric (*N*, *SA* and *M*), the algorithm outputs: 1) aerosol size distribution from 10 nm to 10 μm resolved in 40 size bins for each decade of data; 2) summary statistics (*CMD, SMD, MMD, GSD, N, SA, M*) for each mode.

Algorithm Refinement

We conducted tests to determine the step size and range for the grid-search of CMD_i that provides accurate and precise size distributions for four pre-defined typical atmospheric aerosols (including clean continental background, urban and freeway, coal power plant and marine surface aerosols, see Table 3-1). These four pre-defined aerosols were selected from Whitby and Sverdrup (1980) to encompass a wide range of size distributions encountered in the atmosphere. For example, the clean continental background aerosol was used to test the accuracy of the algorithm under low concentrations of aerosols in all three modes (1900 #/cm^3). For the urban and freeway aerosol, the number concentration of the ultrafine mode was high (1.9×10^6 #/cm^3), the surface area concentrations of the ultrafine mode (2.0×10^9 μm^2/m^3) and fine mode (1.1×10^9 μm^2/m^3) were similar, and the mass concentrations of the fine mode (38 μg/m^3) and coarse mode (43 μg/m^3) were also similar. For the coal power plant aerosol, the surface area concentration of the fine mode (5.1×10^8 μm^2/m^3) was much higher than that of the ultrafine mode (4.3×10^7 μm^2/m^3) and the coarse mode (4.0×10^7 μm^2/m^3). For the marine surface aerosol, the number concentration was only 440 #/cm^3; however, the mass concentration was over 12 μg/cm^3.

For each aerosol, we converted the nine parameters (one *CMD* x three modes + one *GSD* x three modes + one *N* x three modes = nine parameters) provided by Whitby and Sverdrup (1980) to obtain the 12 equivalent values that would be measured with the PACS (six $N_{obs,k}$, and six $M_{obs,k}$) assuming standard density (1000 kg/m^3) and spheres (shape factor = 1).

We evaluated the influence of the grid-search step size on the accuracy and precision of the fit for the four aerosols. For CMD_i, the step size was changed from 0.1×10^i nm to 0.5×10^i nm for each mode *i* with an increment of 0.05×10^i nm. For example, the step size was changed from 1 nm to 5 nm for ultrafine mode (*i*=1) with an increment of 0.5 nm, from 10 nm to 50 nm for fine mode (*i*=2) with an increment of 5 nm, and from 100 nm to 500 nm for coarse mode (*i*=3) with an increment of 50 nm. We calculated three statistical parameters: the normalized mean bias (*NMB*), normalized mean error (*NME*) and the R-squared (R^2) values as follows:

$$NMB = \frac{\sum(fit_j - real_j)}{\sum real_j} \times 100\% \quad (3\text{-}15)$$

$$NME = \frac{\sum|fit_j - real_j|}{\sum real_j} \times 100\% \quad (3\text{-}16)$$

$$R^2 = 1 - \frac{\sum(real_j - fit_j)^2}{\sum(real_j - \frac{1}{j}\sum real_j)^2} \quad (3\text{-}17)$$

where fit and $real$ are the fitting and real aerosol size distribution, respectively, for each size bin, j. In this study, we used 40 size bins for each decade of data (e.g., 40 bins from 10 nm to 100 nm).

NMB indicates the tendency of the algorithm to over-predict or under-predict variables, although the summing of positive and negative biases can lead to cancellation of an absolute magnitude of discrepancies. We also calculated *NME*, the sum of the absolute values of *NMB* at each size bin, to provide another indicator without the cancellation problem. In addition, R^2 was used to indicate how well the fitted tri-modal log-normal distribution approximates the real data points. We used the mean of each statistical parameter (*NMBs*, *NMEs* and R^2*s*) for the four aerosols tested to represent the accuracy, and the standard deviation (*SD*) of each parameter to represent the precision.

According to the above testing results, we selected the step size with the most accurate and precise fit. However, the computation time would dramatically increase due to the increase of grid-search times of CMD_i with decreased step size. In order to decrease the computation time, we established narrowed grid-search ranges for GSD_i and CMD_i with each decrease in the step size of CMD_i.

We then evaluated the refined algorithm for the four typical atmospheric aerosols by comparing the fitting results to the observed ones as follows: (1) we compared the aerosol size distributions in three metrics, (2) we compared the nine parameters given by Whitby and Sverdrup (1980), and (3) we calculated the statistical parameters (*NMB*, *NME* and R^2) in three metrics.

Sensitivity Analysis

We performed a sensitivity analysis to test the robustness of the algorithm in the presence of uncertainties from unknown particle density and shape factor. The sensitivity study was conducted by changing the particle density from 500 to 3000 kg/m^3 with a step

of 100 kg/m^3, and the shape factor from 1 to 3 with a step of 0.1. Therefore, 546 combinations (26 densities × 21 shape factors) of density and shape factor were selected to cover a wide range of aerosol types found in different environments. For example, the density of diesel fume ranges from 500 to 1200 kg/m^3 (Park et al., 2004). The density of welding fumes is over 3000 kg/m^3 (Kim et al., 2009). The shape factor of salt aerosol is 1.08 (near spherical), whereas that for welding fume can reach over 3 (Kim et al., 2009). For each combination of density and shape factor, we followed the same procedure described in Section 2.2 by using the four aerosols, then calculated the statistical parameters (*NMB*, *NME* and R^2) in three metrics.

Results and Discussion

Algorithm Refinement

The effect of reducing the grid-search step size of CMD_i on algorithm accuracy and precision is shown in Figure 3-2. In general, decreasing the step size of CMD_i improved accuracy and precision of the fitting results. Independent of step size, most mean *NMBs* were near zero (within ±3.6%), except surface area concentration (Figure 3-2a). The mean and *SD* of *NMBs* for surface area concentrations oscillated with decreasing step size becoming stable for the smallest step size. The surface area concentration was underestimated for the coarsest step size (*NMB* of -4.3% ± 11.7%), although it was near zero (1.8% ± 2.7%) for the smallest step size. The mean and *SD* of *NMEs* decreased substantially with decreasing step size (Figure 3-2b). For number concentrations, *NMEs* decreased from 26.8% ± 14.7% for a step size of 0.5×10^i nm to 9.7% ± 4.0% for a step size of 0.1×10^i nm (Figure 3-2b). For mass concentration, *NME* reached the highest value of 39.1% ± 43.3% for a step size of 0.5×10^i nm and then decreased to 8.0% ± 4.3% for a

step size of 0.1×10^i nm. For all metrics, the mean of R^2 approached one (0.97 for *N*, 0.94 for *SA*, and 0.98 for *M*), and the *SD* of R^2*s* reached was near zero (0.04 for *N*, 0.07 for *SA*, and 0.02 for *M*) for the smallest step size of 0.1×10^i nm (Figure 3-2c). For number concentration, R^2 increased from 0.91 ± 0.08 for a step size of 0.5×10^i nm to 0.97 ± 0.04 for a step size of 0.1×10^i nm. For surface area and mass concentrations, decreasing the step size from 0.5×10^i to 0.1×10^i nm increased the R^2 from 0.89 ± 0.16 to 0.94 ± 0.07, and from 0.44 ± 1.09 to 0.98 ± 0.02, respectively.

We selected 0.1×10^i nm as the final step size in the algorithm for several reasons. For each of the three statistical parameters, we found the most accurate and precise estimates at the step size of 0.1×10^i nm. The results of *NMB* indicated that the smallest step size resulted in the most accurate (with 0.8% of mean of *NMBs*) and precise (with 1.4% of SD of *NMBs*) fit for all three metrics. Similar to *NMB*, the *NME* results also indicated that the smallest step size resulted in the most accurate (with 9.3% of mean of *NMEs*) and precise (with 4.6% of SD of *NMEs*) fit for all three metrics. For R^2, the smallest step size resulted in the most accurate (with 0.96 of mean of R^2) and precise (with 0.04 of SD of R^2) fit for all three metrics as well. The oscillations of fitting results using various step sizes might be caused by the value of the last two significant figures of observed CMD_i. If the observed value of CMD_i could be located during grid-search, the fitting results would be accurate. The smaller the step size in the algorithm, the better chance he algorithm has of finding the observed value. However, using a computer with a processor of i7-4790 CPU (3.60 GHz) and installed memory of 8.00 GB, the computation time increased from 1.7 ± 1.0 sec for a step size of 0.5×10^i nm to 43.3 ± 29.0 min for a step size of 0.1×10^i nm.

We refined the algorithm using an adaptive process to decrease the computation time while still using the smallest step size for CMD_i (0.1×10^i nm). Further investigation of the above test results indicated that, regardless of CMD_i step size, fitted GSD_i were within ± 0.2 and fitted CMD_i were within $\pm 0.5 \times 10^i$ nm of true values. Thus, the grid-search ranges can be narrowed for each pass through Step 2 of the algorithm to minimize search times without sacrificing accuracy. We grid-searched GSD_i within the range of ± 0.2 constrained to the best values of GSD_i obtained from Step 1, which applied the whole range of GSD_i. Similarly, we grid-searched CMD_i within aerosol diameter ranges of $\pm 0.5 \times 10^i$ nm constrained around the best values of CMD_i obtained from Step 1. The step size of CMD_i was decreased from 0.5×10^i nm to 0.3×10^i nm, and then to 0.1×10^i nm with narrowed ranges of GSD_i and CMD_i to refine the algorithm. The computation time decreased from 43.3 ± 29.0 min to 24.3 ± 11.4 s after the refinement.

The results of fitting aerosol size distributions using the refined algorithm are shown in Figure 3-3 and summarized in Table 3-1. Overall, the fitted and observed aerosol size distributions in three metrics (number, surface area and mass concentrations) were in close agreement for all four pre-defined aerosols. For the ultrafine and fine modes, the algorithm found almost the exact values of the CMD_i, GSD_i and N_i for all four aerosols. The largest discrepancies between fit and observed values occurred for the fine and coarse mode of mass concentration for coal power plant aerosol (Figure 3-3c). The fitted distribution was shifted to larger sizes for both fine and coarse mode. For the surface area concentration of coal power plant aerosol, the algorithm underestimated the fine and coarse modes (Figure 3-3c). For the coarse mode, the CMD_3 was overestimated, and GSD_3 was underestimated to compensate for the overestimation of the aerosol size (CMD_3).

Table 3-2 summarizes the performance statistics of the refined algorithm for the four pre-defined aerosols. The estimated number and mass concentrations were more accurate than the surface area concentrations. For all four aerosols, *NMBs* for both number and mass concentrations were within ± 0.2%. The estimations of surface area concentrations were not as good as number and mass concentrations. According to the *NME* and R^2 values, the number aerosol size distribution was the most accurate among the three metrics. The percentage bias between fitted and observed size distributions for number and mass concentrations meet the acceptable criteria from both the EPA and NIOSH (within ± 10%).

Sensitivity Analysis

The results of the sensitivity study are depicted in Figure 3-4. For all parameters (NMB_i, NME_i, R^2), the fitting of surface area concentrations was more sensitive to unknown density and shape factor than number and mass concentrations. The *NMBs* of number and mass concentrations were ± 10%, whereas those for surface area concentrations deviated substantially above zero (underestimation of concentration) for particle density less than 1000 kg/m^3, and below zero (overestimation of concentration) for particle density larger than 1000 kg/m^3. In addition, by increasing the shape factor, the algorithm tended to underestimate the surface area concentration (Figure 3-4a).

NME and R^2 plots are shown in Figure 3-4b and 3-4c, respectively. For all metrics, aerosol size distributions fit well (low *NME* and high R^2 values) if the density and shape factor increased simultaneously. For aerosol number size distributions, the algorithm was most accurate (*NMEs* of 36.2% ± 22.8% coupled with R^2*s* of 0.80 ± 0.25) for the urban and freeway aerosol, followed by the marine surface aerosol (*NMEs* of 45.0% ± 34.4% and R^2*s*

of 0.67 ± 0.58), coal power plant aerosol (*NMEs* of 47.1% ± 29.5% and R^2*s* of 0.68 ± 0.48) and background aerosol (*NMEs* of 61.2% ± 23.3% and R^2*s* of 0.35 ± 0.45). For aerosol surface area size distributions, the algorithm was most accurate for the urban and freeway aerosol, which had the *NMEs* of 74.7% ± 31.4% and R^2*s* of 0.12 ± 0.68. For aerosol mass size distributions, the algorithm was the most accurate for the marine surface aerosol (*NMEs* of 26.5% ± 14.0% and R^2*s* of 0.90 ± 0.12). In the marine surface aerosol, both surface area and mass concentrations were dominated by coarse mode.

Independent of particle density and shape factor, fitted number and mass concentrations were within ± 10% of known concentrations, which meet the acceptable EPA and NIOSH criteria (see number and mass concentration plots in Figure 3-4a, in which, the light green color indicates the bias of approximately 0%). Compared to the number and mass concentrations, the fitted surface area concentrations were more sensitive to changes in particle density and shape factor. Moreover, the aerosol size distributions in all three metrics were fitted relatively well if the density and shape factor increased simultaneously. Density and shape factor are sometimes difficult to estimate. However, the PACS is able to collect particles on impactor plates in impactor stages, and meshes in diffusion stages. Then, we can obtain density and shape factor from analysis of collected materials.

Based on the PACS hardware, we developed a MMLN fitting algorithm to estimate aerosol size distributions in three metrics (number, surface area and mass concentration) over a wide size range (from 10 nm to 10 μm). The PACS is able to obtain a size distribution in 3 min. The results showed that the fitted and observed aerosol size distributions in three metrics (number, surface area and mass concentrations) were in close

agreement. The sensitivity studies indicated that the particle density and shape factor were of great importance to the fitting accuracy of the algorithm. Since the PACS is able to collect particles for later physical and chemical analysis in the laboratory, we could still correct the final results of aerosol size distributions after analyzing the physical and chemical properties of collected aerosols. Thus, the PACS sampler will directly benefit assessment of exposures to all size particles for workers in different environments, where the adverse health effects may be caused by different metrics.

Table 3-1: Parameters to describe three modes of aerosols found in diverse environments (obs.) compared to those determined by the PACS fitting algorithm (fit.), assuming standard density spheres.

Aerosol Type	Parameters	Ultrafine Mode		Fine Mode		Coarse Mode		All Modes	
		Obs.[1]	Fit.	Obs.[1]	Fit.	Obs.[1]	Fit.	Obs.[1]	Fit.
1. Clean background	*CMD (μm)*	0.015	0.017	0.067	0.076	0.929	0.900	--	--
	SMD (μm)	0.024	0.034	0.202	0.210	3.222	3.259	--	--
	MMD (μm)	0.030	0.050	0.350	0.349	6.000	6.198	--	--
	GSD	1.6	1.8	2.1	2.0	2.2	2.2	--	--
	N (#/cm^3)	1.1×10^{3}	1.3×10^{3}	8.0×10^{2}	6.5×10^{2}	7.3×10^{-1}	9.1×10^{-1}	1.9×10^{3}	1.9×10^{3}
	SA (μm^2/m^3)	1.3×10^{6}	2.3×10^{6}	3.4×10^{7}	3.3×10^{7}	6.8×10^{6}	8.4×10^{6}	4.2×10^{7}	4.3×10^{7}
	M (μg/m^3)	6.0×10^{-3}	1.6×10^{-2}	1.5×10^{0}	1.5×10^{0}	5.3×10^{0}	5.0×10^{0}	6.5×10^{0}	6.5×10^{0}
2. Urban and freeway	*CMD (μm)*	0.014	0.014	0.059	0.050	1.151	0.760	--	--
	SMD (μm)	0.024	0.023	0.155	0.150	3.460	2.873	--	--
	MMD (μm)	0.032	0.029	0.250	0.261	6.000	5.585	--	--
	GSD	1.7	1.7	2.0	2.1	2.1	2.3	--	--
	N (#/cm^3)	1.9×10^{6}	1.9×10^{6}	4.0×10^{4}	4.8×10^{4}	4.5×10^{0}	1.3×10^{1}	1.9×10^{6}	1.9×10^{6}
	SA (μm^2/m^3)	2.0×10^{9}	1.9×10^{9}	1.1×10^{9}	1.1×10^{9}	5.6×10^{7}	8.9×10^{7}	3.3×10^{9}	3.2×10^{9}
	M (μg/m^3)	9.2×10^{0}	8.5×10^{0}	3.8×10^{1}	3.7×10^{1}	4.3×10^{1}	4.4×10^{1}	9.0×10^{1}	9.0×10^{1}
3. Coal power plant	*CMD (μm)*	0.009	0.010	0.043	0.040	0.443	1.250	--	--
	SMD (μm)	0.013	0.013	0.111	0.139	2.375	3.922	--	--
	MMD (μm)	0.015	0.014	0.180	0.258	5.500	6.947	--	--
	GSD	1.5	1.4	2.0	2.2	2.5	2.1	--	--
	N (#/cm^3)	1.2×10^{5}	1.2×10^{5}	3.4×10^{4}	2.8×10^{4}	1.2×10^{1}	1.7×10^{1}	1.5×10^{5}	1.5×10^{5}
	SA (μm^2/m^3)	4.3×10^{7}	4.9×10^{7}	5.1×10^{8}	5.0×10^{8}	4.0×10^{7}	2.6×10^{7}	6.0×10^{8}	5.7×10^{8}
	M (μg/m^3)	1.0×10^{-1}	1.1×10^{-1}	1.2×10^{1}	1.6×10^{1}	2.4×10^{1}	2.1×10^{1}	3.6×10^{1}	3.6×10^{1}
4. Marine surface	*CMD (μm)*	0.010	0.010	0.071	0.084	0.622	0.660	--	--
	SMD (μm)	0.015	0.020	0.186	0.177	4.474	4.346	--	--
	MMD (μm)	0.019	0.029	0.300	0.256	12.000	11.153	--	--
	GSD	1.6	1.8	2.0	1.8	2.7	2.6	--	--
	N (#/cm^3)	3.8×10^{2}	3.9×10^{2}	6.1×10^{1}	5.0×10^{1}	1.1×10^{0}	1.1×10^{0}	4.4×10^{2}	4.4×10^{2}
	SA (μm^2/m^3)	1.8×10^{5}	2.5×10^{5}	2.5×10^{6}	2.4×10^{6}	9.8×10^{6}	1.0×10^{7}	1.2×10^{7}	1.3×10^{7}
	M (μg/m^3)	5.0×10^{-4}	1.0×10^{-3}	1.0×10^{-1}	8.4×10^{-2}	1.2×10^{1}	1.2×10^{1}	1.2×10^{1}	1.2×10^{1}

[1] Whitby and Sverdrup (1980)

Table 3-2: Summary of fitting results for aerosols found in diverse environments, assuming standard density spheres.

Aerosol Type	NMB, %			NME, %			R^2		
	N	*SA*	*M*	*N*	*SA*	*M*	*N*	*SA*	*M*
1. Clean background	0.0	3.5	0.0	11.9	6.2	3.3	0.98	1.00	1.00
2. Urban and freeway	0.0	-3.2	0.0	5.3	7.9	9.4	1.00	0.99	0.99
3. Coal power plant	0.0	-4.9	0.0	27.6	24.0	23.2	0.90	0.94	0.90
4. Marine surface	0.0	2.5	-2.7	17.5	6.2	5.9	0.97	0.99	1.00

NMB: normalized mean bias; *NME*: normalized mean error; *N*: number concentration; *SA*: surface area concentration; *M*: mass concentration

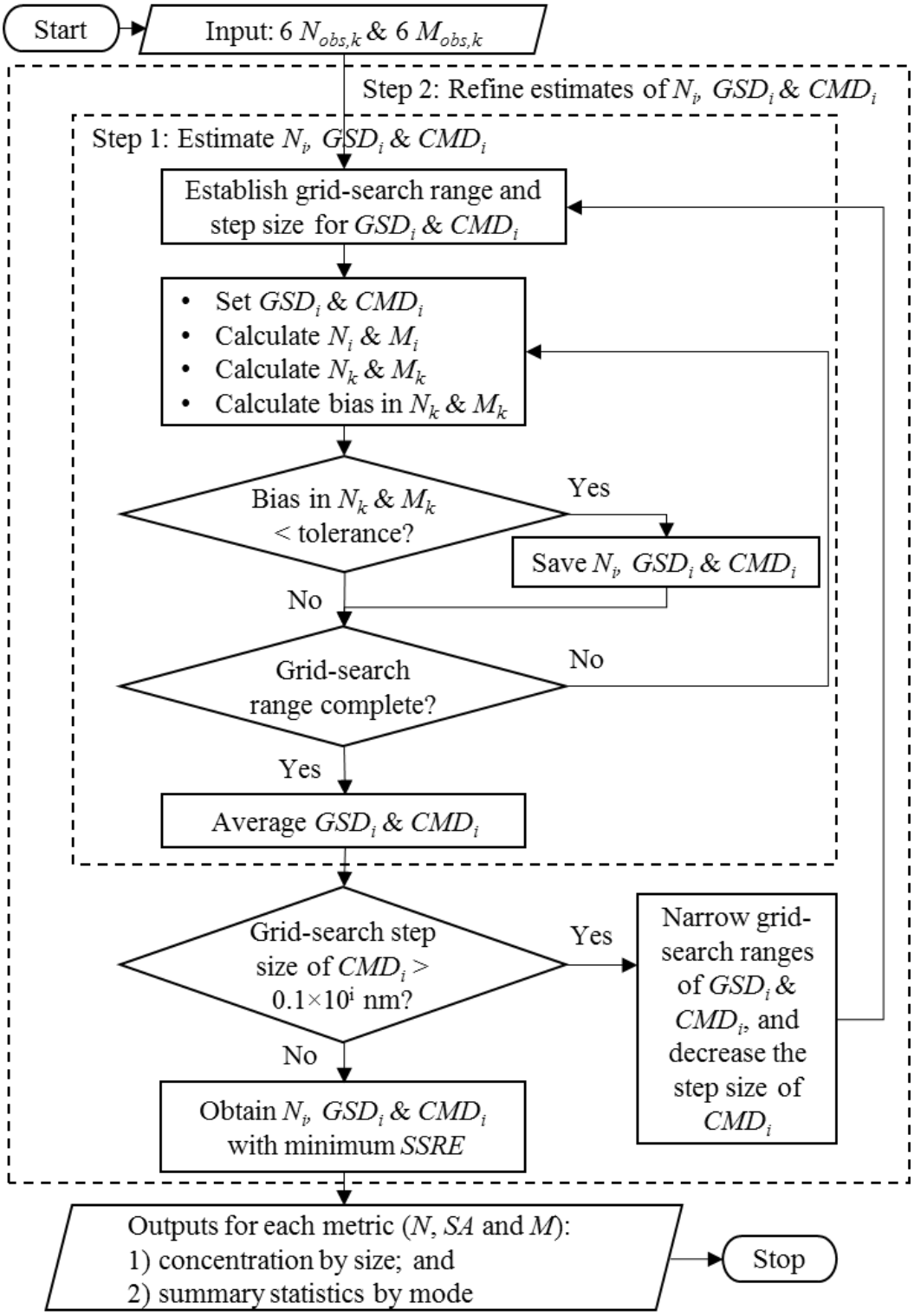

Figure 3-1: Flow chart of the fitting algorithm developed for the PACS.

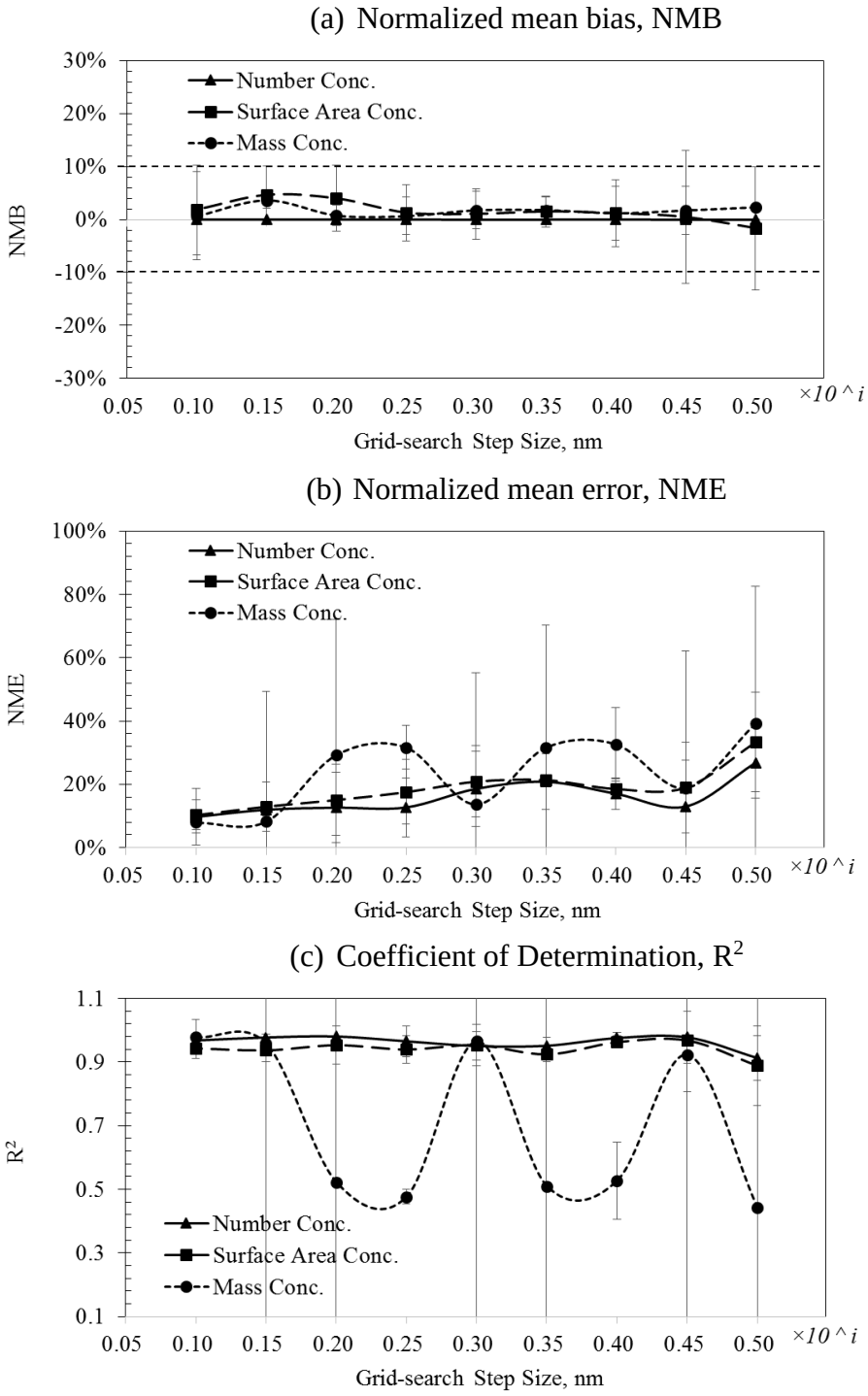

Figure 3-2: Effect of the grid-search step size on the fitting results expressed as: (a) *NMB*; (b) *NME*; and (c) R^2. The step size ranged from 1 nm to 5 nm for ultrafine mode, from 10 nm to 50 nm for fine mode, and from 100 nm to 500 nm for coarse mode. Error bars represent one standard deviation.

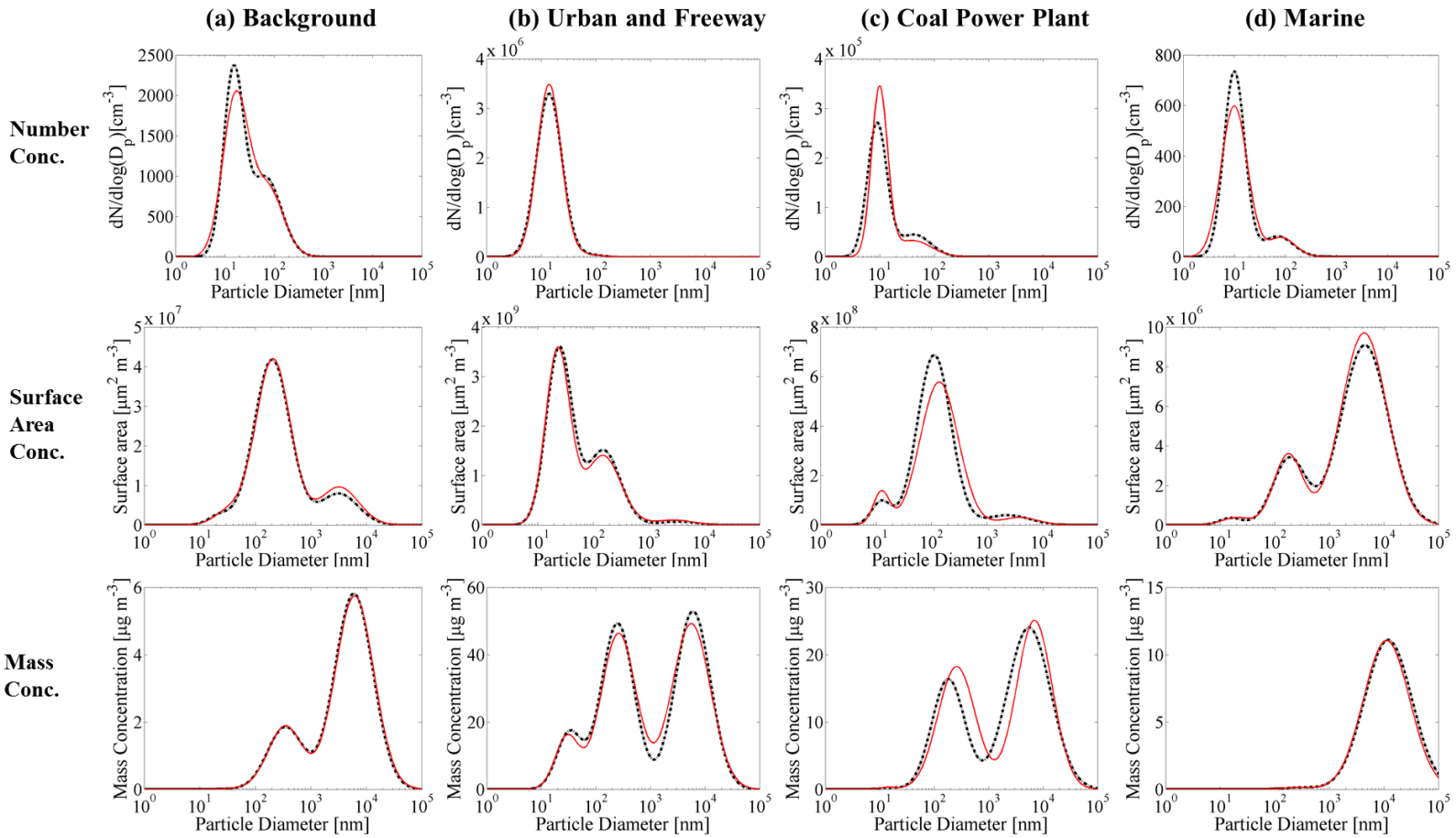

Figure 3-3: Particle size distributions estimated with the PACS fitting algorithm for four atmospheric aerosols: (a) clean continental background; (b) urban and freeway; (c) coal power plant; and (d) marine surface. The black, dotted lines represent the pre-defined aerosol, and the red, solid lines represent the distribution fit with the algorithm.

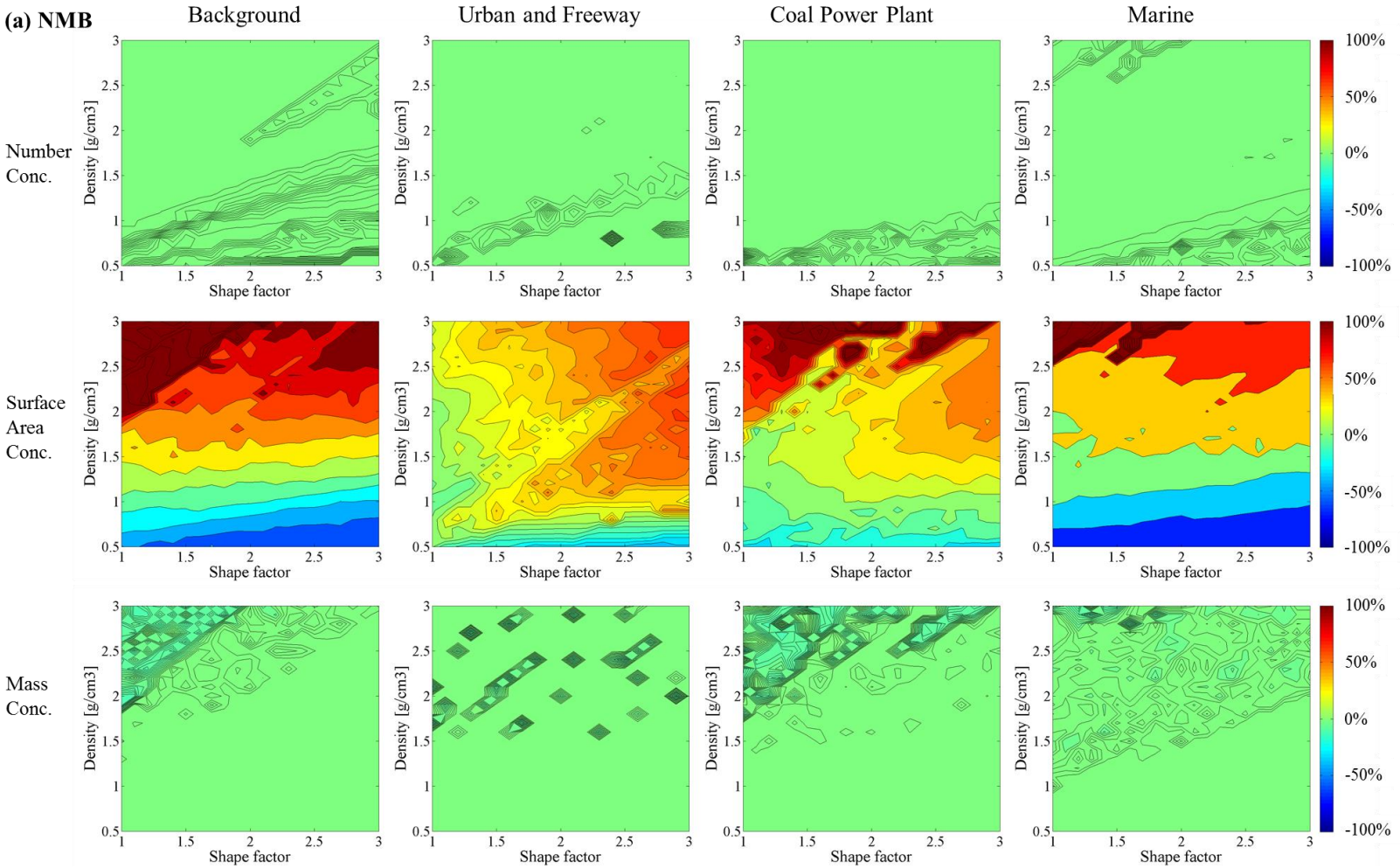
(a) NMB
Background
Urban and Freeway
Coal Power Plant
Marine
Number Conc.
Surface Area Conc.
Mass Conc.
Density [g/cm3]
Shape factor
100%
50%
0%
-50%
-100%

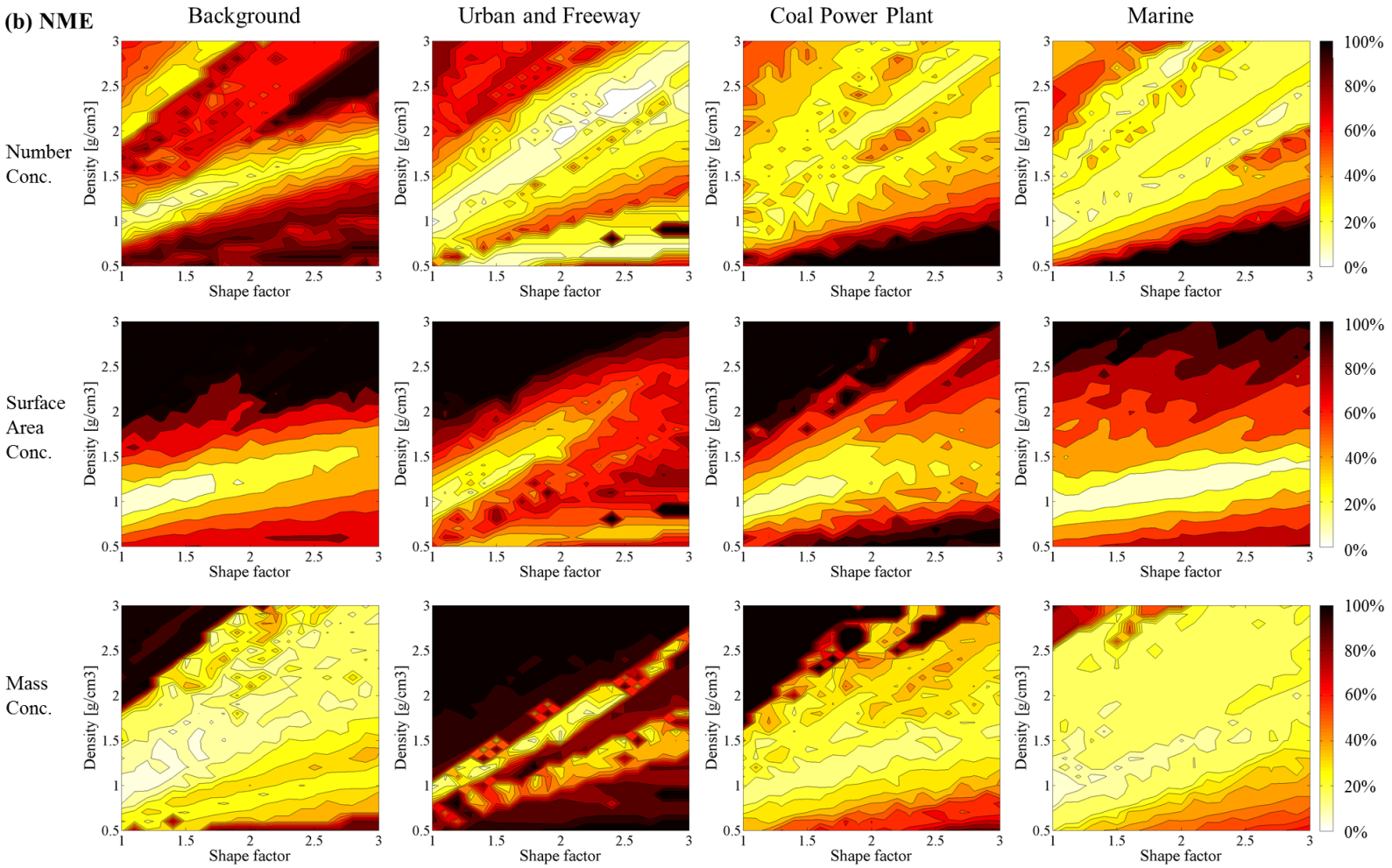
(b) NME
Background
Urban and Freeway
Coal Power Plant
Marine
Number Conc.
Surface Area Conc.
Mass Conc.
Density [g/cm3]
Shape factor
0.5
1
1.5
2
2.5
3
100%
80%
60%
40%
20%
0%

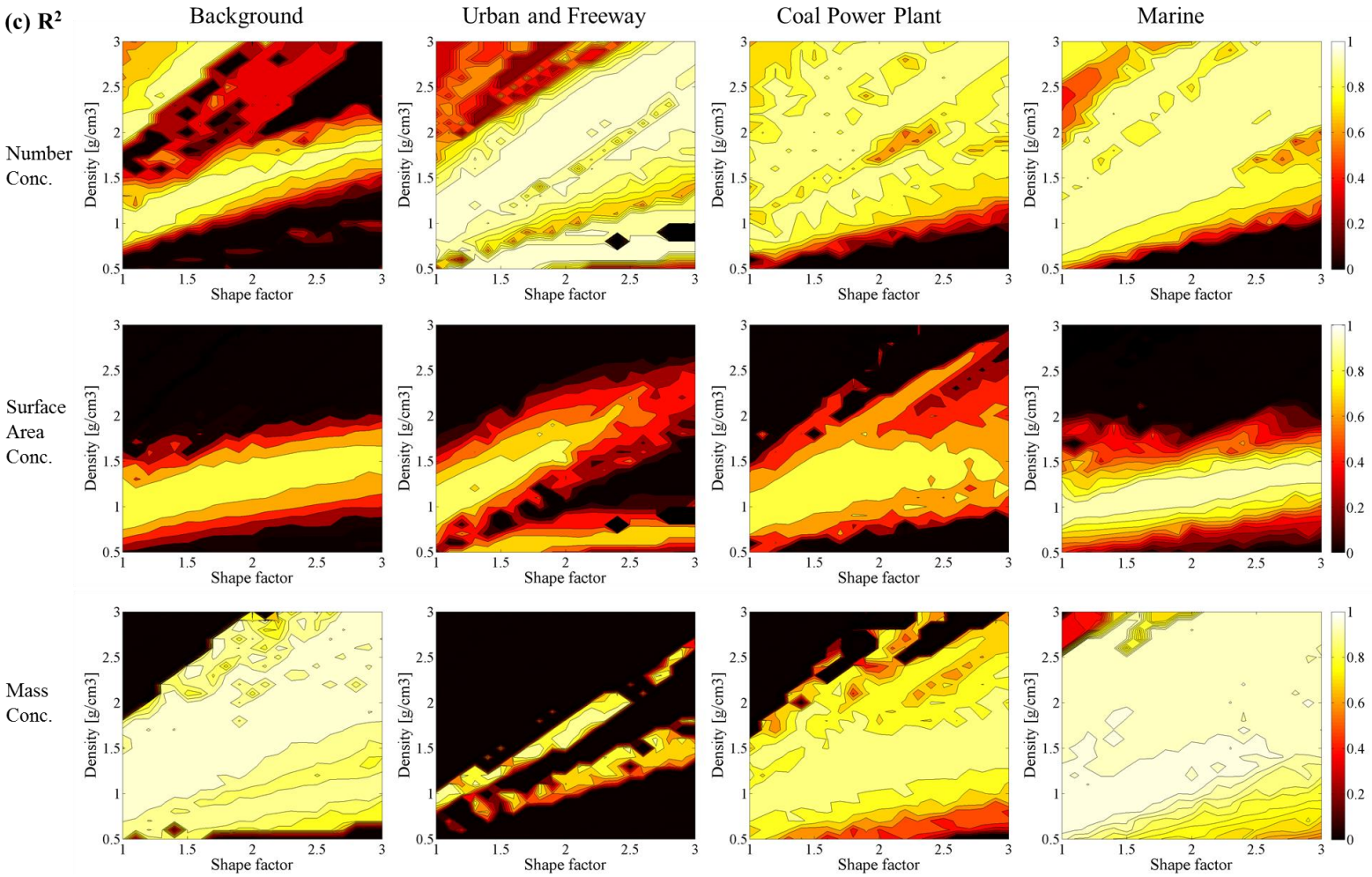

Figure 3-4: Effects of changing the particle density and shape factor on the algorithm fitting results expressed as: (a) *NMB*; (b) *NME*; and (c) R^2.

CHAPTER IV

EVALUATION OF A PORTABLE AEROSOL COLLECTOR AND SPECTROMETER (PACS) TO MEASURE PARTICLE CONCENTRATIONS AND COMPOSITION BY SIZE

Abstract

We developed an algorithm to estimate mass concentration by size and composition with a Portable Aerosol Collector and Spectrometer (PACS). In laboratory experiments, we compared particle size distributions measured with the PACS to reference instruments for multi-modal aerosols: two-mode generated by spark discharge, consisting of ultrafine (fresh Mn fume) and fine particles (aged Cu fume); and three-mode produced by adding coarse particles (Arizona road dust) to that generated by spark discharge. Near-real-time size distributions from the PACS compared favorably to those from a scanning mobility particle sizer and an aerodynamic particle sizer for the three-mode aerosol (number, *bias* = 9.4% and R^2 = 0.96; surface area, *bias* = 17.8%, R^2 = 0.77; mass, *bias* = -2.2%, R^2 = 0.94), but less so for the two-mode aerosol (number, *bias* = -17.7% and R^2 = 0.51; surface area, *bias* = -45.5%, R^2 = 0; for mass, *bias* = -81.75%, R^2 = 0.08). Estimates of elemental mass concentration by size were similar to those measured with a nano micro-orifice uniform deposition impactor for coarse-mode particles, whereas agreement was considerably poorer for ultrafine- and fine-mode particles. The PACS has merit in estimating multi-metric concentrations by size and composition but requires further research to resolve discrepancies identified for two-mode aerosol.

Introduction

Adverse health effects from the inhalation of aerosols are a complicated function of aerosol size, composition, and concentration (Harrison and Yin, 2000). Particles deposit in different regions of the respiratory system according to their size and shape (Hinds, 1999), whereas the adverse health effects potentially resulting from these deposited particles depend on particle composition (Valavanidis et al., 2008). Moreover, three concentration metrics (number, surface area and mass) are considered as predictors of various adverse health effects for different size particles (Kittelson, 1998; Brouwer et al., 2004; Ramachandran, 2005; Ellenbecker and Tsai, 2015).

A combination of commercially available research instruments are needed to assess aerosol exposures by size, composition, and multiple concentration metrics. Some instruments provide a way to continuously measure aerosol number concentrations by size, such as the scanning mobility particle sizer (SMPS, ~$70,000) for measuring the sub-micrometer particles by equivalent mobility particle size, and the aerodynamic particle sizer (APS, ~$50,000) for measuring particles larger than ~0.7 μm by aerodynamic particle size (Baron, 1986; Wang and Flagan, 1990). Surface area and mass size distributions can be estimated reasonably well with the SMPS and APS because the number concentrations are highly resolved by size. Such estimates, however, are improved with knowledge of particle density and shape factor, which is not available from these instruments. Other devices, such as the nano micro-orifice uniform deposit impactor (nanoMOUDI, ~$60,000) (Marple et al., 1986, 1991; Maenhaut et al., 1996), provide a way to collect particles by aerodynamic particle size for subsequent chemical analyses, such as inductively coupled plasma-mass spectrometry (ICP-MS) (Karthikeyan et al., 2006; Kulkarni et al., 2007).

Combined, the SMPS, APS, and nanoMOUDI provide near-real-time size distributions by metric and composition. However, they are expensive (>$60,000), large, and heavy, limiting their use to research studies.

Previously, we introduced a new device—the Portable Aerosol Collector and Spectrometer (PACS)—designed to estimate aerosol size distributions of three metrics (number, surface area and mass concentration) in near-real-time (<3 min), and to collect particles to determine mass concentration by size and composition. Introduced in Chapter II, the PACS hardware consists of a six-stage particle size selector, a valve system, a water condensation particle counter (WCPC) to detect number concentrations, and a photometer to detect mass concentrations. The valve system diverts airflow to pass sequentially through each stage of the selector to the detectors. The first stage of the selector allows aerosol entering the inlet to freely pass through to the valve manifold. The next three impactor stages collect particles by single-hole impactors with measured 50% stage cut-off diameters, d_{50}s, of 10 µm, 1 µm, and 0.4 µm of aerodynamic diameter. The last two stages collect particles by diffusion with measured d_{50}s of 16 nm and 56 nm of geometric diameter, respectively. A software program sequentially opens one valve at a time to obtain six number and six mass concentrations every 3 min. In Chapter III, we developed a multi-modal log-normal (MMLN) fitting algorithm that leverages these low-resolution, two-metric measurements to estimate number, surface area, and mass concentration highly resolved by size from 10 nm to 10 µm in near-real-time.

In this study, we had two objectives: (1) to develop an algorithm to estimate the mass distribution of an aerosol by size and composition using data from the chemical analysis of particles collected on the stages of the PACS size selector; and (2) to compare

particle size distributions measured for multi-modal aerosols with the PACS to those measured with reference instruments in the laboratory. We compared the near-real-time number, surface area and mass concentrations by size measured with the PACS to those measured with the SMPS/APS and mass concentrations by size and composition measured with the PACS to those measured with the nanoMOUDI.

Methods

Description of the Algorithm

We developed a new algorithm—the mass distribution by composition and size (MDCS) algorithm—to estimate mass concentration by size and chemical component from analysis of particles collected on the stages of the PACS size separator (Figure 4-1). The algorithm has three inputs: (1) the mass of each element *e* from analysis (in this work, chemical analysis by ICP-MS) of particles collected in each PACS stage *k*, $m_{e,k,ICP-MS}$; (2) the collection efficiency of particles by size d_p for each PACS stage, $C_k(d_p)$ (experimentally determined in Chapter II; equivalent mobility diameter for particles smaller than ~700 nm and aerodynamic diameter for particles larger than ~700 nm); (3) output from the MMLN algorithm (introduced in Chapter III) including, for each particle size mode *i*, the mass concentration by size $\left(M_i(d_p)\right)$, the mass median diameter(MMD_i), and geometric standard deviation (GSD_i). We used a tri-modal, log-normal distribution to mathematically express the mass size distribution of a particle for a given composition (Whitby, 1978):

$$f(d_p, M_i, MMD_i, GSD_i) = \sum_{i=1}^{3} \frac{M_i}{\sqrt{2\pi}\ln(GSD_i)} \exp\left[-\frac{\left[ln(d_p)-ln(MMD_i)\right]^2}{2ln^2(GSD_i)}\right] \quad (4\text{-}1)$$

For each element, we adjust $m_{e,k,ICP-MS}$ (Input 1) for the fact that lower volumes of air pass through each successive stage as follows:

$$m_{e,k} = m_{e,k,ICP-MS} \times \frac{t_{total}}{t_k} \quad (4\text{-}2)$$

where t_{total} is the total time of one PACS measurement cycle, and t_k is the time that air passes through a given stage during that sequence. The air volume sampled differs because the stages are in series and the valves open sequentially one at a time. For one cycle given the current arrangement of the PACS with each valve open for 30 sec, the total time is 180 sec and the time that air passes through Stage 1 is 150 sec, Stage 2 is 120 sec, Stage 3 is 90 sec, Stage 4 is 60 sec, and Stage 5 is 30 sec. Using $m_{e,k,ICP-MS}$ values that are greater than the limit of detection (LOD), we assign the element to a mode(s) as follows: (1) all modes, if mass detected in impactor and diffusion stages; (2) fine and coarse modes, if mass in all three impactor stages only; (3) coarse mode, if mass in the first two impactor stages only; (4) ultrafine and fine modes, if mass in diffusion stages only; and (5) ultrafine mode, if mass in first diffusion stage only.

We multiply $C_k(d_p)$ from Input 2 by $M_i(d_p)$ from Input 3 to calculate the mass concentration of each mode in each stage by size:

$$M_{i,k}(d_p) = M_i(d_p) \times C_k(d_p) \quad (4\text{-}3)$$

Assuming that the mode structure is the same as the mode structure identified by the MMLN algorithm, we calculate the mass fraction of each mode among all three modes in each stage as:

$$F_{i,k,e} = \frac{\int_0^\infty \sum_i M_{i,k}(d_p) d(d_p)}{\int_0^\infty \sum_{i=1}^3 M_{i,k}(d_p) d(d_p)} \quad (4\text{-}4)$$

We also calculate the mass fraction of each stage among all six stages of each mode as:

$$F_{k,i,e} = \frac{\int_0^\infty \sum_k M_{i,k}(d_p)d(d_p)}{\int_0^\infty \sum_{k=0}^5 M_{i,k}(d_p)d(d_p)} \quad (4\text{-}5)$$

We then calculate the mass concentration in each mode as:

$$M_{e,i} = \frac{m_{e,k} \times F_{i,k,e}}{F_{k,i,e}} \times \frac{1}{Q \times t} \quad (4\text{-}6)$$

where Q is the PACS flowrate, and t is the sampling time.

For each element, we obtain the *MMD* and *GSD* of each mode output by the MMLN algorithm. We then distribute the mass ($M_{e,i}$) calculated above. The algorithm outputs: (1) composition mass size distribution from 10 nm to 10 μm resolved in 40 size bins for each decade of data; (2) summary statistics (M_e, *MMD*, *GSD*) for each mode.

Experimental Setup and Aerosol Generation

We compared aerosol size distributions measured with the PACS to those measured with reference instruments two multi-modal aerosols: (1) a three-mode aerosol with fresh Mn fume for the ultrafine mode (<100 nm), aged Cu fume for the fine mode (100 nm ~ 1 μm) and Arizona road dust for the coarse mode (>1 μm), and (2) a two-mode aerosol with fresh Mn fume for the ultrafine mode and aged Cu fume for the fine mode. The three-mode aerosol was used to mimic the structure observed by Whitby and Sverdrup (1980) as typical of ambient aerosol, whereas the two-mode aerosol was used to evaluate the PACS under an extreme case (i.e., little mass concentration detected by the photometer without a coarse mode).

Following the aerosol generating procedures described by Park et al. (2014), fresh Mn fume (ultrafine mode aerosol) was produced with a spark discharge system with 5 kV voltage and 3 mA current applied between two identical pure Mn rods (3 mm diameter x 75 mm length, purity 99.5%, Goodfellow Corporation, PA, USA). To produce aged Cu fume (fine mode aerosol), we used a second spark discharge system operated with 5 kV voltage applied between two identical pure Cu rods (3 mm diameter x 75 mm length, alloy 101, purity 99.99%, McMaster-Carr Elmhurst, IL, USA). The aerosol produced with this system was aged as it was passed through two coagulation chambers in series (2 chambers × 200 L each = 400 L). The aerosols produced in the spark chambers were passed through Po-210 neutralizer. Coarse mode aerosol was produced by aerosolizing Arizona road dust (Fine Grade, Part # 1543094, Powder Technology Inc., Arden Hills, MN, USA) with a fluidized bed aerosol generator (3400A, TSI Inc., Shoreview, MN, USA).

Experiments were conducted in a test chamber (Figure 4-2). The chamber consisted of a mixing zone (0.64 m × 0.64 m × 0.66 m) and a sampling zone (0.53 m × 0.64 m × 0.66 m), divided by a perforated plate, which contains 600 evenly spaced holes (0.6 cm in diameter). Room air was filtered with two high efficiency particulate air filters to provide the clean air to the mixing zone. We fed the generated multi-modal aerosols directly into the mixing zone of the test chamber. For each aerosol type, we conducted three experiments, and each experiment lasted 8 hours.

Measurement instruments were positioned outside the sampling chamber including the PACS, SMPS (SMPS 3936, TSI Inc., Shoreview, MN, USA), APS (APS 3321, TSI Inc., Shoreview, MN, USA) and nanoMOUDI (model 125-R, MSP, Shoreview, MN, USA). The collection plates of the PACS impactor stages were operated with greased filters

to facilitate digestion by ICP-MS. Polycarbonate substrates (0.2 μm pore size, 47 mm diameter, Part # PCT0247100, Sterlitech Corporation, Kent, WA, USA) were cut in-house to 11-mm-diameter circles. A round stamp cut out of foam (37 mm in diameter) dipped into oil (Heavy-Duty Silicon Oil, Part # 07041, MSP Corporation, Shoreview, MN, USA) was pressed onto the middle of polycarbonate substrates to create a layer of silicone oil coating. Greased substrates were baked in the oven at 50ºC for 4 hours to evaporate volatile material and create a thin layer of sticky silicone intended to prevent particle bounce (Pak et al., 1992). The greased filter was attached to pre-oiled, porous plastic discs (9.5 mm in diameter, Part # 225-388, SKC Inc., Eighty Four, PA, USA) and pressed into a recess in the impactor plate assembly. Nylon meshes (41–μm net filters, Part # NY4104700, Carrigtwohill, Co. Cork, Ireland) held in place with a 47-mm filter holder were used to collect particles by Brownian motion in the diffusion stages. We used one mesh for the first diffusion stage, and six meshes for the second diffusion stage. The PACS was operated at 0.7 L min^{-1} for 8 hours of one experiment.

The SMPS measured particle number concentration by size (64 size bins per decade) from ~10 to ~400 nm (equivalent mobility diameters) every 3 minutes during the first hour of sampling. The APS measured particle number concentration by size (32 size bins per decade) from ~700 nm to ~20 μm (aerodynamic diameters) every 30 seconds during the first hour of sampling. The nanoMOUDI was operated at 10 L min^{-1} for 8 hours of one experiment, and 13 polycarbonate substrates (0.2 μm pore size, 47 mm in diameter, Part # PCT0247100, Sterlitech Corporation, Kent, WA, USA) coated with silicon oil, using the same procedure described above for preparing the PACS impactor substrates. A mixed cellulose esters filter (0.8 μm pore size, 47 mm in diameter, Part # FMCE847, Zefon

International, Inc., Ocala, FL, USA) was used as a backup filter in the last nanoMOUDI stage to collect remaining particles.

Near-real-time Aerosol Size Distributions

We applied the MMLN algorithm, presented in Chapter III, to convert number and mass concentrations measured by stage with PACS to number, surface area and mass concentration by size. These estimates were compared to those measured with the SMPS/APS. We obtained three SMPS measurements (time = 3 min × 3 times = 9 min) during the first sampling hour, and then calculated the average of them. For the same 9-min time period, we also calculated the average of all APS measurements. After measuring the number concentration by size using SMPS and APS, we converted the number concentration by size to surface area and mass concentration by size by assuming the standard density and spheres of the particles. We then compared the mean values measured from the PACS and SMPS/APS during the same 9-min sampling time. For each metric, we then quantified the ability of PACS to measure aerosol size distributions with the following two statistical parameters:

$$Percentage\ bias = \frac{\sum(PACS_j - Ref_j)}{\sum Ref_j} \times 100\% \quad (4\text{-}7)$$

$$R^2 = 1 - \frac{\sum(Ref_j - PACS_j)^2}{\sum(Ref_j - \frac{1}{j}\sum Ref_j)^2} \quad (4\text{-}8)$$

where $PACS_j$ and Ref_j are the measured aerosol concentration with the PACS and the reference instruments (SMPS/APS), respectively, for each size bin, j. In order to make the measurement results comparable between the PACS and SMPS/APS, we converted the

aerodynamic diameter measured with the PACS for particles smaller than ~700 nm to equivalent mobility diameter by assuming standard density spheres.

Percentage bias indicates the tendency of the PACS to overestimate or underestimate total concentration each metric. R^2 indicates how well the measured aerosol size distributions of number, surface area and mass concentration with the PACS approximates the data points measured with the SMPS/APS.

Mass Concentration by Element and Size

After sampling, the PACS substrates (three impactor plates and two sets of diffusion nylon meshes) and 14 nanoMOUDI substrates were each digested separately using a combination of 29 M HF and 15 M HNO_3 (HF:HNO_3 = 1:4) acids in 7-ml capsules (Perfluoroalkoxy vial, Savillex Corporation, MN, USA) on a hotplate at 95°C (Baker et al., 2004). After 24 hours of digestion, we opened the capsule lids, and set up the lids and capsules on a hotplate at 95°C. After 12 hours, HF and HNO_3 were evaporated from the samples. Then, we added 15 M HNO_3 into the capsules to dissolve the sample on a hotplate at 95°C. After 12 hours, we opened the capsule lids, and set up the lids and capsules on a hotplate at 95°C. After 12 hours of evaporation, we diluted the samples with water ultra-purified by Milli-Q system (Milli-Q, Millipore Corporation, MA, USA) to 2% HNO_3 solutions.

Samples were analyzed by ICP-MS (X Series II quadrupole, Thermo Fisher Scientific, MA, USA) for metals present in a Complete Standard Solution 71A (Al, As, B, Ba, Be, Cd, Ca, Cd, Ca, Ce, Cr, Co, Cu, Cs, Dy, Er, Eu, Gd, Ga, Ho, Fe, La, Pb, Lu, Mg, Mn, Nd, Ni, P, K, Pr, Rb, Sm, Se, Ag, Na, Sr, S, Tl, Th, Tm, U, V, Yb, Zn) and a Refractory

Elements Standard Solution 71B (Sb, Ge, Hf, Mo, Nb, Si, Ta, Te, Sn, Ti, W, Zr) using an Internal Standard Solution 71D (Bi, In, Sc, Tb, Y, Li). All solutions were National Institute of Standards and Technology (NIST) certified reference materials sold by Inorganic Ventures (Christiansburg, VA). Standard solutions were diluted with 2% HNO_3 (Trace Metal Grade, Fisher Scientific LLC, Pittsburgh, PA) to concentrations of 0, 10, 20, 30, 40, and 50 part per billion (ppb) to measure the calibration curve.

We compared the mass size distributions measured with the PACS to those measured with the nanoMOUDI for several particle compositions determined through ICP-MS chemical analysis. We ran the MMLN algorithm to obtain the needed inputs ($M_i(d_p)$, MMD_i and GSD_i) for the MDCS algorithm. Together with other inputs ($m_{e,k,ICP-MS}$ from ICP-MS and $C_k(d_p)$ from measurement), we then ran the MDCS algorithm to calculate the mass concentrations by size for each element. Mn was used as an indicator of the ultrafine mode, and Cu was used as an indicator of the fine mode. Fe is one of the main elements in the Arizona road dust, so we used the Fe as an indicator of the coarse mode (Ramadan et al., 2000).

Results and Discussion

Near-real-time Aerosol Size Distributions

The near-real-time number, surface area and mass concentrations by size measured with the PACS and SMPS/APS are summarized in Table 4-1 and presented graphically for the three-mode aerosol in Figure 4-3 and for the two-mode aerosol in Figure 4-4. In these figures, Panel a shows the raw concentration data from the PACS detectors (WCPC and

photometer) relative to time, and Panel b shows the size distribution results from the MMLN algorithm compared to that from the SMPS/APS.

As expected for the three-mode aerosol, the size selector in the PACS removed more particles with each stage added in a sequence of measurement, resulting in stair steps in the raw number and mass concentration (Figure 4-3a). The number concentration was more stable than the mass concentration because the metal fume generated by the spark discharging system was more stable than the Arizona road dust generated by the fluidized bed aerosol generator. Particle number, surface area and mass concentrations by size measured with the PACS were compared to those measured with the SMPS/APS (Figure 4-3b). The number concentration measured with the PACS was similar to that measured with the SMPS/APS (*percentage bias* for the total number concentration was 9.4%, coupled with R^2 of 0.96 shown in Table 4-1). The surface area concentration was overestimated with a *percentage bias* of 17.8% and R^2 of 0.77. The mass concentration measured with the PACS was 2.2% lower than that measured with the SMPS/APS with R^2 of 0.94.

For the two-mode aerosol, mass concentrations detected with the photometer were low (0.003 ± 0.001 mg/m^3) in all stages (Figure 4-4a) because of the limitations of photometer for measuring mass concentrations. The photometer uses the Mie theory of light scattering of particles and the built-in optical parameters (e.g., light wavelength and detection angle) (Görner et al., 1995). Therefore, the mass concentration measured with the photometer is a function of the main aerosol parameters including the refractive index, particle density, particle size, etc. For metal fume, Sousan et al. (2017) found that mass concentrations measured with a photometer were highly linear (correlation coefficient r =

0.99) with those measured gravimetrically, but severely underestimated (slope of 0.2 ± 0.01; photometer 5 times lower than gravimetric mass concentration). In addition, the lower detection limit of the photometer is 100 nm, so the photometer cannot measure the mass concentration of ultrafine mode particles.

The size distributions measured with the PACS compared poorly to those from the SMPS/APS (Figure 4-4b). For number concentration, the PACS underestimated the particle size of both ultrafine and fine modes. The inability to identify the ultrafine and fine modes resulted in underestimated total concentration and poor R^2 values for number (bias = -17.7%; R^2 = 0.51), surface area (bias = -45.5%; R^2 = 0) and mass concentration (bias = -81.8%; R^2 = 0.08) (Table 4-1). We attribute this poor agreement to the inability of the photometer to measure particles throughout the fine mode. If we apply the correction factor of 5 for the metal fume obtained from the study of Sousan et al. (2017), the size distributions measured with the PACS were greatly improved (Figure E-1 in Appendix E). The bias of the number concentration was increased from -17.7% to 31.8% with R^2 increased from 0.51 to 0.76. The bias of the surface area concentration was increased from -45.5% to 39.6% with R^2 increased from 0 to 0.25. The bias of the mass concentration was increased from -81.8% to -10.6% with R^2 increased from 0.08 to 0.77.

The PACS was able to fit aerosol size distributions for the three-mode aerosol substantially better than for the two-mode aerosol. As designed, reasonable size distributions for number, surface area, and mass were concentration were obtained with the MMLN fitting algorithm when raw measurement data was available in all stages (i.e., the three-mode aerosol, Figure 4-3). Thus, the PACS is able to successfully leverage the two-

metric, low-resolution data from handheld CPC and photometer technology to estimate size distributions with high resolution over a wide size range in near-real-time.

We envision several ways to improve the ability of the PACS to measure near-real-time aerosol size distributions. For both three- and two-mode aerosols generated in this study, very little mass was detected by the photometer in diffusion stages due to the inability of the photometer to detect metal fume (Figure 4-3a and 4-4a). The addition of a diffusion charger would provide a direct and highly sensitive way to measure ultrafine and fine particle surface area concentration of ultrafine and fine particles. However, adding a diffusion charger would increase the cost (~$15,000) and size of the device.

Adding a stage to the size selector may also help resolve the ultrafine and fine modes. Another impactor stage between impactor stage 2 (d_{50} of 400 nm) and 3 (d_{50} of 1 μm) may provide more information needed to better estimate the fine mode, whereas adding another diffusion stage after the diffusion stage with d_{50} of 56 nm may help with estimating both ultrafine and fine modes. However, adding stages would increase the measurement time, device size and device weight.

Mass Concentration by Element and Size

The results of experiments to evaluate the ability of the PACS to measure mass concentration by element and size are presented for the three-mode aerosol in Figure 4-5 and the two-mode aerosols in Figure 4-6. In these figures, Panel a shows the raw and time-adjusted mass of the three elements selected to represent different aerosol modes measured on each PACS stage by ICP-MS chemical analysis. Since the valve is open and closed one by one, the time adjusted masses are higher than the raw determined masses, especially in the diffusion stages. The raw data are used as input to the PACS MDCS algorithm, and

Panel b shows the mass size distribution output by the MDCS algorithm compared to that from the nanoMOUDI. The mass concentrations of the three elements measured with the PACS and the nanoMOUDI are summarized in Table 4-2.

For the three-mode aerosol, Fe, an indicator of coarse particles, was detected in impactor stages (Figure 4-5a) but not in diffusion stages. We expected this result because the measured *MMD* of Arizona road dust is ~3.3 μm of aerodynamic diameter (Figure 4-3b), which is consistent with the measurement from the study of Peters et al. (2006). The impactor stage with the d_{50} of 0.4 μm removed all dust particles. Also as expected based on SMPS/APS measurements (Figure 4-3b), the marker for fine-mode particles, Cu, was detected in both diffusion stages, and the marker for ultrafine particles, Mn, was detected in the first diffusion stage. However, we were surprised that Cu and Mn were found at appreciable levels on the impactor stages. We discuss this finding during the presentation of results for the two-mode aerosol.

The relative magnitudes of elements measured with the nanoMOUDI in the three modes shown in Figure 4-5b are consistent with the time-adjusted masses of elements in PACS stages shown in Figure 4-5a. For example, the Fe was only detected in impactor stages, so the coarse mode dominated the Fe mass concentration. Cu were mainly collected by the second diffusion stage, so the fine mode dominated the Cu mass concentration. Mn were determined in both impactor and diffusion stages, the Mn concentrations were found among all three modes. In addition, since the element masses estimated with the MDCS algorithm in the three modes were found in similar particle sizes compared to the d_{50s} of PACS stages, the mode selection process presented in the algorithm development was reasonable.

The PACS estimated the *MMDs* of the coarse mode well for all three elements, but overestimated the *MMDs* of the fine modes (Figure 4-5b). However, according to Table 4-2a, the Cu mass concentration in fine mode measured with the PACS (7.3 $\mu g/m^3$) was similar to that measured with the nanoMOUDI (6.0 $\mu g/m^3$). These results suggest that the *MMD* of the fine mode obtained from MMLN fitting results for the three-mode aerosol may not be applicable for each specific element. This finding is consistent with a previous study showing that particles of different composition usually have different modal structures (Bardouki et al., 2003). The PACS substantially underestimated the particles smaller than 10 nm. For the WCPC used in the PACS, the count efficiency of particles would rapidly decrease from ~100% to ~0% by decreasing the particle size from ~10 nm to ~4 nm (Hakala et al., 2013). This might be the reason why the ultrafine mode measured with the PACS is consistent with that measured with the SMPS (Figure 4-3b), but is severely underestimated by comparing to that measured with the nanoMOUDI (Figure 4-5b).

For the two-mode aerosol, Fe was negligible because Arizona road dust was not present (Figure 4-6a). As expected based on SMPS/APS measurements (Figure 4-4b), Cu was mostly detected on diffusion stage 2, but also to a much lower extent in impactor stage 2 and diffusion stage 1. Interestingly, substantial quantities of Mn and Cu were collected on the impactor stages for the three-mode aerosol but not for the two-mode aerosol. We hypothesize that the metallic ultrafine and fine mode particles coagulated with the coarse-mode particles in the mixing and sampling zones of the chamber. The ultrafine and fine metal particles associated with larger particles were then collected on impactor plates of the PACS. We also considered losses due to diffusion, especially for ultrafine mode

particles. However, the fact that Mn and Cu were present at substantially lower levels on the impactor stages for the two-mode aerosol than those for the three-mode aerosol suggests that diffusion is a minor mechanism of deposition on impactor plates.

The relative magnitudes of elements measured with the nanoMOUDI in the three modes shown in Figure 4-6b are consistent with the time-adjusted masses of elements in PACS stages shown in Figure 4-6a. For example, Cu was mainly collected by the second diffusion stage, so the fine mode dominated the Cu mass concentration. Mn was measured in both impactor and diffusion stages, the Mn concentrations were found among all three modes. However, the element mass concentrations estimated with the MDCS algorithm were not inconsistent with nanoMOUDI or the d_{50s} of PACS stages.

Agreement between the mass size distributions from the PACS and nanoMOUDI was considerably poorer for the two-mode aerosol (Figure 4-6b) than that for the three-mode aerosol (Figure 4-5a). Similar to the three-mode aerosol, the PACS was unable to measure particles smaller than 10 nm. The PACS overestimated the Mn and Cu mass concentration of the ultrafine mode, but severely underestimate the Cu mass concentration of the fine mode (Table 4-2). Adding a backup filter as a last PACS stage might solve the issue of substantially overestimate/underestimate mass concentration for each element. With a backup filter, the PACS would be able to collect all size particles, so that conservation of mass could be used to distribute the mass of each element in each mode.

The accuracy of the fitting results from the MMLN algorithm greatly influenced the accuracy of the results from the MDCS algorithm. We used the *MMD* and *GSD* of each mode obtained from the MMLN fitting results to distribute the mass concentration of the aerosol composition in each mode. For the three-mode aerosol, the algorithm overestimated

the number concentration and the *CMD* of the fine mode (Figure 4-3b); consequently, the PACS overestimated the mass concentration and the *MMD* of the fine mode as well (Figure 4-5b and Table 4-2). For the two-mode aerosol, the MMLN algorithm underestimated the *CMD* of the fine mode (Figure 4-4b), therefore, compared to the nanoMOUDI, the PACS substantially underestimated mass concentration of the fine mode (Figure 4-6b and Table 4-2).

Moreover, the results from the MDCS algorithm were also affected by some assumptions made in the algorithm inputs. For example, we used non-chemical specific data on modes from the MMLN algorithm results to distribute the element mass data (Input 3). The assumption might cause the difference between the measurements from the PACS and nanoMOUDI because particles of different composition usually have various modal structures (Bardouki et al., 2003). In addition, when we calculated the mass percentage of each mode (Eq. 4) and the mass percentage of particles collected by each stage (Eq. 5), we assumed standard density and spherical shape of all particles in the calculation. Furthermore, converting the equivalent mobility diameter measured with the PACS for particles smaller than ~700 nm to the aerodynamic diameter was also based on the assumption of standard density spheres, which is the same as the assumption used to convert the number concentration by size measured with SMPS to surface area and mass concentration by size. However, the particle density and shape factor might be different for various aerosol types (Appendix C). This may be why the size distributions measured with the PACS were consistent with those measured with the SMPS/APS, but not consistent with those measured with nanoMOUDI.

We envision several ways to improve the ability of the PACS to resolve mass size distributions by composition and size in the future. First, the MDCS algorithm is dependent on the accuracy of the fitting results from the MMLN algorithm. The MMLN algorithm could be improved by applying a detector (e.g., diffusion charger) more sensitive to ultrafine mode particles and by adding impactor/diffusion stages. Knowing the modal structure by composition might improve the MDCS algorithm results. We could measure the particle size distribution by composition using the reference instrument (e.g., nanoMOUDI), so that we could apply the measured modal structure by composition to the MDCS algorithm. In addition, after collecting particles, we can analyze the particles physically and chemically to have more reasonable assumptions of the particle density and shape factor. By knowing the particle density and shape factor could improve the MMLN fitting results as well as presented in Chapter III.

Limitations of the study include the potential that the laboratory generated multi-mode aerosols are not representative of real multi-mode aerosols in the occupational and environmental settings. In this study, we only generated fresh Mn fume and aged Cu fume for the ultrafine and fine mode particles, respectively. Many other metal and non-metal aerosol types are needed to be tested. A field study would allow for a practical assessment of the PACS, including set up and durability, and performance of analytical methods in a 'real-world' environment.

Conclusion

In laboratory tests, we demonstrated the feasibility of measuring the size distributions of multi-modal aerosols with the PACS. For a three-mode aerosol, the near-real-time number, surface area and mass concentrations by size measured with the newly-

developed PACS agreed well with those from the SMPS/APS. The mass concentration by element and size estimated with the PACS compared well to those measured with the nanoMOUDI for the coarse mode of all elements, but less so for ultrafine and fine modes. Results were considerably poorer for the two-mode aerosol, especially for near-real-time surface area and mass concentrations by size. Although promising, the PACS in its current form has in sufficient accuracy to replace the reference instruments. Future work will explore ways to improve accuracy through hardware modifications, improvements to the MMLN algorithm, and making reasonable assumptions of particle density, shape factor and modal structure by composition.

Table 4-1: Summary of near-real-time particle concentrations and fit results for the entire size distribution (R^2) measured with the PACS compared to the SMPS/APS.

Metric, units	Concentration		Percentage bias, %	R^2
	PACS	SMPS/APS		
a. Three-mode aerosol				
Number, particles/cm^3	2.6×10^5	2.4×10^5	9.4	0.96
Surface area, μm^2/cm^3	4.7×10^9	4.3×10^9	17.8	0.77
Mass, μg/m^3	1.8×10^3	1.9×10^3	-2.2	0.94
b. Two-mode aerosol				
Number, particles/cm^3	1.8×10^5	2.2×10^5	-17.7	0.51
Surface area, μm^2/cm^3	3.9×10^8	7.2×10^8	-45.5	0.00
Mass, μg/m^3	2.9×10^0	1.6×10^1	-81.8	0.08

Table 4-2: Mass concentrations of Mn, Cu, and Fe by mode and total measured with the PACS compared to the nanoMOUDI.

Device	Mn, μg/m^3				Cu, μg/m^3				Fe, μg/m^3			
	Ultrafine	Fine	Coarse	Total	Ultrafine	Fine	Coarse	Total	Ultrafine	Fine	Coarse	Total
a. Three-mode aerosol												
PACS	0.3	0.4	2.3	3.0	0.3	7.3	0.5	8.0	0.0	5.4	44.7	50.0
Nano_MOUDI	0.9	1.4	1.8	4.2	0.1	6.0	0.4	6.5	0.0	7.9	71.3	79.3
b. Two-mode aerosol												
PACS	1.4	0.2	0.0	1.5	0.3	0.0	0.0	0.3	0.8	0.1	0.0	0.9
Nano_MOUDI	0.4	0.3	0.1	0.8	0.0	8.4	0.1	8.6	0.3	0.1	0.3	0.7

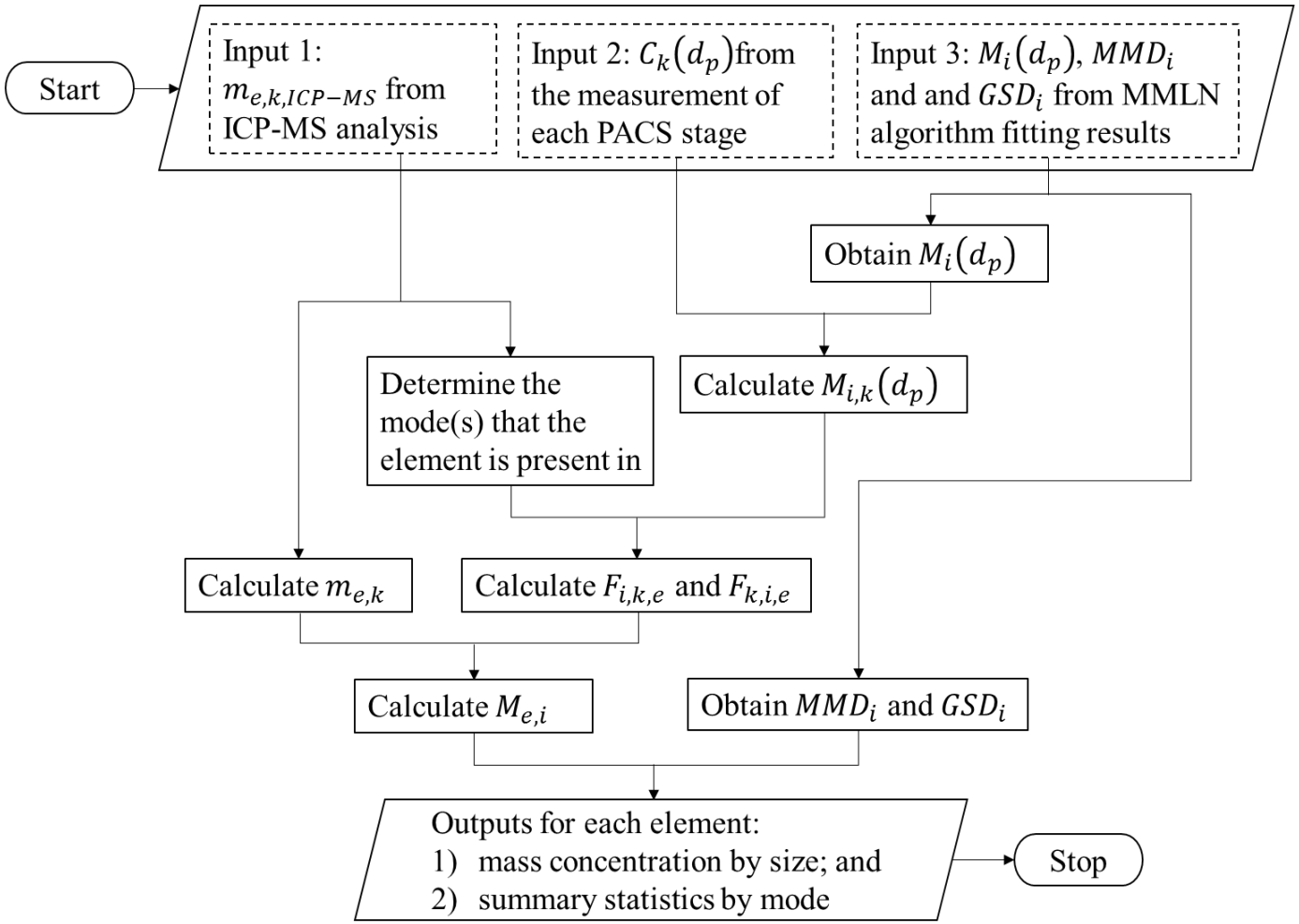

Figure 4-1: Flow chart of the mass distribution by composition and size (MDCS) algorithm to estimate mass size distributions by particle compositions.

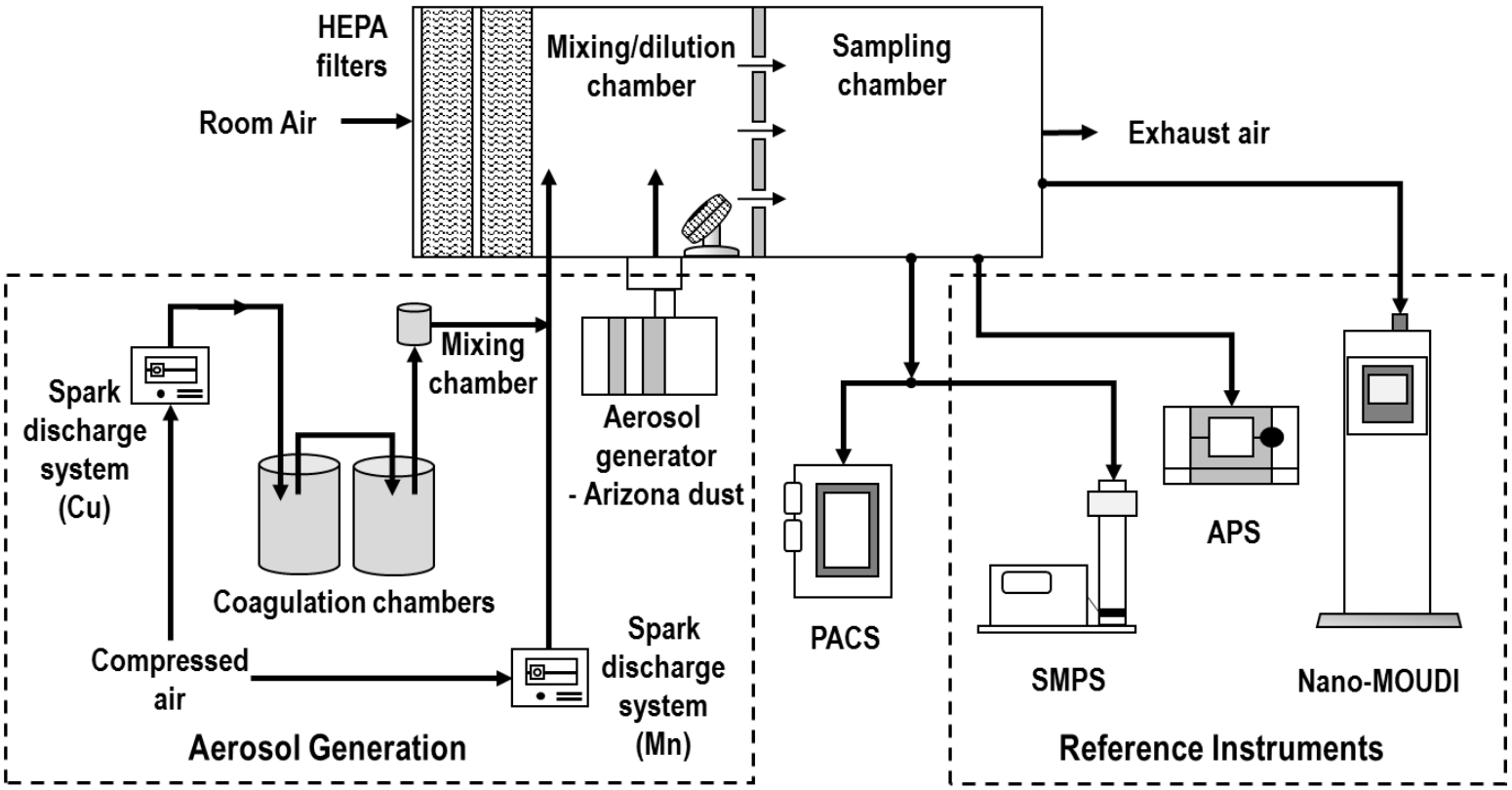

Figure 4-2: Experimental set-up used to compare particle size distributions measured with the PACS to those measured with reference instruments.

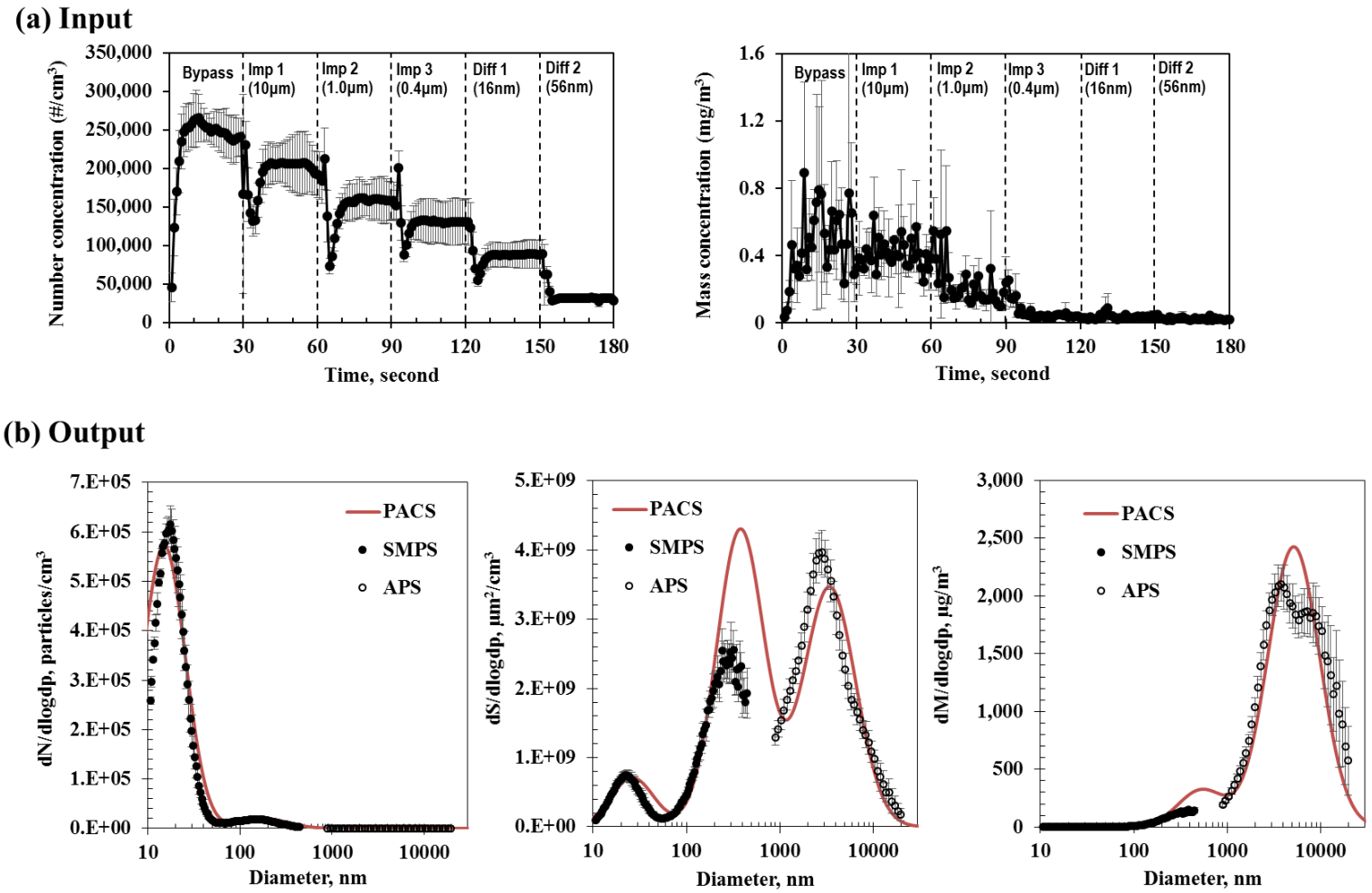

Figure 4-3: Near-real-time number, surface area, and mass concentration by size measured with the PACS compared to the SMPS/APS for the three-mode aerosol: (a) raw input to the multi-modal log-normal (MMLN) algorithm from the WCPC and photometer (stage d_{50} provided in parentheses), and (b) output size distributions from the algorithm. Error bars represent the standard deviation of three measurements during the 1st hour experiment.

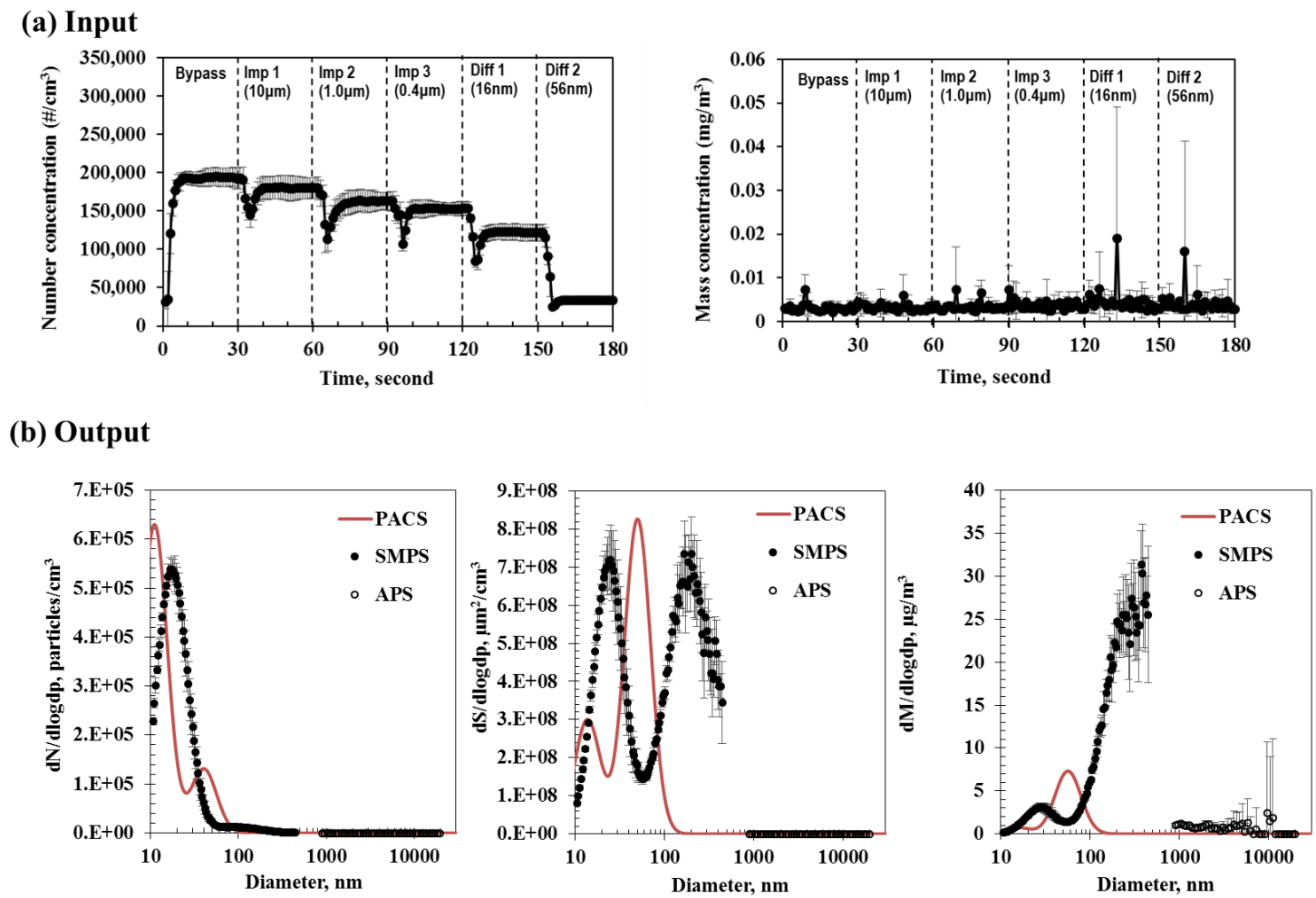

Figure 4-4: Near-real-time number, surface area, and mass concentration by size measured with the PACS compared to the SMPS/APS for the two-mode aerosol: (a) raw input to the multi-modal log-normal (MMLN) algorithm from the WCPC and photometer (stage d_{50} provided in parentheses), and (b) output size distributions from the algorithm. Error bars represent the standard deviation of three measurements during the 1st hour experiment.

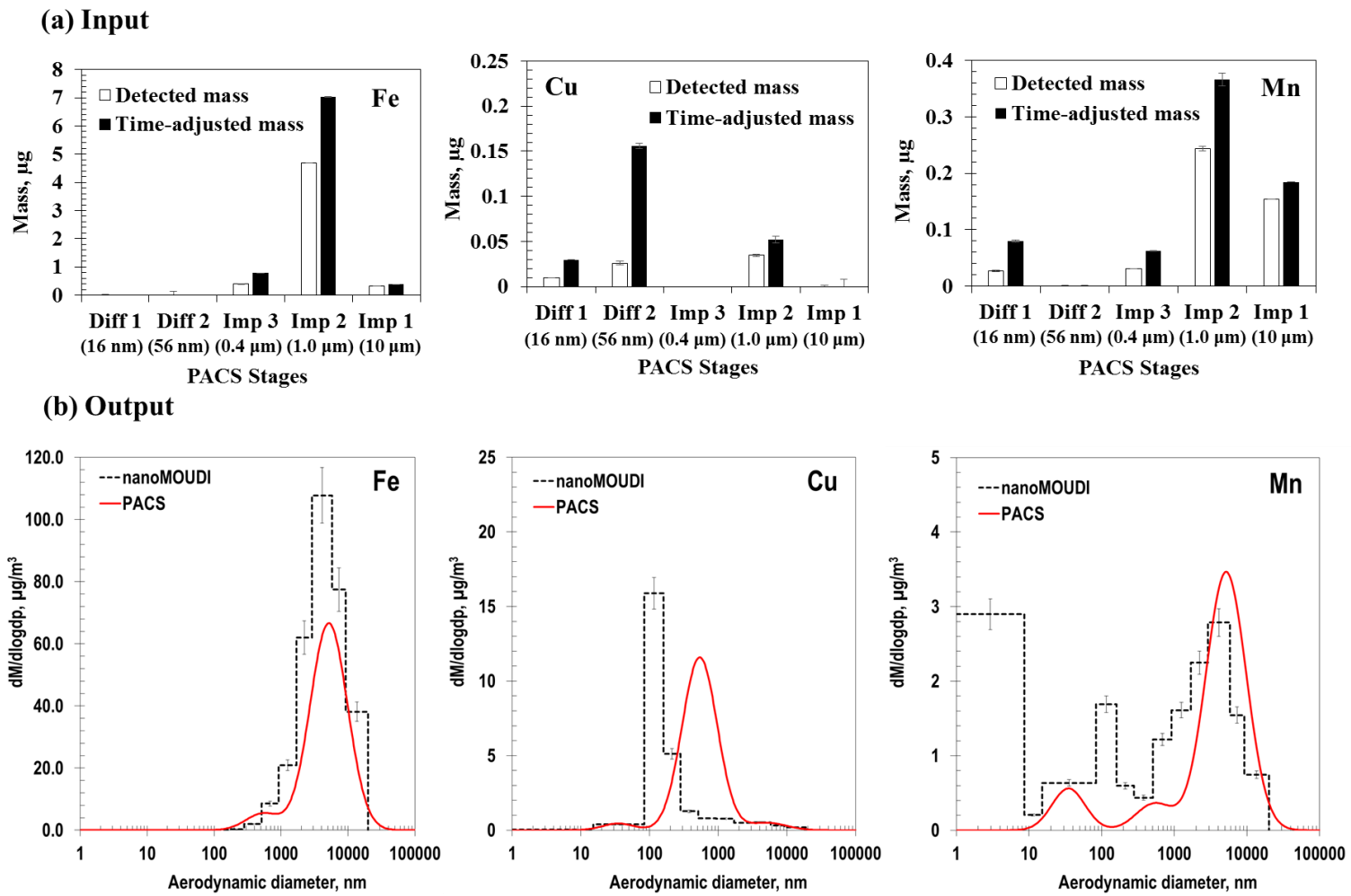

Figure 4-5: Mass concentration by size and composition measured with the PACS compared to the nanoMOUDI for the three-mode aerosol: (a) raw and adjusted input to the mass distribution by composition and size (MDCS) algorithm from ICP-MS (stage d_{50} provided in parentheses), and (b) output size distributions from the algorithm output. Error bars represent the standard deviation of three measurements.

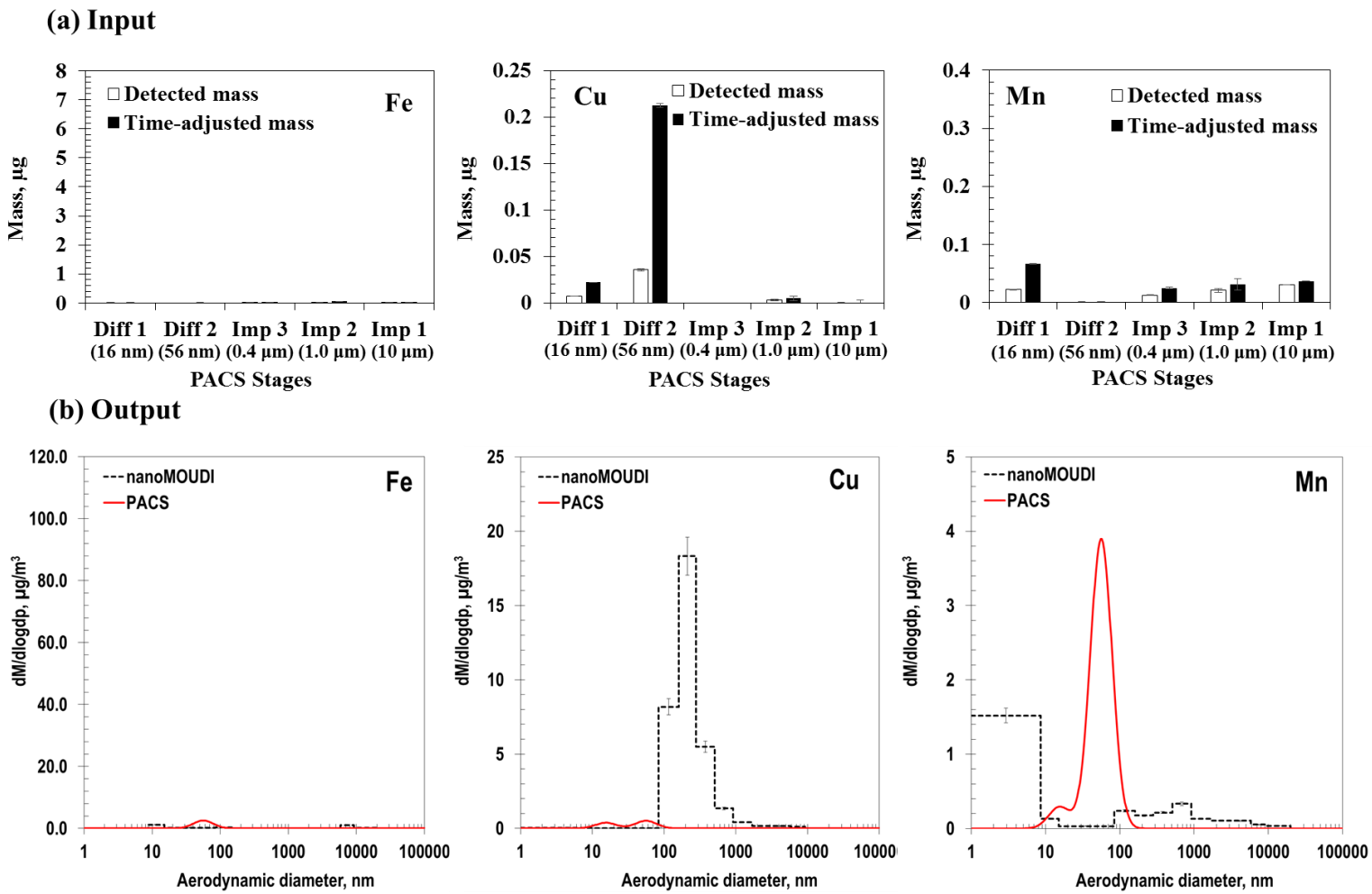

Figure 4-6: Mass concentration by size and composition measured with the PACS compared to the nanoMOUDI for the two-mode aerosol: (a) raw and adjusted input to the mass distribution by composition and size (MDCS) algorithm from ICP-MS (stage d_{50} provided in parentheses), and (b) output size distributions from the algorithm output. Error bars represent the standard deviation of three measurements.

CHAPTER V

CONCLUSIONS

The work presented in this doctoral dissertation accomplishes three goals: 1) it presents the design and testing of the hardware of a Portable Aerosol Collector and Spectrometer (PACS) (Chapter II); 2) it presents the development of a multi-modal log-normal fitting (MMLN) algorithm to estimate aerosol size distributions in three metrics (number, surface area and mass concentration) from 10 nm to 10 μm in near-real-time (Chapter III); 3) it presents the evaluation of a PACS prototype's ability to measure aerosol size distributions in near-real-time for the three metrics, and estimate mass size distributions of various particle compositions in the laboratory (Chapter IV).

Chapter II of this dissertation presented the design and testing of the PACS hardware. The PACS consists of a six-stage particle size selector, a valve system, a water condensation particle counter to detect number concentrations, and a photometer to detect mass concentrations. The valve system diverts airflow sequentially through each stage of the selector to the detectors. The stages of the selector include one bypass stage, three impactor stages, and two diffusion stages, which resolve particles by size (aerodynamic diameter for impactor stages and geometric diameter for diffusion stages) and collect particles for chemical analysis. The first stage allows all size particles entering the inlet to freely pass through to the detectors. Each subsequent stage removes a fraction of particles according to their size. Three impactor stages collect particles by single-hole impactors with designed 50% stage cut-off, $d_{50,s}$, of 10-μm, 1-μm, and 0.3-μm of aerodynamic diameter. The last two stages collect particles by diffusion with designed $d_{50,s}$ of 16 nm and 110 nm of geometric diameter, respectively. A software program samples the particles

at each stage by sequentially opening one valve at a time for 30 sec. A complete, 180-second cycle yields 12 measurements: six number and six mass concentrations.

Particle penetration by size was measured through each stage to determine actual performance and account for particle losses. The testing of the PACS hardware showed that the measured d_{50} (aerodynamic diameter for impactor stages and geometric diameter for diffusion stages) of each stage was similar to the design. The size selector in the PACS removed more particles with each stage added in one sequence of measurement, resulting in stair steps in the raw measurement data. The pressure drop of each stage was sufficiently low to permit its operation with portable air pumps.

Chapter III of this dissertation described the development of the MMLN algorithm to estimate the aerosol size distributions of number, surface area, and mass concentration in near-real-time. The algorithm uses a grid-search process and a constrained linear least-square (CLLS) solver to find a tri-mode (ultrafine, fine, and coarse), log-normal distribution that best fits the input data. We refined the algorithm to obtain accurate and precise size distributions for four aerosols typical of diverse environments: clean background, urban and freeway, coal power plant, and marine surface. Sensitivity studies were conducted to explore the influence of unknown particle density (range from 500 to 3000 kg/m^3) and shape factor (range from 1.0 to 3.0) on algorithm output. An adaptive process that refined the ranges and step sizes of the grid-search reduced the computation time to fit a single size distribution from 43.3 ± 29.0 min to 24.3 ± 11.4 sec.

Assuming standard density spheres, the aerosol size distributions from the MMLN algorithm fit well with a normalized mean bias (*NMB*) of -4.9% to 3.5%, normalized mean error (*NME*) of 3.3% to 27.6%, and R^2 values of 0.90 to 1.00. The bias in fitted total number

and mass concentration were within ± 10% regardless of uncertainties in density and shape factor. However, fitted surface area concentrations were more likely to be underestimated for particle density less than 1000 kg/m^3 and shape factor larger than 1, and overestimated for particle density larger than 1000 kg/m^3. With this algorithm, the PACS is able to estimate aerosol size distributions by number, surface area, and mass concentrations from 10 nm to 10 μm in near real-time.

Chapter IV of this dissertation described a new algorithm–the mass distribution by composition and size (MDCS) algorithm–to estimate the mass size distribution of various particle compositions. Then, it presented an evaluation of the PACS for measuring multi-modal aerosols by comparing to the three reference instruments, including a scanning mobility particle sizer (SMPS), an aerodynamic particle sizer (APS) and a nano micro-orifice uniform deposit impactor (nanoMOUDI) in the laboratory. A two-mode aerosol was generated by spark discharge, consisting of ultrafine (fresh Mn fume) and fine mode particles (aged Cu fume), and a three-mode aerosol was produced by adding coarse mode particles (Arizona road dust) to that generated by spark discharge. We compared the near-real-time aerosol size distributions by number, surface area and mass concentrations measured with the PACS to those measured with an SMPS/APS. We used inductively coupled plasma mass spectrometry (ICP-MS) to measure the mass of collected particles on PACS and nanoMOUDI stages by element (Mn to indicate ultrafine; Cu to indicate fine; and Fe to indicate coarse particles). Mass concentrations by aerodynamic particle size and by element measured with the PACS were compared to those measured with the nanoMOUDI.

For the three-mode aerosol, the aerosol size distributions in the three metrics measured with the PACS agreed well with those measured with the SMPS/APS: number concentration, *bias* = 9.4% and R^2 = 0.96; surface area, *bias* = 17.8%, R^2 = 0.77; mass, *bias* = -2.2%, R^2 = 0.94. Agreement was considerably poorer for the two-mode aerosol, especially for surface area and mass concentrations. Comparing to the nanoMOUDI, for the three-mode aerosol, the PACS estimated the mass median diameters (*MMDs*) of the coarse mode well, but overestimated the *MMDs* for ultrafine and fine modes. The PACS overestimated the mass concentrations of Cu, but underestimated the Mn and Fe. The agreement was considerably poorer for the two-mode aerosol as well. While progress has been made in this work, the PACS in its current form is not able to provide sufficient accuracy in measuring aerosol number, surface area, and mass concentrations by size and composition to replace the reference instruments.

Future Work

We envision several ways to improve the PACS hardware. For example, 180 sec is required for one measurement using the current prototype. If the aerosol concentrations are rapidly changing at the measurement site, the aerosol size distribution measurements might not be accurate. The flowrate is only 0.7 L/min, which might require a long time sampling to collect sufficient particles on the substrates to be detectable. An alternative scheme of reducing the sampling time is to measure the number and mass concentrations in all stages simultaneously by including additional detectors to the outlet of each stage. Moreover, the PACS separator can be made by injection molding of conductive plastic, substantially reducing cost and weight. Furthermore, we envision that these detectors could be combined

in a commercial PACS version, further reducing costs associated with redundant user interfaces and pumps.

We envision several ways to improve the MMLN fitting algorithm results as well. For instance, adding another impactor stage between impactor stage 2 (measured d_{50} of 400 nm) and 3 (measured d_{50} of 1 μm) would provide more information on particle size in the fine mode needed to improve estimates of aerosol size distributions. Moreover, adding another diffusion stage after diffusion stage 2 (measured d_{50} of 56 nm) might also provide more information on particle size in the both ultrafine and fine modes needed to improve estimates of aerosol size distributions. However, adding more stages increases the time to sequence the valves, complicates the airflow path, and increase the time to post-process the data. The design needs to balance the elements.

We also envision several ways to improve the measurement of mass size distribution by composition in the future. First, improving the accuracy of the fitting results from the MMLN algorithm might improve the results of measuring mass size distribution by composition. Second, a more sensitive mass detector (e.g., diffusion charging), which can detect the surface area of particles smaller than 300 nm, might be helpful to improve the fitting results. For example, for both three- and two-mode aerosols, very little mass was detected by the photometer in diffusion stages due to the limitations of the photometer. If we have a more sensitive detector for small particles, we could obtain more information for ultrafine and fine mode particles, which could be used to further leverage the number concentration of the two modes. Finally, using more reasonable assumptions of the modal structures of different particle compositions, and the particle density and shape factor might improve the results of measuring the aerosol composition by size.

My Ph.D. Study Experience

I have a deep fascination with the field of Occupational and Environmental Health. My Ph.D. study at the University of Iowa gave me an open research mind and provided me many teaching opportunities. My research activities included the laboratory experiments and field measurements. Moreover, my Ph.D. dissertation focused on developing both the device hardware/software and related mathematical algorithms. I have been also involved in a research project of applying machine learning methods for air quality forecasting. Therefore, I have two primary research lines of inquiry in the future. Both of them are interdisciplinary in nature. First, I am interested in developing devices for exposure assessment. Second, I am interested in integrating modeling techniques into the Occupational and Environmental Health fields.

My teaching goes in tandem with my research at the University of Iowa. I tutored the Aerosol Technology course at the graduate level for three years (in Fall 2015, 2016 and 2017). In spring 2017, I co-designed and co-taught the Physical Agent Hazards course at the graduate level. After graduating with a doctoral degree in Industrial Hygiene, I would perceive myself as a researcher and educator. This is because: (1) my strongest motivation to study the Occupational and Environmental Health is to improve the working and living environments of humankind; and (2) colleges and universities are the primary places for the new generations of industrial hygienists, engineers and scientists to grow, and I am willing to share the knowledge that I acquired with future generations.

APPENDIX A:

DESIGN AND TEST OF THE THIRD IMPACTOR STAGE

The experience that we obtained from design and test of the third PACS impactor stage might be helpful to other researchers. During the laboratory tests, we measured the particle number concentration by aerodynamic particle size of salt aerosol upstream and downstream of the third impactor that we designed (Figure A-1a). We measured the actual cut-off diameter, d_{50}, to be 184 nm (Figure A-1a), which was substantially smaller than the designed d_{50} of 300 nm.

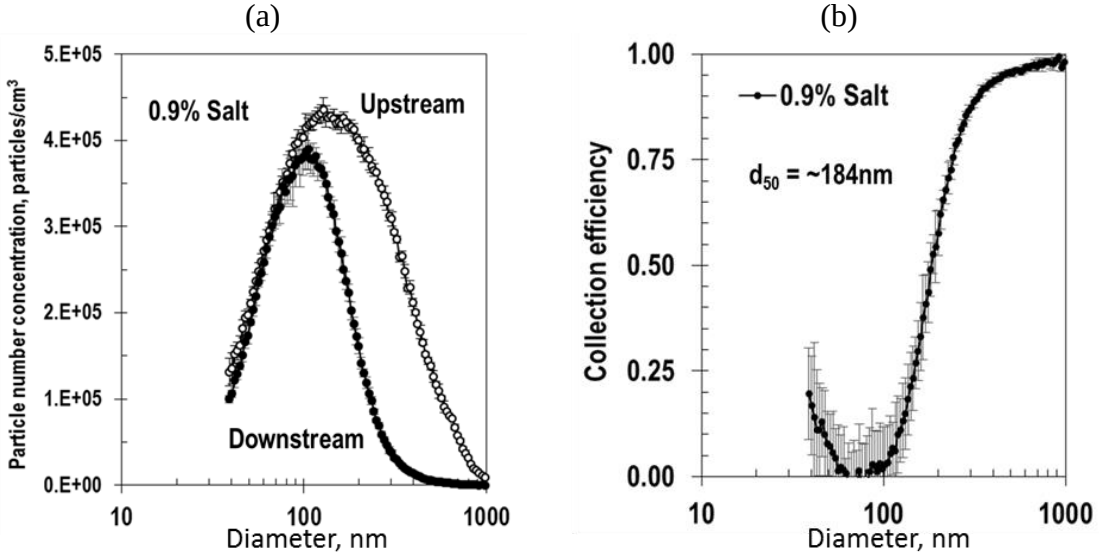

Figure A-1: The measurement of d_{50} of the third impactor stage of the initial design: (a) particle size distributions in both upstream and downstream, and (b) the collection efficiency of the third impactor.

To increase the d_{50}, we increased the diameter of the single, round nozzle of the third impactor stage from 0.360 mm to 0.521 mm, as shown in Figure A-2. In addition to

enlarging the diameter, this process made the impactor nozzle more circular, which we believe is important in obtaining favorable particle separation characteristics. Enlarging the size of the impactor nozzle increased the d50 from ~184 nm to ~400 nm and also decreased the pressure drop from 11.5kPa to 2.2 kPa.

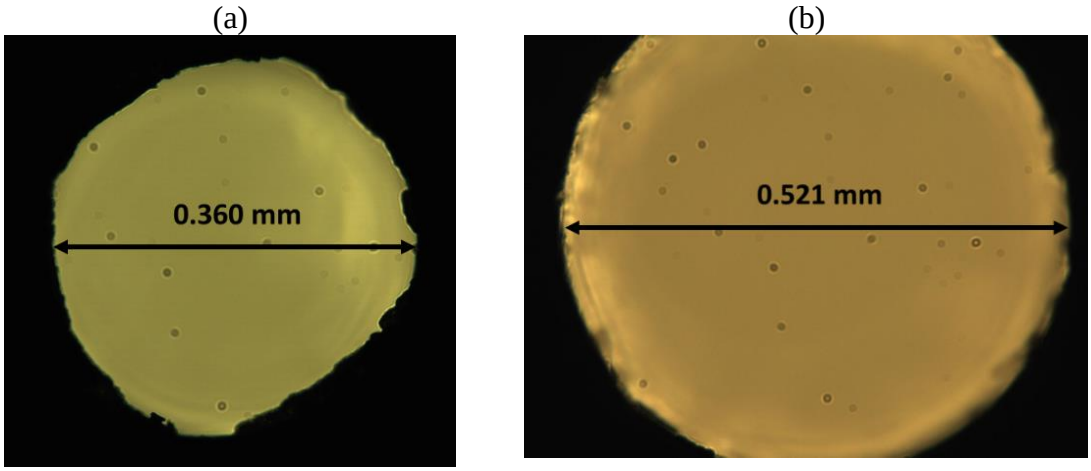

Figure A-2: The third impactor nozzle size: (a) before, and (b) current.

However, we observed substantially higher than expected collection efficiency for nanoparticles due to the diffusion losses of nanoparticles. Collection efficiency sharply increased with decreasing size for particles smaller than 100 nm (up to 45% at 20 nm; see red, circled area in Figure A-3a). This high collection efficiency prevents a substantial fraction of nanoparticles from collecting on the diffusion stage, thereby introducing uncertainty in determination of size distributions. We hypothesized that nanoparticles were able to diffuse given the short distance between the nozzle and the collection plate. To test this hypothesis, we added a washer and O-ring to the screw-in piece that holds the collection plate, thereby increasing the distance between the nozzle and plate by 1.67 mm.

This change dramatically reduced particle collection efficiency of sub-100-nm particles (red, circled area in Figure A-3b), while still maintaining nearly identical collection characteristics for larger particles. With this design change, most nanoparticles collect on the diffusion stages, in line with the intended design of the separator. Thus, we used this as the final design of the third impactor and adopted a similar approach for the other two impactor stages.

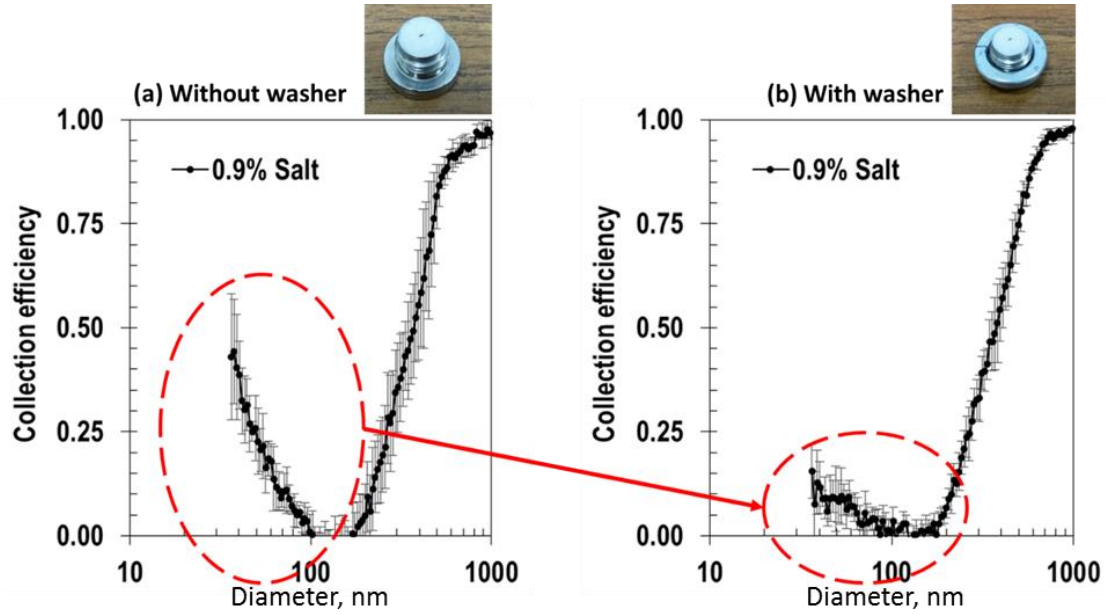

Figure A-3: The measurement of d_{50} of the third impactor stage after drilling: (a) without washer, and (b) with washer.

APPENDIX B:

PRESSURE DROP AND FLOWRATE

During the measurement of pressure drop and flowrate shown in Figure B-1, we found that even with the lower pressure drop of the redesigned third-stage impactor, the internal pumps of the WCPC (piezo-electric pump) and the Sidepak photometer (diaphragm pump) were unable to maintain an airflow of 0.7 Lpm through all stages of the PACS (see column identified as "PACS with internal pumps" in Table B-1). While the airflow was nominally 0.7 Lpm through Stages 1 and 2, it was substantially reduced at Stage 3 (downstream of the 2nd impactor stage; 0.649 Lpm) and more so at Stage 4 (downstream of the third impactor stage; 0.600 Lpm). The relatively low pressure drop of the diffusion stages (Stages 5 and 6) had no further impact on the flowrate. We also experienced failures of the piezo-electric pump within the WCPC due to the extra load on the internal pump.

I replaced the internal pumps of WCPC and Photometer with two external pumps (GilAir Plus, Sensidyne, St. Petersburgh, FL, USA). We set these pumps to operate in low-flow mode with the external pump connected to the WCPC set to 0.3 Lpm and that connected to the photometer set to 0.4 Lpm. For the photometer, the tube from the optics region to the internal pump was disconnected. The external pump was directly connected to the optics region.

The airflow through the device is now constant as we cycle through the different stages of the PACS (see column identified as "PACS with external pumps" in Table B-2).

The airflow was within 0.6% of the target airflow of 0.7 Lpm downstream of all of the stages.

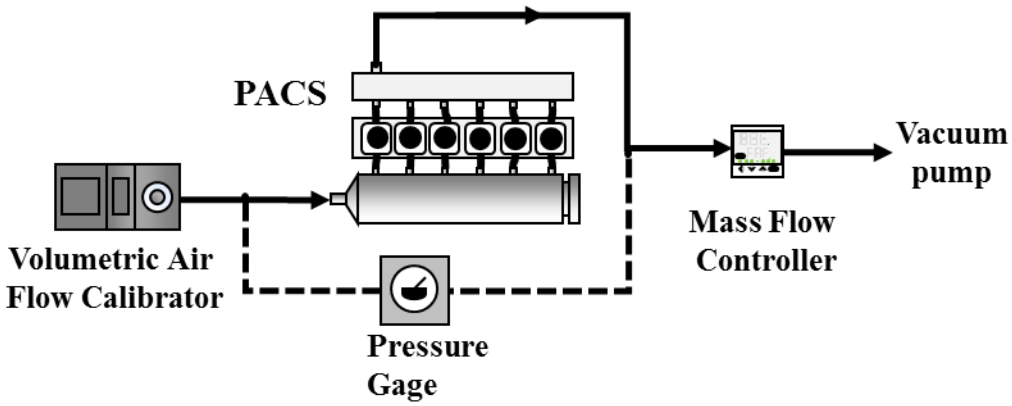

Figure B-1: Experimental setup used to measure flowrate and pressure drop of each PACS stage.

Table B-1: The pressure drop and flowrate measured as air is passed through different stages of the PACS.

Stage No.	Cumulative Pressure drop, kPa	Flowrate, L/min	
		With internal pumps	With external pumps
1	0	0.702	0.698
2	0	0.701	0.698
3	0.65	0.649	0.697
4	2.88	0.600	0.696
5	2.88	0.600	0.697
6	2.88	0.600	0.696

APPENDIX C:

DIAMETER CONVERSION

In this study, the assumed particle densities and shape factors are summarized in Table C-1. The conversion between aerodynamic diameter (d_a) and equivalent mobility diameter (d_e) by considering particle density and shape factor are as follows:

$$d_a = d_e\left(\frac{C_{(de)}\rho_p}{C_{(da)}\rho_0\chi}\right)^{1/2}, \quad \text{(C-1)}$$

where C is the slip correction factor; ρ_p is the density; ρ_0 is the standard particle density (1000 kg/m^3); χ is the shape factor.

Table C-1: Assumed particle density and shape factor used in this study.

Aerosol	Density (kg/m^3)	Shape Factor
Fe fume[1]	5700	1.68[1]
Salt aerosol[2]	2200	1.08
Arizona Road Dust[3]	2650	1.5
Mn fume[4]	5400	1.68[1]
Cu fume[5]	6310	1.68[1]

[1] Cena et al. (2014)
[2] Kelly and McMurry (1992)
[3] Endo et al. (1998)
[4] Kobayashi et al. (1997)
[5] Stefaniak et al. (1997)

```
%% Assumptions
p_dens    = 1000;       % Particle density, kg/m3
s_factor  = 1;          % Shape factor
```

Figure C-1: Snapshot of the particle density and shape factor used in the multi-modal log-normal (MMLN) fitting algorithm in Chapter III.

I converted the diameters for different purposes in the three chapters (Chapter II, III and IV). In the Chapter II of testing the PACS size selector, in order to compare the measured $d_{50,s}$ to the designed ones, I converted the equivalent mobility diameters of Fe fume and salt aerosol measured with SMPS to aerodynamic diameters according to the densities and shape factors summarized in Table C-1. In Chapter III of testing the MMLN fitting algorithm theoretically, I assumed that all aerosols were spherical ($\chi = 1$) with standard density ($\rho_p = 1000\ kg/m^3$) (Figure C-1). Therefore, the equivalent mobility diameter is the same as aerodynamic diameter.

```
% Penetration for each stage
% equivalent mobility diameter for particles < ~700nm (measured with SMPS)
% aerodynamic diameter for particles > ~700nm (measured with APS)
filename_pacs = '02_stage_penetration.xlsx';
sheet = 'penetration';
xlrange = 'A:F';
Pen_stage = xlsread(filename_pacs, sheet, xlrange);
Pen_1  = Pen_stage(:,1);
Pen_6  = Pen_stage(:,2);
Imp_1  = Pen_stage(:,3);
Imp_2  = Pen_stage(:,4);
Imp_3  = Pen_stage(:,5);
Imp_0  = Pen_stage(:,6);
```

Figure C-2: Snapshot of the penetration of each stage used in the multi-modal log-normal (MMLN) fitting algorithm in Chapter IV.

The SMPS and APS measure the equivalent mobility diameter and aerodynamic diameter, respectively. In Chapter IV of testing the PACS prototype, in order to minimize the error caused by diameter conversion, I directly applied the two types of diameter measurement of collection efficiency in each stage as the input of the MMLN algorithm. Therefore, in the MMLN algorithm output, the diameter of particles smaller than ~700 nm

is equivalent mobility diameter, and the diameter of particles larger than ~700 nm is aerodynamic diameter. By comparing the PACS to the nanoMOUDI, since the nanoMOUDI measures the aerodynamic diameter, I converted the PACS measurements into aerodynamic diameter according to the densities and shape factors summarized in Table C-1.

APPENDIX D:

CORE PARTS OF THE FITTING ALGORITHM CODE

The algorithm presented in Chapter III uses a grid-search process, a constrained linear least-square (CLLS) solver and an adaptive process to find a tri-mode (ultrafine, fine, and coarse), log-normal distribution that best fits the PACS input data. In order for researchers to use the three methods in the future, Figure C-1 is the snapshot of the core parts of the code for the three methods.

```
...
parfor gsd_c_par = 21:1:27      % Grid-search GSD for coarse mode (parallel computing)
 for gsd_f = 1.8:0.1:2.2        % Grid-search GSD for fine mode
  for gsd_u = 1.5:0.1:1.8       % Grid-search GSD for ultrafine mode
   for gmd_c = 400:500:2000     % Grid-search CMD for coarse mode
    for gmd_f = 40:50:200       % Grid-search CMD for fine mode
       for gmd_u = 5:5:40       % Grid-search CMD for ultrafine mode
       gsd_c  = gsd_c_par./10;
...
       x=qpas(C'*C, -C'*d, A,b,[],[],...
           xmin,xmax',0);   % A constrained linear least-square (CLLS) solver
       num_c = x(1);        % Calculate number concentration of coarse mode using CLLS
       num_f = x(2);        % Calculate number concentration of fine mode using CLLS
       num_u = x(3);        % Calculate number concentration of ultrafine mode using CLLS
...
% The adaptive process to establish
% new grid-search range of CMD and GSD
if (gmd_u_1 - 5) < 5
    gmd_u_1_b = 5;
    gmd_u_1_a = gmd_u_1 + 5;
elseif (gmd_u_1 + 5) > 40
    gmd_u_1_b = gmd_u_1 - 5;
    gmd_u_1_a = 40;
else
    gmd_u_1_b = gmd_u_1 - 5;
    gmd_u_1_a = gmd_u_1 + 5;
end
    gsd_f_1_b = (gsd_f_1 - 0.1);
    gsd_f_1_a = (gsd_f_1 + 0.1);
...
%% Grid-search GSD and CMD using new ranges
parfor gsd_c_par = gsd_c_1_b:1:gsd_c_1_a
 for gsd_f = gsd_f_1_b:0.1:gsd_f_1_a
  for gsd_u = gsd_u_1_b:0.1:gsd_u_1_a
   for gmd_c = gmd_c_1_b:300:gmd_c_1_a
    for gmd_f = gmd_f_1_b:30:gmd_f_1_a
       for gmd_u = gmd_u_1_b:3:gmd_u_1_a
       gsd_c  = gsd_c_par./10;
...
```

Figure D-1: Snapshot of the code for the three methods (grid-search, CLLS solver and adaptive process) used in the fitting algorithm.

APPENDIX E:

SIZE DISTRIBUTIONS MEASURED WITH THE PACS USING CORRECTED MASS CONCENTRATIONS FROM THE PHOTOMETER

For the two-mode aerosol, we multiplied the mass concentrations measured with the photometer by the correction factor of 5 for the metal fume obtained from the study of Sousan et al. (2017). We then ran the MMLN algorithm to output near-real-time number, surface area, and mass concentration by size (Figure E-1)

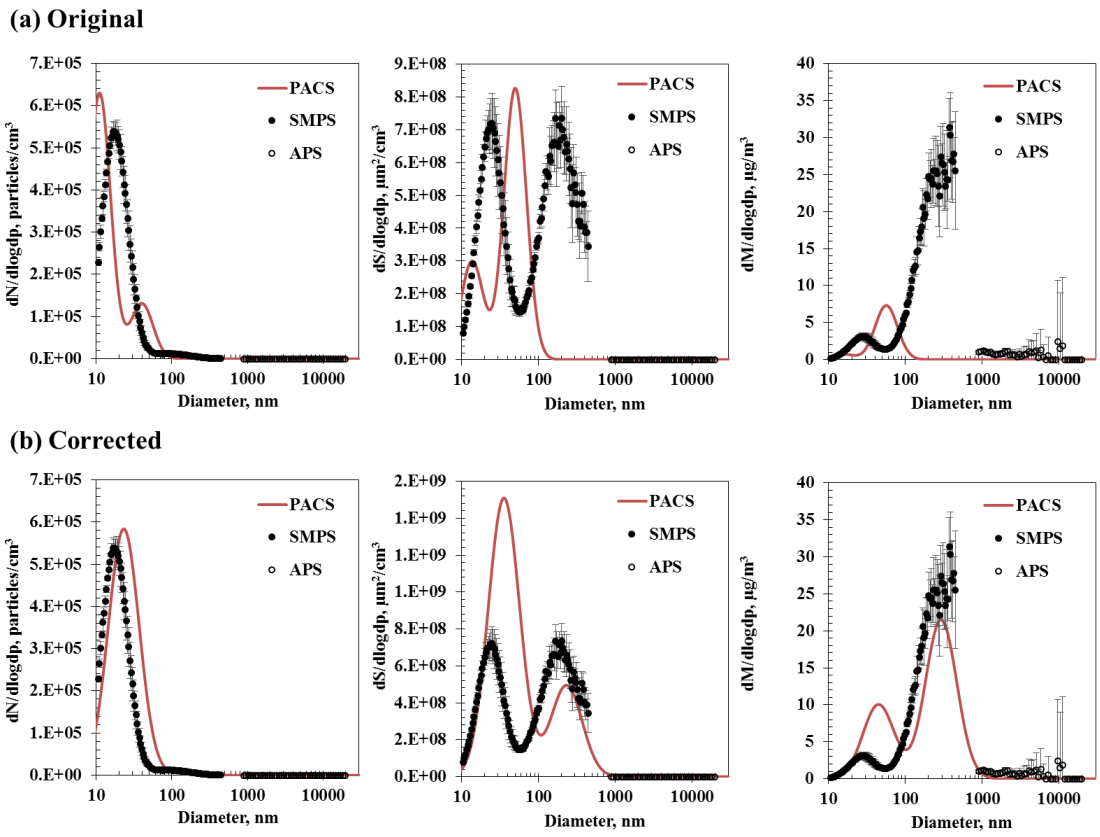

Figure E-1: Near-real-time number, surface area, and mass concentration by size measured with the PACS compared to the SMPS/APS for the two-mode aerosol: (a) original output size distributions from the algorithm. Error bars represent the standard deviation of three measurements during the 1st hour experiment.

REFERENCES

Abt, E., Suh, H. H., Allen, G., & Koutrakis, P. (2000). Characterization of indoor particle sources: A study conducted in the metropolitan Boston area. *Environmental Health Perspectives*, *108*(1), 35.

ACGIH, C. O. (2008). TLVs and BEIs Based on the Documentation of the Threshold Limit Values for Chemical Substances and Physical Agents, and Biological Exposure Indices. In *American Conference of Governmental Industrial Hygienists Cincinnati*.

Ahamed, M., AlSalhi, M. S., & Siddiqui, M. K. J. (2010). Silver nanoparticle applications and human health. *Clinica Chimica Acta*, 411(23), 1841-1848.

Alexander, D. J., Collins, C. J., Coombs, D. W., Gilkison, I. S., Hardy, C. J., Healey, G., ... & McDonald, P. (2008). Association of Inhalation Toxicologists (AIT) working party recommendation for standard delivered dose calculation and expression in non-clinical aerosol inhalation toxicology studies with pharmaceuticals. *Inhalation Toxicology*, 20(13), 1179-1189.

Arora, S., Jain, J., Rajwade, J. M., & Paknikar, K. M. (2008). Cellular responses induced by silver nanoparticles: in vitro studies. *Toxicology Letters*, 179(2), 93-100.

Arora, S., Jain, J., Rajwade, J. M., & Paknikar, K. M. (2009). Interactions of silver nanoparticles with primary mouse fibroblasts and liver cells. *Toxicology and Applied Pharmacology*, 236(3), 310-318.

Baker, J., Peate, D., Waight, T., & Meyzen, C. (2004). Pb isotopic analysis of standards and samples using a 207 Pb–204 Pb double spike and thallium to correct for mass bias with a double-focusing MC-ICP-MS. *Chemical Geology*, 211(3), 275-303.

Bardouki, H., Liakakou, H., Economou, C., Sciare, J., Smolık, J., Ždímal, V., ... & Mihalopoulos, N. (2003). Chemical composition of size-resolved atmospheric aerosols in the eastern Mediterranean during summer and winter. *Atmospheric Environment*, 37(2), 195-208.

Baron, P. A. (1986). Calibration and use of the aerodynamic particle sizer (APS 3300). *Aerosol Science and Technology*, 5(1), 55-67.

Brachert, L., Mertens, J., Khakharia, P., & Schaber, K. (2014). The challenge of measuring sulfuric acid aerosols: number concentration and size evaluation using a condensation particle counter (CPC) and an electrical low pressure impactor (ELPI+). *Journal of Aerosol Science*, 67, 21-27.

Brouwer, D. H., Gijsbers, J. H., & Lurvink, M. W. (2004). Personal exposure to ultrafine particles in the workplace: exploring sampling techniques and strategies. *Annals of Occupational Hygiene*, 48(5), 439-453.

Brunekreef, B., & Forsberg, B. (2005). Epidemiological evidence of effects of coarse airborne particles on health. *European Respiratory Journal*, 26(2), 309-318.

Carslaw, K. S., Boucher, O., Spracklen, D. V., Mann, G. W., Rae, J. G. L., Woodward, S., & Kulmala, M. (2010). A review of natural aerosol interactions and feedbacks within the Earth system. *Atmospheric Chemistry and Physics*, 10(4), 1701-1737.

Cena, L. G., Anthony, T. R., & Peters, T. M. (2011). A personal nanoparticle respiratory deposition (NRD) sampler. *Environmental Science and Technology*, 45(15), 6483-6490.

Cena, L. G., Chisholm, W. P., Keane, M. J., Cumpston, A., & Chen, B. T. (2014). Size distribution and estimated respiratory deposition of total chromium, hexavalent chromium, manganese, and nickel in gas metal arc welding fume aerosols. *Aerosol Science and Technology*, 48(12), 1254-1263.

Chen, M., Romay, F. J., Li, L., Naqwi, A., & Marple, V. A. (2016). A novel quartz crystal cascade impactor for real-time aerosol mass distribution measurement. *Aerosol Science and Technology*, 50(9), 971-983.

Cheng, Y. S., and Yeh, H. C. (1980). Theory of a Screen-type Diffusion Battery. *Journal of Aerosol Science*, 11: 313-320.

Chow, J. C., Watson, J. G., Ono, D. M., & Mathai, C. V. (1993). PM10 standards and nontraditional particulate source controls: a summary of the A&WMA/EPA international specialty conference. *Air & Waste*, 43(1), 74-84.

Craighead, J. E., Abraham, J. L., Churg, A. A., Green, F. H., Kleinerman, J., Pratt, P., ... & Weill, H. (1982). The pathology of asbestos-associated diseases of the lungs and pleural cavities: diagnostic criteria and proposed grading schema. Report of the Pneumoconiosis Committee of the College of American Pathologists and the National Institute for Occupational Safety and Health. *Archives of Pathology & Laboratory Medicine*, 106(11), 544.

Crump, J. G., & Seinfeld, J. H. (1981). A new algorithm for inversion of aerosol size distribution data. *Aerosol Science and Technology*, 1(1), 15-34.

Demange, M., Görner, P., Elcabache, J. M., & Wrobel, R. (2002). Field comparison of 37-mm closed-face cassettes and IOM samplers. *Applied Occupational and Environmental Hygiene*, 17(3), 200-208.

Elder, A., Gelein, R., Silva, V., Feikert, T., Opanashuk, L., Carter, J., ... & Oberdörster, G. (2006). Translocation of inhaled ultrafine manganese oxide particles to the central nervous system. *Environmental Health Perspectives*, 114(8), 1172.

Ellenbecker, M. J., & Tsai, C. S. J. (2015). *Exposure assessment and safety considerations for working with engineered nanoparticles*. John Wiley & Sons.

Endo, Y., Chen, D. R., & Pui, D. Y. (1998). Effects of particle polydispersity and shape factor during dust cake loading on air filters. *Powder Technology*, 98(3), 241-249.

EPA. (2006). 40 CFR Parts 58- *Ambient Air Quality Surveillance (Subchapter C)*. Environmental Protection Agency, Washington, DC.

Görner, P., Bemer, D., & Fabries, J. F. (1995). Photometer measurement of polydisperse aerosols. *Journal of Aerosol Science*, 26(8), 1281-1302.

Gouesbet, G., & Grehan, G. (2013). *Optical particle sizing: theory and practice*. Springer Science & Business Media.

Hakala, J., Manninen, H. E., Petäjä, T., & Sipilä, M. (2013). Counting efficiency of a TSI environmental particle counter monitor model 3783. *Aerosol Science and Technology*, 47(5), 482-487.

Harrison, R. M., Shi, J. P., Xi, S., Khan, A., Mark, D., Kinnersley, R., & Yin, J. (2000). Measurement of number, mass and size distribution of particles in the atmosphere. *Philosophical Transactions of the Royal Society of London A: Mathematical, Physical and Engineering Sciences*, 358(1775), 2567-2580.

Harrison, R. M., & Yin, J. (2000). Particulate matter in the atmosphere: which particle properties are important for its effects on health?. *Science of the Total Environment*, 249(1), 85-101.

Hata, M., Linfa, B., Otani, Y., & Furuuchi, M. (2012). Performance evaluation of an andersen cascade impactor with an additional stage for nanoparticle sampling. *Aerosol and Air Quality Research*, 12(6), 1041-1048.

Heitbrink, W. A., Evans, D. E., Ku, B. K., Maynard, A. D., Slavin, T. J., & Peters, T. M. (2008). Relationships among particle number, surface area, and respirable mass concentrations in automotive engine manufacturing. *Journal of Occupational and Environmental Hygiene*, 6(1), 19-31.

Hering, S. V., Stolzenburg, M. R., Quant, F. R., Oberreit, D. R., & Keady, P. B. (2005). A laminar-flow, water-based condensation particle counter (WCPC). *Aerosol Science and Technology*, 39(7), 659-672.

Hering, S. V., Spielman, S. R., & Lewis, G. S. (2014). Moderated, water-based, condensational particle growth in a laminar flow. *Aerosol Science and Technology*, 48(4), 401-408.

Herner, J. D., Green, P. G., & Kleeman, M. J. (2006). Measuring the trace elemental composition of size-resolved airborne particles. *Environmental Science and Technology*, 40(6), 1925-1933.

Hinds, W. C. (1999). Aerosol technology: properties, behavior, and measurement of airborne particles. John Wiley & Sons

Hussein, T., Dal Maso, M., Petaja, T., Koponen, I. K., Paatero, P., Aalto, P. P., ... & Kulmala, M. (2005). Evaluation of an automatic algorithm for fitting the particle number size distributions. *Boreal Environment Research*, 10(5), 337.

Jaenicke, R. (1972). The optical particle counter: cross-sensitivity and coincidence. *Journal of Aerosol Science*, 3(2), 95-111.

Järvinen, A., Heikkilä, P., Keskinen, J., & Yli-Ojanperä, J. (2017). Particle charge-size distribution measurement using a differential mobility analyzer and an electrical low pressure impactor. *Aerosol Science and Technology*, 51(1), 20-29.

Jiang, R. T., Acevedo-Bolton, V., Cheng, K. C., Klepeis, N. E., Ott, W. R., & Hildemann, L. M. (2011). Determination of response of real-time SidePak AM510 monitor to secondhand smoke, other common indoor aerosols, and outdoor aerosol. *Journal of Environmental Monitoring*, 13(6), 1695-1702.

Jianzhong, L., Xing, S., & Zhenjiang, Y. (2003). Effects of the aspect ratio on the sedimentation of a fiber in Newtonian fluids. *Journal of Aerosol Science*, 34(7), 909-921.

KANOMAX, *Nanosampler Model 3180*. (2012). http://www.kanomax.co.jp/products/1103.html

Karlsson, H. L., Cronholm, P., Gustafsson, J., & Moller, L. (2008). Copper oxide nanoparticles are highly toxic: a comparison between metal oxide nanoparticles and carbon nanotubes. *Chemical Research in Toxicology*, 21(9), 1726-1732.

Karthikeyan, S., Joshi, U. M., & Balasubramanian, R. (2006). Microwave assisted sample preparation for determining water-soluble fraction of trace elements in urban airborne particulate matter: evaluation of bioavailability. *Analytica Chimica Acta*, 576(1), 23-30.

Keck, L., Pesch, M., & Grimm, H. (2011). Comprehensive Measurement of Atmospheric Aerosols with a Wide Range Aerosol Spectrometer. *In Journal of Physics: Conference Series* (Vol. 304, No. 1, p. 012065). IOP Publishing.

Kelly, W. P., & McMurry, P. H. (1992). Measurement of particle density by inertial classification of differential mobility analyzer–generated monodisperse aerosols. *Aerosol Science and Technology*, 17(3), 199-212.

Keskinen, J., Pietarinen, K., & Lehtimäki, M. (1992). Electrical low pressure impactor. *Journal of Aerosol Science*, 23(4), 353-360.

Kim, S. C., Wang, J., Emery, M. S., Shin, W. G., Mulholland, G. W., & Pui, D. Y. (2009). Structural property effect of nanoparticle agglomerates on particle penetration through fibrous filter. *Aerosol Science and Technology*, 43(4), 344-355.

Kittelson, D. B. (1998). Engines and nanoparticles: a review. *Journal of Aerosol Science*, 29(5), 575-588.

Klepeis, N. E., Ott, W. R., & Switzer, P. (2007). Real–time measurement of outdoor tobacco smoke particles. *Journal of the Air & Waste Management Association*, 57(5), 522-534.

Kobayashi, M., Maki, S., Hashimoto, Y., & Suga, T. (1983). Investigations on chemical composition of welding fumes. *Welding Journal*, 62(7), 190.

Koehler, K. A., Clark, P., & Volckens, J. (2009). Development of a sampler for total aerosol deposition in the human respiratory tract. *Annals of Occupational Hygiene*, 53(7), 731-738.

Kulkarni, P., Chellam, S., Flanagan, J. B., & Jayanty, R. K. M. (2007). Microwave digestion—ICP-MS for elemental analysis in ambient airborne fine particulate matter: Rare earth elements and validation using a filter borne fine particle certified reference material. *Analytica Chimica Acta*, 599(2), 170-176.

Kulkarni, P., Baron, P. A., & Willeke, K. (Eds.). (2011). *Aerosol measurement: principles, techniques, and applications.* John Wiley & Sons.

Kuo, Y. M., Huang, S. H., Shih, T. S., Chen, C. C., Weng, Y. M., & Lin, W. Y. (2005). Development of a size-selective inlet-simulating ICRP lung deposition fraction. *Aerosol Science and Technology*, 39(5), 437-443.

Kwakye, G. F., Paoliello, M., Mukhopadhyay, S., Bowman, A. B., & Aschner, M. (2015). Manganese-induced Parkinsonism and Parkinson's disease: shared and distinguishable features. *International Journal of Environmental Research and Public Health*, 12(7), 7519-7540.

Liu, S., Hu, M., Wu, Z., Wehner, B., Wiedensohler, A., & Cheng, Y. (2008). Aerosol number size distribution and new particle formation at a rural/coastal site in Pearl River Delta (PRD) of China. *Atmospheric Environment*, 42(25), 6275-6283.

Liu, B. Y., Romay, F. J., Dick, W. D., Woo, K. S., & Chiruta, M. (2010). A wide-range particle spectrometer for aerosol measurement from 0.010 μm to 10 μm. *Aerosol and Air Quality Research*, 10, 125-139.

Maenhaut, W., Hillamo, R., Mäkelä, T., Jaffrezo, J. L., Bergin, M. H., & Davidson, C. I. (1996). A new cascade impactor for aerosol sampling with subsequent PIXE analysis. *Nuclear Instruments and Methods in Physics Research Section B: Beam Interactions with Materials and Atoms*, 109, 482-487.

Maher, E. F., & Laird, N. M. (1985). EM algorithm reconstruction of particle size distributions from diffusion battery data. *Journal of Aerosol Science*, 16(6), 557-570.

Marjamäki, M., Keskinen, J., Chen, D. R., & Pui, D. Y. (2000). Performance evaluation of the electrical low-pressure impactor (ELPI). *Journal of Aerosol Science*, 31(2), 249-261.

Markowski, G. R. (1987). Improving Twomey's algorithm for inversion of aerosol measurement data. *Aerosol Science and Technology*, 7(2), 127-141.

Marple, V. A., and Willeke, K. (1976). Impactor Design. *Atmospheric Environment (1967)*, 10(10): 891-896.

Marple, V. A. K. G. H. J., Rubow, K., Ananth, G., & Fissan, H. J. (1986). Micro-orifice uniform deposit impactor. *Journal of Aerosol Science*, 17(3), 489-494.

Marple, V. A., Rubow, K. L., & Behm, S. M. (1991). A microorifice uniform deposit impactor (MOUDI): description, calibration, and use. *Aerosol Science and Technology*, 14(4), 434-446.

Marple, V. A., Rubow, K. L., & Olson, B. A. (2001). Inertial, gravitational, centrifugal, and thermal collection techniques. *Aerosol Measurement: Principles, Techniques, and Applications*, 2, 229-260.

MATLAB. (2014). MATLAB R2014a, Natick, MA: The MathWorks Inc.

Maynard, A. D., Baron, P. A., Foley, M., Shvedova, A. A., Kisin, E. R., & Castranova, V. (2004). Exposure to carbon nanotube material: aerosol release during the handling of unrefined single-walled carbon nanotube material. *Journal of Toxicology and Environmental Health, Part A*, 67(1), 87-107.

Maynard, A. D., Aitken, R. J., Butz, T., Colvin, V., Donaldson, K., Oberdörster, G., ... & Tinkle, S. S. (2006). Safe handling of nanotechnology. *Nature*, 444(7117), 267-269.

Mossman, B. T., & Churg, A. (1998). Mechanisms in the pathogenesis of asbestosis and silicosis. *American Journal of Respiratory and Critical Care Medicine*, 157(5), 1666-1680.

Natusch, D. F., & Wallace, J. R. (1974). Urban aerosol toxicity: the influence of particle size. *Science*, 186(4165), 695-699.

NIOSH. (2012). *Components for Evaluation of Direct-Reading Monitors for Gases and Vapors.* DHHS (NIOSH) Publication No. 2012–162. National Institute for Occupational Safety and Health, Cincinnati, OH.

Nukiyama, S. (1939). Experiments on the atomization of liquids in an air stream, report 3, on the droplet-size distribution in an atomized jet. *Trans. Soc. Mech. Eng. Jpn.*, 5(18), 62-67.

Olanow, C. W. (2004). Manganese-induced parkinsonism and Parkinson's disease. *Annals of the New York Academy of Sciences*, 1012(1), 209-223.

Onat, B., Şahin, Ü. A., & Bayat, C. (2012). Assessment of particulate matter in the urban atmosphere: size distribution, metal composition and source characterization using principal component analysis. *Journal of Environmental Monitoring*, 14(5), 1400-1409.

Ostro, B., Sanchez, J. M., Aranda, C., & Eskeland, G. S. (1996). Air pollution and mortality: results from a study of Santiago, Chile. *Journal of Exposure Analysis and Environmental Epidemiology*, 6(1), 97-114.

Pak, S. S., Liu, B. Y., & Rubow, K. L. (1992). Effect of coating thickness on particle bounce in inertial impactors. *Aerosol Science and Technology*, 16(3), 141-150.

Palomäki, J., Välimäki, E., Sund, J., Vippola, M., Clausen, P. A., Jensen, K. A., ... & Alenius, H. (2011). Long, needle-like carbon nanotubes and asbestos activate the NLRP3 inflammasome through a similar mechanism. *ACS Nano*, 5(9), 6861-6870.

Park, J. H., Mudunkotuwa, I. A., Kim, J. S., Stanam, A., Thorne, P. S., Grassian, V. H., & Peters, T. M. (2014). Physicochemical characterization of simulated welding fumes from a spark discharge system. *Aerosol Science and Technology*, 48(7), 768-776.

Park, K., Kittelson, D. B., & McMurry, P. H. (2004). Structural properties of diesel exhaust particles measured by transmission electron microscopy (TEM): Relationships to particle mass and mobility. *Aerosol Science and Technology*, 38(9), 881-889.

Peters, T. M., Ott, D., & O'shaughnessy, P. T. (2006). Comparison of the Grimm 1.108 and 1.109 portable aerosol spectrometer to the TSI 3321 aerodynamic particle sizer for dry particles. *The Annals of Occupational Hygiene*, 50(8), 843-850.

Peters, T. M., Elzey, S., Johnson, R., Park, H., Grassian, V. H., Maher, T., & O'Shaughnessy, P. (2008). Airborne monitoring to distinguish engineered nanomaterials from incidental particles for environmental health and safety. *Journal of Occupational and Environmental Hygiene*, 6(2), 73-81.

Poland, C. A., Duffin, R., Kinloch, I., Maynard, A., Wallace, W. A., Seaton, A., ... & Donaldson, K. (2008). Carbon nanotubes introduced into the abdominal cavity of mice show asbestos-like pathogenicity in a pilot study. *Nature Nanotechnology*, 3(7), 423-428.

Pope III, C. A., Burnett, R. T., Thun, M. J., Calle, E. E., Krewski, D., Ito, K., & Thurston, G. D. (2002). Lung cancer, cardiopulmonary mortality, and long-term exposure to fine particulate air pollution. *Jama*, 287(9), 1132-1141.

Pöschl, U. (2005). Atmospheric aerosols: composition, transformation, climate and health effects. *Angewandte Chemie International Edition*, 44(46), 7520-7540.

Pruppacher, H. R., & Klett, J. D. (2012). *Microphysics of Clouds and Precipitation*. Reprinted 1980. Springer Science & Business Media.

Ramachandran, G., Paulsen, D., Watts, W., & Kittelson, D. (2005). Mass, surface area and number metrics in diesel occupational exposure assessment. *Journal of Environmental Monitoring*, 7(7), 728-735.

Ramadan, Z., Song, X. H., & Hopke, P. K. (2000). Identification of sources of Phoenix aerosol by positive matrix factorization. *Journal of the Air & Waste Management Association*, 50(8), 1308-1320.

Reineking, A., & Porstendörfer, J. (1986). Measurements of particle loss functions in a differential mobility analyzer (TSI, Model 3071) for different flow rates. *Aerosol Science and Technology*, 5(4), 483-486.

RosIN, P. A. U. L. (1933). The laws governing the fineness of powdered coal. *Journal of the Institute of Fuel*, 7, 29-36.

Rubenstein, D. I., & Koehl, M. A. R. (1977). The mechanisms of filter feeding: some theoretical considerations. *The American Naturalist*, 111(981), 981-994.

Seinfeld, J. H., & Pandis, S. N. (2016). *Atmospheric chemistry and physics: from air pollution to climate change*. John Wiley & Sons.

Shi, J. P., Khan, A. A., & Harrison, R. M. (1999). Measurements of ultrafine particle concentration and size distribution in the urban atmosphere. *Science of the Total Environment*, 235(1), 51-64.

Sousan, S., Koehler, K., Hallett, L., & Peters, T. M. (2016). Evaluation of the Alphasense optical particle counter (OPC-N2) and the Grimm portable aerosol spectrometer (PAS-1.108). *Aerosol Science and Technology*, 50(12), 1352-1365.

Sousan, S., Koehler, K., Hallett, L., & Peters, T. M. (2017). Evaluation of consumer monitors to measure particulate matter. *Journal of Aerosol Science*, 107, 123-133.

Stefaniak, A. B., Hoover, M. D., Dickerson, R. M., Peterson, E. J., Day, G. A., Breysse, P. N., ... & Scripsick, R. C. (2003). Surface area of respirable beryllium metal, oxide, and copper alloy aerosols and implications for assessment of exposure risk of chronic beryllium disease. *Aiha Journal*, 64(3), 297-305.

Takagi, A., Hirose, A., Nishimura, T., Fukumori, N., Ogata, A., Ohashi, N., ... & Kanno, J. (2008). Induction of mesothelioma in p53+/− mouse by intraperitoneal application of multi-wall carbon nanotube. *The Journal of Toxicological Sciences*, 33(1), 105-116.

Taylor, M., Kazadzis, S., & Gerasopoulos, E. (2014). Multi-modal analysis of aerosol robotic network size distributions for remote sensing applications: dominant aerosol type cases. *Atmospheric Measurement Techniques*, 7(3), 839.

Tsai, C. J., Liu, C. N., Hung, S. M., Chen, S. C., Uang, S. N., Cheng, Y. S., & Zhou, Y. (2012). Novel active personal nanoparticle sampler for the exposure assessment of nanoparticles in workplaces. *Environmental Science and Technology*, 46(8).

Turpin, B. J., & Lim, H. J. (2001). Species contributions to PM2. 5 mass concentrations: Revisiting common assumptions for estimating organic mass. *Aerosol Science and Technology*, 35(1), 602-610.

Twomey, S. (1965). The application of numerical filtering to the solution of integral equations encountered in indirect sensing measurements. *Journal of the Franklin Institute*, 279(2), 95-109.

Twomey, S. (1975). Comparison of constrained linear inversion and an iterative nonlinear algorithm applied to the indirect estimation of particle size distributions. *Journal of Computational Physics*, 18(2), 188-200.

Valavanidis, A., Fiotakis, K., & Vlachogianni, T. (2008). Airborne particulate matter and human health: toxicological assessment and importance of size and composition of particles for oxidative damage and carcinogenic mechanisms. *Journal of Environmental Science and Health, Part C*, 26(4), 339-362.

Vosburgh, D. J., Klein, T., Sheehan, M., Anthony, T. R., & Peters, T. M. (2013). Design and evaluation of a personal diffusion battery. *Aerosol Science and Technology*, 47(4), 435-443.

Wallace, L., & Howard-Reed, C. (2002). Continuous monitoring of ultrafine, fine, and coarse particles in a residence for 18 months in 1999-2000. *Journal of the Air & Waste Management Association*, 52(7), 828-844.

Wang, S. C., & Flagan, R. C. (1990). Scanning electrical mobility spectrometer. *Aerosol Science and Technology*, 13(2), 230-240.

Whitby, K. T. (1978). The physical characteristics of sulfur aerosols. *Atmospheric Environment (1967)*, 12(1-3), 135-159.

Whitby, K. T., & Sverdrup, G. M. (1980). California aerosols-their physical and chemical characteristics. *Adv. Environ. Sci. Technol.;(United States)*, 9.

Wilson, W. E., & Suh, H. H. (1997). Fine particles and coarse particles: concentration relationships relevant to epidemiologic studies. *Journal of the Air & Waste Management Association*, 47(12), 1238-1249.

Wittmaack, K. (2007). In search of the most relevant parameter for quantifying lung inflammatory response to nanoparticle exposure: particle number, surface area, or what?. *Environmental Health Perspectives*, 115(2), 187.

Wolfenbarger, J. K., & Seinfeld, J. H. (1990). Inversion of aerosol size distribution data. *Journal of Aerosol Science*, 21(2), 227-247.